論文 / 著書情報
Article / Book Information

題目(和文)	大規模積層型静電アクチュエータの開発
Title(English)	Development of a Large-scale Stacked-type Electrostatic Actuator
著者(和文)	伊藤誠
Author(English)	Makoto Ito
出典(和文)	学位:博士(理学), 学位授与機関:東京工業大学, 報告番号:甲第9376号, 授与年月日:2014年3月26日, 学位の種別:課程博士, 審査員:實吉　敬二,中村　隆司,垣本　史雄,柴田　利明,宗宮　健太郎
Citation(English)	Degree:Doctor (Science), Conferring organization: Tokyo Institute of Technology, Report number:甲第9376号, Conferred date:2014/3/26, Degree Type:Course doctor, Examiner:,,,,
学位種別(和文)	博士論文
Type(English)	Doctoral Thesis

Development of a Large-scale Stacked-type Electrostatic Actuator

a dissertation presented
by
Makoto Ito
to
The Physics

in partial fulfillment of the requirements
for the degree of
Doctor of Philosophy
in the subject of
Science

Tokyo Institute of Technology
Yokohama, Kanagawa
Feb. 2014

Development of a Large-scale Stacked-type Electrostatic Actuator

Abstract

Electrostatic actuators have the advantages of light weight, flexibility, and high energy efficiency, which make them suitable for use as artificial muscles. However, a traditional electrostatic actuator cannot generate long strokes and a high force density at the same time because such actuator would excessively widen the gap between the electrodes because of its structure.

This paper presents a newly developed large-scale stacked-type electrostatic actuator (LSEA) intended for use as an artificial muscle for robots. An LSEA is a multi-stacked electrostatic actuator that can be linearly contracted by the application of a voltage. It has a unique structure that prevents overextension of the gap between the electrodes. It can therefore generate a large force.

In this study, two different prototypes were made to experimentally determine the spring characteristics, the relationship between the contractive force and the stroke, and power consumption. The findings showed that LSEA prevents the overextension of the gap between the electrodes and has a high contraction ratio that is equivalent to that of a mammalian skeletal muscle. The force density (or the actuation energy density) was hundredth smaller than that of muscles, but it can be improved by applying short and thin hinge parts. The experiment in vacuum shows the effect of air drag. The effect was not change the performance of the prototype although it might be not negligible when the air gaps between the electrodes are short considerably.

As an additional study, fundamental concept of a physics engine was proposed as a method to simulate the performance of LSEAs. In this simulation, the hinge

parts were considered as compounds of linear springs and torsion springs in order to simplify the hinge model and reduce the calculation cost. This concept enables us to calculate more complex LSEA models in less time in comparison with FEM model. The result example of calculation of spring characteristics showed the adequacy of the spring hinge model in the case of a 6-layered 3×1 LSEA model.

Contents

1 Introduction **1**
- 1.1 Actuators in Autonomous Robots . . . 1
- 1.2 Contributions . . . 2

2 Survey of Artificial Muscles **3**
- 2.1 Pneumatic Artificial Muscles . . . 3
- 2.2 Shape Memory Alloys (SMAs) . . . 6
- 2.3 Electroactive Polymers (EAPs) . . . 7
- 2.4 Electrostatic Actuators . . . 11
- 2.5 Comparison – Superiority of Electrostatic Actuators . . . 17
- 2.6 Concluding Remarks . . . 19

3 A Large-scale Stacked-type Electrostatic Actuator (LSEA) **21**
- 3.1 Basic Concept . . . 21
- 3.2 Characteristics . . . 23
- 3.3 Concluding Remarks . . . 29

4 Prototypes **31**
- 4.1 Electrode Film . . . 31
- 4.2 Fabrication Process . . . 32
- 4.3 Adhesion Improvement . . . 37
- 4.4 Prototypes . . . 41
- 4.5 Concluding Remarks . . . 44

5 Spring Characteristics **45**
- 5.1 Measuring Instrument . . . 45

5.2 Prototype A 49
5.3 Prototype B 51
5.4 Concluding Remarks 60

6 Actuation Characteristics **61**
6.1 Contraction Ratio 61
6.2 Responsiveness 68
6.3 Generative Force 75
6.4 Concluding Remarks 87

7 Power Consumption **91**
7.1 Measurement Method 91
7.2 Steady Current 92
7.3 Power Consumption 92
7.4 Power Consumption in Vacuum 95
7.5 Concluding Remarks 95

8 Simulation **97**
8.1 Outline 97
8.2 Modeling 98
8.3 Simulation Method 107
8.4 Examples of the Simulation 109
8.5 Concluding Remarks 115

9 Conclusion **117**
9.1 Summary 117
9.2 Future Work 120

Appendix **121**
I Pull-in Phenomenon 121
II Electrostatic Force Generated in a Parallel Plate Electrode Laminated by a Solid Insulator 123
III Large Deflection of a Cantilever Beam 125
IV Tensile Test of the PET Film and the Electrode Film 128

References **132**

Listing of figures

2.1.1 Operation principle of McKibben actuators. [1] 4
2.1.2 Straight-fiber-type pneumatic artificial muscle. [2] 5
2.1.3 Robot arm with an artificial muscle driven by EHD pump. [3] . . . 5
2.1.4 Schematics of material crystalline arrangement of an SMA coil spring actuator during actuation. 6
2.3.1 Alpha and beta phases in PVDF, looking along the chains (top) and perpendicular to the chains (bottom). A similar alpha-to-beta phase change is induced in P(VDF-TrFE) relaxor ferroelectrics that begin in the nonpolar alpha phase and switch to the polar beta phase upon the application of an electric field. This results in dimensional changes (expansion along the chain length and contraction perpendicular to the chain direction). 7
2.3.2 Electrostrictive graft copolymer consisting of P(VDF-TrFE) main chain and PVDF grafts. Polar aggregate and form crystallites that serve as polarizable moieties for actuation and as physical cross links between elastomer chains. 8
2.3.3 Operating principle of dielectric elastomer. When a voltage is applied across an elastomer film coated on both sides with compliant electrodes, Maxwell stress act to compress the film in the thickness direction and expand it in plane. 9
2.3.4 Stacked linear contractile actuator configurations. From left to right: stacked type, helical type and folded type. 10
2.4.1 Electrostatic film motor. 12
2.4.2 Distributed Electrostatic Micro Actautor (DEMA). 13

2.4.3 Dielectric breakdown voltage based on Paschen effect and field emission in air for bear metal electrodes. (a) Maximum voltage versus gap spacing. (b) Maximum field strength versus gap spacing. The shade region denote the safe design limits. 15
2.4.4 Different spring characteristics of electrostatic actuators in the same electrostatic force. (A) Hard spring, (A') soft spring, and (B) soft and hard spring. 17

3.1.1 Schematic and drive principle of a two-layer LSEA. 22
3.2.1 Deformation of the hinge part. 24
3.2.2 The hinge part considered as a cantilever beam (left). When the LSEA elongates under a tensile force F, the cantilever beam is subjected to the force F in the tensile direction of the LSEA (right). . 24
3.2.3 Spring characteristics of a cantilever beam. The left graph shows the relationship between the displacement and the applied tensile force and the right graph shows change of the spring constant. . . 25
3.2.4 Longer LSEA stroke can be achieved by multi-stacking. 26
3.2.5 Large LSEA electrode area can be achieved using n×n electrode films. 26
3.2.6 An example of realizable configurations. These LSEAs can be made by stacking triangular, circular and annulus-shape electrode films starting from the left figure. The checkered pattern on the top electrode films shows their adhesive pattern. 29

4.1.1 Schematic of the electrode film. 32
4.1.2 Laser ablation system. 32
4.2.1 Pristine electrode film (left) and the electrode film after cutting (right). 33
4.2.2 Cut electrode film (left) and etched film (right). 33
4.2.3 Mask for adhesive printing. 34
4.2.4 Jigs and stamp for adhesive printing. The left one is a flat plate to precisely allocate a stamp and a mask. The middle one is a mask made by teflon. The right one is a cover plate to fix a mask. 34
4.2.5 Schematic of the printing process of the adhesive with masks and a stamp. 35

4.2.6 (a) Electrode film allocated by the knock pins. (b) Appearance of transcription of the adhesive into the teflon plate with the mask. (c) Appearance of transcription of the adhesive into the electrode film. 36
4.2.7 The stacked electrode films. 36
4.2.8 Schematic showing the position misalignment of the mask. 36
4.2.9 The printed adhesive pattern and quadrilateral hole (left) and its schematic (right). 37
4.3.1 Schematic of UV-ozone processing. 39
4.3.2 Change of the wettability of a PET film. 40
4.3.3 Schematic of peeling test. 40
4.3.4 Electrode film during T-peel test. 41
4.3.5 Change of the adhesion force between the adhesive and the electrode films with and without UV-ozone processing with respect to time. 41
4.4.1 Prototype used for investigating the spring characteristics (Prototype A). 42
4.4.2 50-layer LSEA with external stoppers (Prototype B). 43
4.4.3 Jig for attachment of the external stoppers and Prototype B (left) and its enlarge view (right). 43

5.1.1 Appearance of the F-d measuring instrument for Prototype A. . . 46
5.1.2 Appearance of the F-d measuring instrument for Prototype B. . . 47
5.1.3 Schematic of the setup for measurement in vacuum. 48
5.1.4 Appearance of the vacuum vessel. 48
5.1.5 Schematic of the displacement measurement by the laser displacement meter. 49
5.2.1 Spring characteristics of Prototype A. 50
5.3.1 Relationship between the elongation of the prototype and the travel distance of the movable stage. 52
5.3.2 Change of the elongated length of the prototype with respect to the degree of vacuum. The length in atmospheric pressure was set as a standard (0 mm). 53
5.3.3 Spring characteristics in the different degree of vacuum. 55
5.3.4 Change of the spring characteristics with respect to the degree of vacuum. 56

5.3.5 Spring characteristics for the contraction and elongation speed of of 50 μm/s and 500 μm/s in atmospheric pressure and vacuum. . . . 59
5.3.6 Spring constants during elongation and contraction, and their average ('Overall' in the graph). 59

6.1.1 Prototype B at the deactivated state (left) and the activated state (right). The prototype lifted a load of 1.15 N at 250 V. 62
6.1.2 Relationship between the contraction ratio and the applied voltage in atmospheric pressure. 63
6.1.3 The contraction ratio as a function of the load weight and the calculated generative force. 63
6.1.4 Relationship between the contraction ratio and the applied voltage in vacuum. 65
6.1.5 Difference of the initial stretch length of the prototype between in atmospheric pressure and a vacuum. 66
6.1.6 Relationship between the contraction ratio and the storage condition of the prototype. 67
6.1.7 Relationship between the contraction ratio and the initial stretch length at 300 V. 67
6.2.1 Waveform of the applied voltage and the contraction ratio. 69
6.2.2 Comparison of the contraction ratio at the different loads. 69
6.2.3 Comparison of the contraction ratio in atmospheric pressure and vacuum (upper) and their difference (bottom). 71
6.2.4 Comparison of the contraction ratio in atmospheric pressure and vacuum under contraction time of 25 s. 71
6.2.5 Comparison of the contraction ratio under the different time of application of 300 V. 73
6.2.6 Changes of the contraction ratio and the stroke with respect to the contraction time in atmospheric pressure and a vacuum. 74
6.3.1 Generative force at 300 V after a lapse of 12.5 s as a function of the gap between the electrodes in atmospheric pressure. 77
6.3.2 Average generative force at 300 V after a lapse of 12.5 s as a function of the gap between the electrodes in atmospheric pressure and the curve of the calculated electrostatic force. 77

6.3.3 Potential energy of a two-layered electrostatic actuator with respect to the air gap ($d - d'$). 79
6.3.4 Schematic of the multi-layered electrostatic actuator whose electrodes are connected with the adjacent electrode by a spring k. (i) Initial condition, (ii) a state under contraction of a layer (the $i - 1$ layers already have been completely contracted) and (iii) a state where the i layers have been completely contracted. 80
6.3.5 Generative force of calculated model (pull-in model and no pull-in model) and the experiment result. 82
6.3.6 Calculated potential energy of 50-layered actuator at $d = 24\mu$m and $i = 20$. 83
6.3.7 Generative force at 300 V after a lapse of 12.5 s as a function of the gap between the electrodes in the different degree of vacuum. . . . 85
6.3.8 The generative force after a lapse of 12.5 s as a function of the degree of vacuum. 86
6.3.9 The generative force after a lapse of 60 s as a function of the degree of vacuum. 86
6.3.10 The generative force at 300 V after a lapse of 2.5 s as a function of the degree of vacuum. 87
6.3.11 Change of the generative force under the different degree of vacuum. 88

7.3.1 Power consumption in the different average gaps between the electrode parts for 10 s starting from the application of 300 V (left graphs) and 180 s (right graphs). 93
7.3.2 Change of the capacitance with respect of time of application of 300 V (0-10 s). 94
7.3.3 Change of the capacitance with respect of time of application of 300 V (0-180 s). 94
7.4.1 Power consumption in the different average gaps between the electrode parts for 10 s starting from the application of 300 V (left graphs) and 180 s (right graphs) in vacuum. 96

8.1.1 Outline of the simulation. 98
8.2.1 Schematic of electrode parts and electrode units with the part names. 99

8.2.2 Arranged electrode units. 100
8.2.3 A variety of deformed hinges and the forces acting on the electrode parts at the time. 101
8.2.4 Schematic of the actual hinge parts (left) and the simulated hinge model (right). 101
8.2.5 Gravity of the electrode unit, and a force and a torque resulting from the elasticity of a hinge part. 102
8.2.6 Force and torque acting on the hinge part (left) and force and torque acting on the electrode units (right). 104
8.2.7 Electrostatic force and the distances d_i $(i = 1, 2, 3, 4)$ between the corners of the electrode units. 105
8.3.1 Flow chart of the physics engine. 108
8.4.1 Elongation simulation of a 6-layered 3×1 LSEA with a load of 1 g. The time represents the elapsed time. The scale of elongation direction is doubled. 110
8.4.2 Elongation simulation of a 6-layered 3×1 LSEA having 20 % variability of the hinge length with a load of 1 g. The scale of elongation direction is doubled. 111
8.4.3 Elongation simulation of a 11-layered 7×7 LSEA with a load of 10 g. The time represents the elapsed time. The scale of elongation direction is decupled. 112
8.4.4 Calculated spring characteristics of a 6-layered LSEA without variability. 113
8.4.5 Contraction simulation of a 6-layered 3×1 LSEA with a load of 0.1 g at 100 V. The time represents the elapsed time. The scale of elongation direction is decupled. 114

I.1 Schematic of a parallel plate electrode connected with a linear spring. 122
II.1 Schematic of a parallel plate electrode with a solid insulator in an insulating fluid. 123
III.1 A cantilever beam bended by the concentrated vertical force P and horizontal force Q at the free end. 126
IV.1 Results of the tensile test of the PET film and the electrode film. . 128

To my treasured family.

Acknowledgments

I would like to express my special appreciation and thanks to my advisor Associate Professor Keiji Saneyoshi, who has been a tremendous mentor for me. I would like to thank you for encouraging my research and for bring me to a higher level of thinking. All your advice have been priceless. Without his guidance and persistent help this dissertation would not have been possible.

I would also like to thank my committee members, Professor Toshiaki Shibata, Professor Fumio Kakimoto, Professor Takashi Nakamura, Associate Professor Kentaro Somiya for serving as my committee members in your hectic schedule. I also want to thank you for letting my defense be an enjoyable moment, and for your brilliant comments and suggestions.

Moreover, I want to give gratitude to Assistant Professor Katsunori Kawasaki and Professor Toshiyuki Hattori who provided insightful comments, technical help and sincere encouragement. Both of them have been busy with their own work, but they were willing to give their helping hands as soon as I was in need.

Last but not least, the various members of Saneyoshi lab. provided me a lot of valuable advice and spent their precious time to discuss with me. I am especially grateful to Kosuke Yamamoto, Shinichi Kakegawa, Yoshihiko Matsubara, Takashi Nakamura, Ryusuke Suzuki, Takehiko Okumura, Kunihiko Hosono and Syungo Chino. I am a lucky person to have met them.

1 Introduction

Actuators transduces a source enery typically electricity, fluid pressure, heat, etc. into motion or force. They are the most important machine elements to determine physical capability of robots. Conventional actuators are used in manufacturing or industrial applications and might be used in devices such as motors, pumps, switches and valves. These applications often require large forces and positional accuracy regardless of the weight and the rigidity of actuators. Then, what characteristics will be needed for robots working in our living environment?

1.1 Actuators in Autonomous Robots

The development of autonomous robots and power assist suits constitutes one of the major trends in the current research of robotics. With this trend, developing high performance actuators is becoming more important because they determine the kinematic performance. Their actuators should be lightweight in order to be efficient and safety, as well as having a large force and long strokes (motion ranges) to work like a human. Therefore, actuators unlike conventional actuators (like

human muscles) will be needed to use autonomous robots and power suits in our living environment.

The following chapters will discuss the current field of artificial muscles through a basic survey, explain our newly-developed electrostatic actuator with the remarkable characteristics and the fabrication process, and investigate the actuation characteristics.

1.2 Contributions

This work builds on the field of electrostatic actuators. Specifically:

- Chapter 2 presents a basic survey of the current artificial muscles such as pneumatic actuators, shape memory alloys, electroactive polymers, and electrostatic actuators.
- Chapter 3 details a structure, characteristics and a fabrication process of a large-scale stacked-type electrostatic actuator (LSEA) which is newly-developed.
- Chapter 4 details the fabrication process of prototypes. LSEAs require high adhesion force for the adhesive used to connect the electrodes. This chapter also shows the adhesion improvement method.
- Chapter 5 shows the spring characteristics of two different prototypes in order to evaluate the compliance of LSEAs for use as artificial muscles.
- Chapter 6 exhibits experiments results of the actuation characteristics such as the contraction ratio, the responsiveness and the generative force.
- Chapter 7 reveal the power consumption and discuss the reason of the energy loss.
- Chapter 8 shows a fundamental concept in order to simulate the motion of LSEAs.

2

Survey of Artificial Muscles

Combustion engines and electric motors have been widely used in various industrial equipments, transport machineries, home electric appliances etc., and even now, play an extraordinary role in the development of our civilization. They have enabled to realize a lot of machines and robots which moved quickly, precisely and reproducibly, but on the other side of the coin, they have restricted the structure of machines. For example, engines and motors are generally the most energy efficient when operated continuously and therefore it is difficult to make high efficient valves or walking robots whose motion is frequently interrupted. Furthermore, their hard and heavy structures have sacrificed the flexibility and power-weight ratio of robots. In this chapter, we discuss various types of actuators and their advantage and disadvantage with the object of artificial muscles of robots.

2.1 Pneumatic Artificial Muscles

Pneumatic artificial muscles are membranes that can expand radially and contract axially when inflated by pressurized air, and generate pulling forces along the lon-

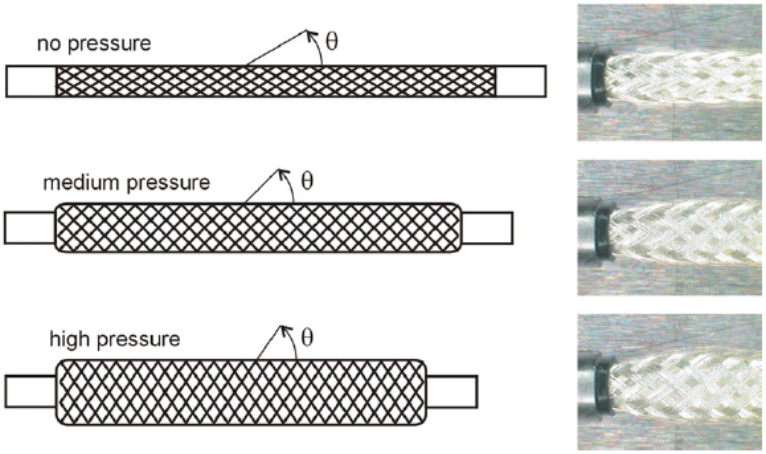

Figure 2.1.1: Operation principle of McKibben actuators. [1]

gitudinal axis. The best known is the so called McKibben actuator. Basically McKibben actuators consist of a rubber tube which is reinforced by a woven structure. Upon pressurization, the rubber tube will expand, resulting in a contraction of the actuator length due to the geometrical constraints of the woven structure (see Figure 2.1.1). Hysteresis, owing to dry friction between the woven thread and the rubber tube, makes control of the actuators rather complicated [1].

Another type of pneumatic artificial muscle is a straight-fiber-type artificial muscle consisting of a natural latex rubber tube with a carbon fiber sheet (see Figure 2.1.2) [2]. Because the carbon fiber sheets are inserted in the longitudinal direction, fixing at either end by a terminal, the artificial muscle exerts a contractile force axially. The straight-fiber-type muscles surpassed a McKibben-type muscles in contraction force and contraction ratio because the fiber sheets in the straight-fiber-type muscles restrict expansion only in the axial direction, whereas the McKibben actuator is restricted by the woven structure not only in the axial direction but also in the radial direction. A 180-mm long straight-fiber-type artificial muscle of 10 mm in inner diameter demonstrates about 1.6 kN of contraction force at a pressure of 0.5 MPa and over 35 % of contraction ratio at 0.3 MPa [2].

Generally, pneumatic artificial muscles have some strong point such as lightweight, flexibility and safety. However, pneumatic actuators are not suitable for artificial muscles of autonomous robots such as walking robots because the actuators re-

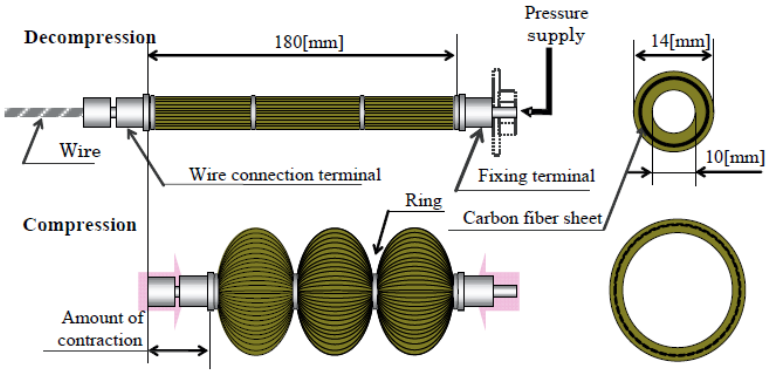

Figure 2.1.2: Straight-fiber-type pneumatic artificial muscle. [2]

quire a heavy and noisy compressor supplying pressurized air to them, eventually making the system heavy.

As an approach to eliminate compressors, Mitsui et al., created an artificial muscle utilize Electro Hydro Dynamics (EHD) phenomenon as a pumping system of fluid [3]. When an insulating fluid is exposed to an electric field, it experiences an additional hydrodynamic force of electric origin, referred to as EHD force [4]. EHD force can generate a jet stream of fluid in some situations depending on the type of fluid, applied voltage and configuration of electrodes. The hydrodynamic-driven muscle (see Figure 2.1.3) generates the maximum pressure of 800 kPa as a momentary value and about 500 kPa stably [3]. However, the applied voltage was very high ranged from several kilovolts to over 10 kV.

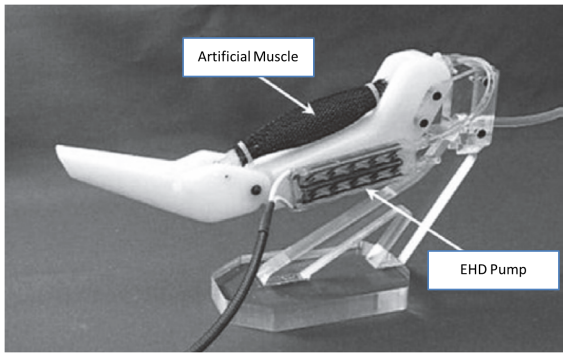

Figure 2.1.3: Robot arm with an artificial muscle driven by EHD pump. [3]

2.2 Shape Memory Alloys (SMAs)

Shape memory alloy (SMA) actuators work by reversible phase transitions as a result of temperature. At low temperature, they have a martensite structure, which is characterized by a monoclinic lattice which looks like a parallelogram. On the other hand, they change the crystal structure to a cubic lattice, called austenite, at high temperature. There is hysteresis in the phase transition due to initial friction between the two phases. The width of the hysteresis is typically 10 - 15 degrees C [5].

Deformed SMAs at a lower temperature will regain its original undeformed shape when heated to a higher temperature as shown in Figure 2.1.4. In the recovering process to austenite structure, they generate high stresses between 140 - 345 MPa [6], whereas they can be deformed with low stresses ($\sim$ 70 MPa) at low temperature. However, repeatedly using the higher stresses can cause eventual failure of the material.

Electrically actuated SMA is easily controllable, working by resistive heating caused by passing current through the material. However, the actuation is fairly slow ($\sim$ 10 Hz) because of a thermal process although the actuation speed can be increased by actively cooling with water or compressed air. As a result, most actuators are made with thin wire of 25 - 500 μm in diameter or thin films in order to heat up and cool down them faster. SMA actuators also suffer from the disadvantage of low energy efficiency (which is also common issue of heat-driven

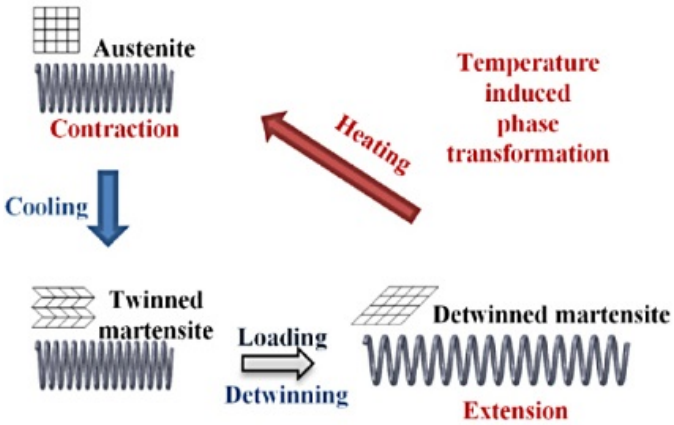

Figure 2.1.4: Schematics of material crystalline arrangement of an SMA coil spring actuator during actuation.

actuators).

In addition, the strain is generally small because of the risk of dislocations preventing full shape recovery. For example, the material strain recovery for nickel-titanium alloys (generally referred to as Nitinol) has a limit of 8 %. Nitinol alloys are popular because of the high ductility, more recoverable motion, excellent corrosion resistance, stable transformation temperatures, high biological compatibility and electrical drivability [5].

2.3 Electroactive Polymers (EAPs)

Electroactive polymers demonstrate some physical change in response to an electric stimulus, categorized into electronic EAPs and ionic EAPs by the change principle. Electronic EAPs are changed by electric fields and coulomb force, or ionic EAPs are changed as a result of the movement of ions [7]. Here, we cover only electronic EAPs which generate large stress and large strain.

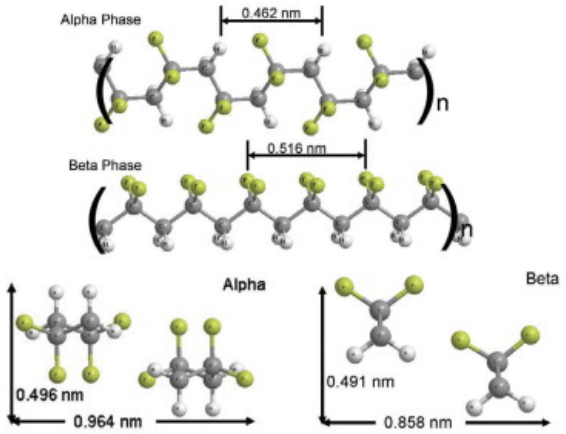

Figure 2.3.1: Alpha and beta phases in PVDF, looking along the chains (top) and perpendicular to the chains (bottom). A similar alpha-to-beta phase change is induced in P(VDF-TrFE) relaxor ferroelectrics that begin in the nonpolar alpha phase and switch to the polar beta phase upon the application of an electric field. This results in dimensional changes (expansion along the chain length and contraction perpendicular to the chain direction).

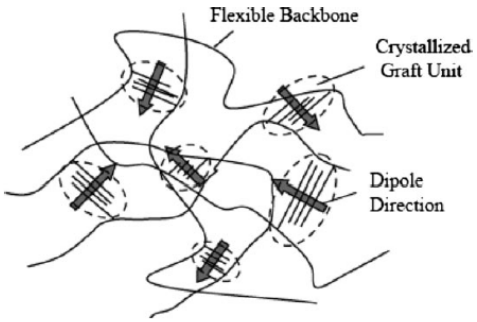

Figure 2.3.2: Electrostrictive graft copolymer consisting of P(VDF-TrFE) main chain and PVDF grafts. Polar aggregate and form crystallites that serve as polarizable moieties for actuation and as physical cross links between elastomer chains.

2.3.1 Piezoelectric Polymers

Piezoelectric polymers have a non-centro-symmetric structure that result in the polymer chain being polarization [8]. They will change phases in order to align their dipoles with an applied electric field. The polarization is reversible by applying a high opposite electric field, or by heating the polymer above its Curie temperature. As the most common piezoelectric polymer material, polyvinylidene fluoride (PVDF, see Figure 2.3.1) is widely used because of the excellent electromechanical response at room temperature [9]. PVDF exhibits 3 MPa of the maximum stress and 0.1 % of the strain at 30 V/μm [10]. The drawback is the hysteresis and the small strain as well as piezoelectric ceramics.

2.3.2 Electrostrictive Polymers

Electrostrictive polymers have randomly aligned polar crystalline domains within an amorphous of flexible material. With an applied electric field, the polar domains attract each other, reducing material thickness in the direction of the applied field (and increasing thickness in the orthogonal directions). These materials take advantage to achieve higher strain than piezoelectric polymers. The typical material is poly(vinylidenefluoride-co-trifluoroethylene) P(VDF-TrFE) which is PVDF copolymerized with trifluoroethylene as shown in Figure 2.3.2. This shows smaller hysteresis than PVDF [11] and demonstrates about 4 % of the strain with around 22 MPa of the stresses for an electric field of 120 V/μm. The actuation energy

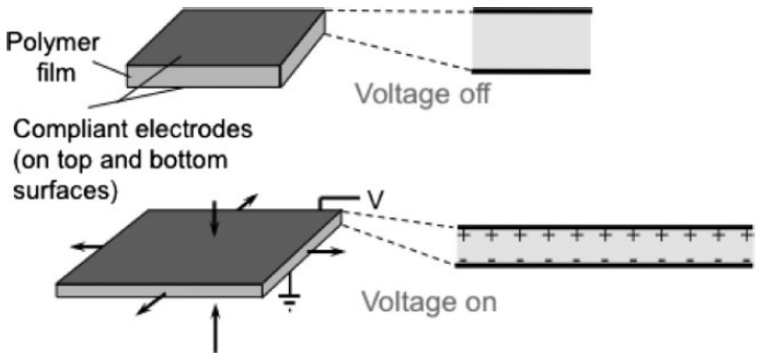

Figure 2.3.3: Operating principle of dielectric elastomer. When a voltage is applied across an elastomer film coated on both sides with compliant electrodes, Maxwell stress act to compress the film in the thickness direction and expand it in plane.

density was 0.44 J/cm^3 [12]. The actuator also suffer from the disadvantage of the small strain although the stress is greatly high.

2.3.3 Dielectric Elastomers

Dielectric elastomer actuators (DEAs) are capacitors with very compliant dielectrics and stretchable electrodes. When a voltage is applied between the electrodes, opposite charges on the electrodes attract each other, compressing the dielectric in the direction of the electric field, and like charges repel each other, increasing thickness in the orthogonal directions as shown in Figure 2.3.3. The induced stress P_M in the dielectric is called the Maxwell stress, and can be represented by,

$$P_M = \varepsilon_r \varepsilon_0 \frac{V^2}{g^2} \tag{2.1}$$

where ε_r is the relative permittivity of the dielectric, ε_0 is permittivity of vacuum, V is the voltage, and g is the thickness of the dielectric. This is exactly twice the electrostatic stress developed between two parallel plates with rigid electrodes. The factor of two is due to the incompressibility of the elastomer film and the repulsive force expanding the electrodes in the transverse direction [13].

For DEAs, the material properties of the dielectric are very important to the actuator performance. The typical materials, used widely, are acrylic elastomers and silicone rubbers. Actuators made out of acrylic elastomers, such as 3M's VHB

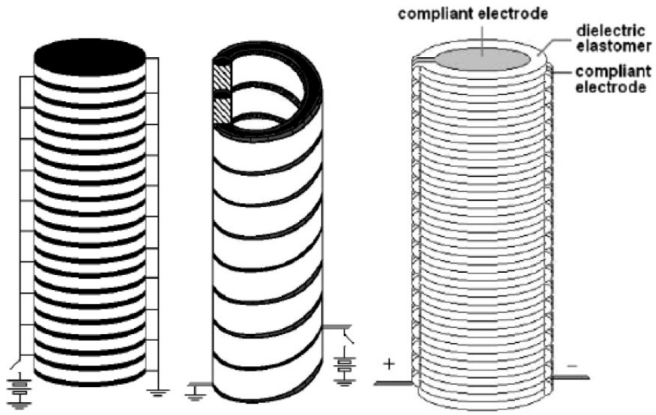

Figure 2.3.4: Stacked linear contractile actuator configurations. From left to right: stacked type, helical type and folded type.

4910, show the highest strain of 380% in area, pressure of 7.2 MPa and energy densities of 3.4 J/g [8]. On the other hand, the less viscoelastic silicones have a maximum strain of 63 % in area, maximum pressure of 3 MPa and actuation energy density of 0.75 J/g [8]. These results appear to exhibit that DEAs are capable to generating large strain and large force beyond the performance of biological muscles. However, they have some practical problems as artificial muscles.

The highly compliant dielectric allows large elastic strain. However, in practice, DEAs with the larger strain ($> 380\%$) suffer severely from creep. The creep prevents them from holding static loads because of pull-in failure (dielectric creeps until the field reaches breakdown), and causes large losses at low frequency (90 % at 10 Hz) [14]. In addition, a flexible electrode is necessary in order to maintain electrical continuity under very high strain because the dielectrode is incompressible. CNT films can maintain conductivity at 200 % area strain because their high aspect ratio results in percolation at very low concentrations [15]. However, because of the sharp shape of the CNTs, high fields can develop at exposed tips, causing discharge through the air. Furthermore, due to viscoelastic problems, DEAs need to be fairly thick to avoid breakdown at high fields ($> 200\text{V}/\mu\text{m}$), and this translates into large voltages ($> 1\text{kV}$). Therefore, DEAs having large strain are hard to maintain the performance due to the creep phenomenon and the risk of discharge. It is also difficult to reduce the large voltage with maintenance of the high pressure.

2.4 Electrostatic Actuators

The simplest electrostatic actuator is a pair of parallel electrode plates. When a voltage is applied between the two electrodes, an electrostatic force is generated, which moves the electrodes. The electrostatic actuators can be divided into two types, 'transverse-motion type' whose electrodes move in the in-plain direction of the electrodes, and 'longitudinal-motion type' whose electrodes move in the out-of-plain direction of the electrodes. In general, electrostatic actuators have advantage as described below.

Lightweight – They are lightweight because the insulator has a specific gravity of about 1 and the electrode can be thin. Since electrostatic force is a surface force, the thickness of the electrode can be reduced without changing the electrostatic force.

High-energy efficiency – Mostly no current flows in the actuators due to the voltage driving when they keep holding a load at the same position. Their energy consumption is mostly zero if the electrode interval is constant. Only negligible minute current flows in them such as current flowing in the insulator in practice.

High response – They makes the electrostatic force shortly after the application of a voltage.

Low cost – They can be made without using rare metals, unhealthy materials, ungreen materials or other high-cost materials.

Electrostatic actuators have been actively researched with the development and spread of microelectromechanical systems technology since 1990, and they are presently mostly used as microactuators on Si and other hard substrates in devices such as micromirrors [16, 17], microgrippers [18], microrelays [19], micromanipulators [20], micromechanical probes [21], optical modulators [22], and tunable photonic resonators [23]. This is because the electrostatic force density becomes high as the size (and the gap between the electrodes) decreases. However, electrostatic actuator has a potential to be used as artificial muscles of robots as is described below.

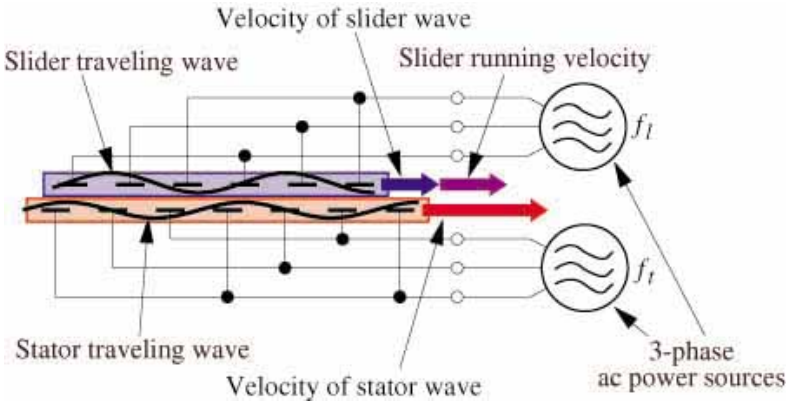

Figure 2.4.1: Electrostatic film motor.

2.4.1 Transverse-motion Type

The electrodes in this type of actuator attract each other by application of a voltage and move in their in-plain direction. The electrostatic force acting in the actuation direction is proportional to the inverse of the gap d between the electrodes:

$$F \propto \frac{\varepsilon w V^2}{d}. \tag{2.2}$$

where ε denotes the electric permittivity of vacuum, w denotes the width of the electrode and V denotes the applied voltage.

Higuchi et al., created an electrostatic film motor aim to use it as artificial muscles [24]. This actuator has two similar electrodes containing a lot of slim-line electrodes arranged in the in-plain direction as shown in Figure 2.4.1. One of the electrode acts as a stator (connected with the body of a robot) and the other one acts as a slider (connected with the arm or the leg of a robot). By applying positive and negative voltage sequentially to the stator and the slider with the same frequency, but different phases, the slider moves with respect to the stator. The actuator achieved high generative force of 1.8 kN/m^2 (force over total electrode area) at 2.5 kVrms [24–26].

The films can be made arbitrarily long to achieve specific stroke lengths. By stacking the stators and sliders alternatively, the actuator has large generative force in proportion of the number of layers. This actuator, however, cannot maximize the advantage of the high-energy efficiency as an electrostatic actuator because the

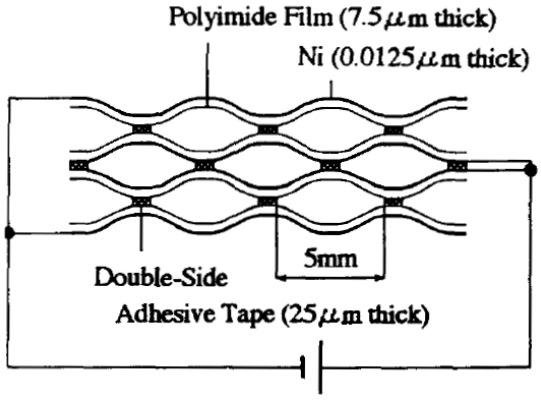

Figure 2.4.2: Distributed Electrostatic Micro Actautor (DEMA).

electric current keeps flowing at all time in activated state due to the alternating voltage driving. The actuator also need glass beads between the electrodes in order to reduce the friction [27]. This makes difficult to achieve high force at low voltage and high durability.

2.4.2 Longitudinal-motion Type

The simplest longitudinal-motion type actuator consists of two parallel electrodes supported by some spring elements. This type of actuator is driven in the out-of-plain direction (stacking direction) along the direction of the electric field. In case that the electrodes collide with each other by pull-in (see Appendix I), the electrodes have to be laminated with an insulator. The electrostatic force is inversely proportional to the square of the gap d between the electrodes:

$$F \propto \frac{\varepsilon S V^2}{d^2}. \tag{2.3}$$

where S represents the area of the electrode. Stroke lengths can be longer by increasing the number of layers of the electrode films. Therefore, the multi-layered actuator can achieve the long stroke and large force at the same time by shortening the gaps between the electrodes if it has proper spring elements between the electrodes (as will hereinafter be described in detail). In addition, this type generates no friction between the electrodes. The actuator also maximize the energy efficiency due to the direct voltage driving.

Minami et al., created a stacked-type electrostatic actuator, called the Distributed Electrostatic Micro Actuator (DEMA) [28]. This actuator consists of metalized polyimide films connected with each other by double-side tapes, fabricated by using photolithography and electroplating as shown in Figure 2.4.2. The micro scale model had an estimated stress of about 420 Pa and less than 1 % strain at 200 V [28]. The lower contraction ratio is due to the higher stiffness of the metal structure. If the electrode becomes more flexible, the actuator however appears to lose the generative force due to overextension of the electrode intervals in our projection.

2.4.3 Dielectric Breakdown

Generative pressure (force density) of electrostatic actuators is dependent upon the electric field. The maximum generative force is therefore limited by the dielectric breakdown voltage. If the dielectric is a gas, electrostatic discharge may occur either through avalanche breakdown or as a result of field emission. For air, the breakdown field is 3 V/μm under normal conditions [29], which seems as an drawback of electrostatic actuator. However, in order to cause avalanche breakdown, electrons must be gain sufficient energy to ionize the atoms that they collide with, initiating a cascade of current flow. This indicates that avalanche breakdown is influenced by the mean free path of the molecules in air. The Paschen's law gives a breakdown voltage V_b as a function of the product of the gas pressure p and the gap between electrodes y as is given by

$$V_b = \frac{Bpy}{\ln(py) + k}, \tag{2.4}$$

where B and k are experimentally determined constants that depend on the gas and electrode material which is used, e.g. for air with platinum electrodes, $B = 2737.5\text{V}/(\text{kPa} \cdot \text{cm})$ and k depends on the value of py [30]:

$$k = 2.0583(py)^{-0.1724} \quad \text{for } 0.0133 \leq py \leq 0.2 \text{ kPa} \cdot \text{cm},$$

$$k = 3.5134(py)^{0.0599} \quad \text{for } 0.2 \leq py \leq 100 \text{ kPa} \cdot \text{cm},$$

$$k = 4.6295 \quad \text{for } 100 \leq py \leq 1400 \text{ kPa} \cdot \text{cm}.$$

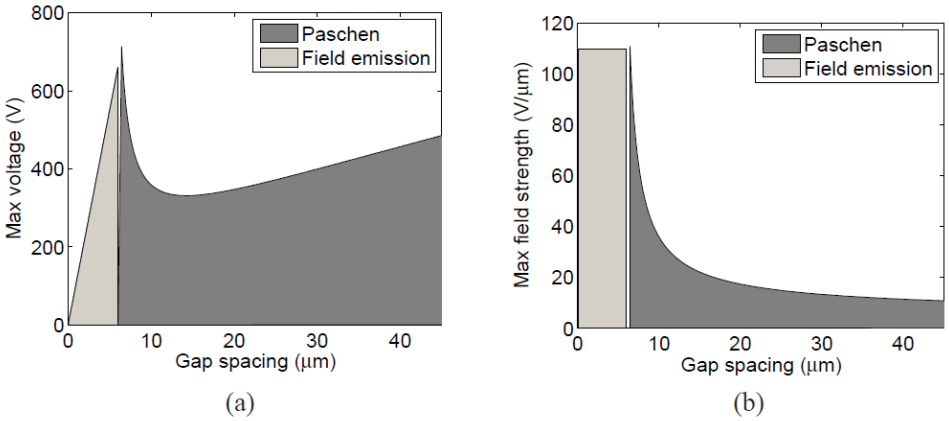

Figure 2.4.3: Dielectric breakdown voltage based on Paschen effect and field emission in air for bear metal electrodes. (a) Maximum voltage versus gap spacing. (b) Maximum field strength versus gap spacing. The shade region denote the safe design limits.

With the given constant, about 330 V is obtained as a minimum breakdown voltage when $py = 0.14\text{kPa} \cdot \text{cm}$, corresponding to a gap of 14 μm at a pressure of 1 atm, or 24 V/μm as an electric field (see Figure 2.4.3).

The Paschen model predicts that after the minimum voltage, the breakdown voltage increases sharply because the mean free path of air is on the same order as the gap size. However, deviations from the Paschen's curve have been reported in microgaps [31, 32]. Radmilović-Radjenović et al., pointed out that the reason is the increase of the secondary electron emission yield due to the quantum tunneling of electrons from the metal electrodes to the gap phase [33]. As it indicates the relationship between the surface state and the breakdown voltage, entirely different results were reported about the breakdown voltage in microgaps in two different electrodes.

Slade found that as an iron needle approached a silver electrode, the Paschen effect lost relevancy when the gap reached 6 μm [34]. After this point, the breakdown voltage was linear with gap spacing g,

$$V_b = Kg \tag{2.5}$$

where K is an experimentally determined constant. For the particular case examined by Slade, K was between 65 and 110 V/μm. This constant represents the

maximum electric field for gaps less than 6 μm. The K value is dependent on the electrode material used and the surface roughness [34].

By contrast, Horn and Smith were able to achieve field strength up to 2300 V/μm with silver electrodes coated in mica and silicon, and having an air gap less than 1 μm, and the maximum field decreased to 600 V/μm as the gap was increased to 3 μm [35].

As is explained later, our newly-developed actuator consists of electrodes completely laminated with an insulator which are closer to the latter electrode configuration of electrode-insulator-air-insulator-electrode. According to Horn's study, insulated electrodes in microgaps could have high breakdown characteristics over 500 V/μm and generate high pressure over 1.1 MPa surpassing that of biological muscles. This indicates that breakdown characteristics in air will be perfectly acceptable for electrostatic actuators to achieve high force density.

2.4.4 Spring Characteristics

Here, we focus on longitudinal-motion actuators and their spring characteristics. For longitudinal-motion actuators, spring characteristics between the electrodes are very important factor to determine the actuation performance. Figure 2.4.4 illustrates the elastic forces of spring elements in a pair of parallel electrode plates (the simplest electrostatic actuators) only whose spring elements are different. Therefore they generate the same electrostatic force when the gap d are the same. The horizontal axis denotes the gap between the electrodes. The vertical axis represents force (the positive sense is defined as contraction for electrostatic force and elongation for elastic force).

If spring element is hard (see (A) in the graph), a large amount of work in activation is stored in the spring element, resulting in reduction of output energy. By contrast, Soft spring element stores less energy when the actuator contracts (see (A')). However, the gaps displace easily with a load. This behavior has more serious consequence for multiply-layered actuators that they cannot contract, because wider gaps are widened more by large electrostatic forces acting on the neighbor electrodes, losing the electrostatic force.

To overcome the problem, Saneyoshi et al., proposed unique spring characteristics for spring elements in electrostatic actuators [36]. The proposed spring has

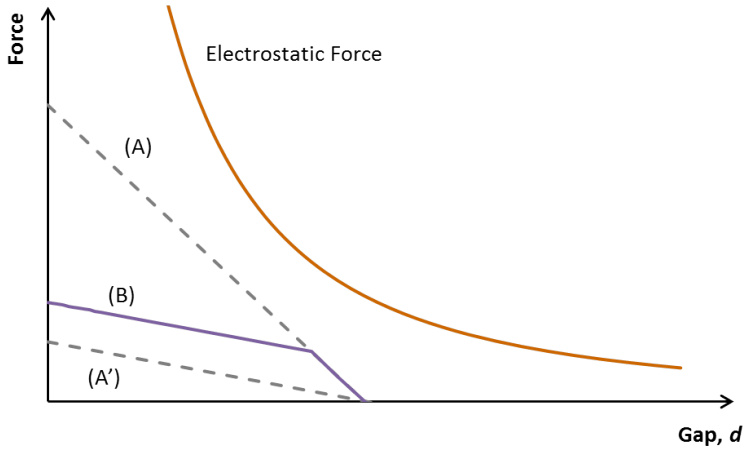

Figure 2.4.4: Different spring characteristics of electrostatic actuators in the same electrostatic force. (A) Hard spring, (A') soft spring, and (B) soft and hard spring.

two spring constant, soft spring constant in a range of short d and hard spring constant in a range of long d as shown (B) in Figure 2.4.4. This spring characteristics prevent the gaps from overextending. They also enable to have stable displacement in the wide range of load weights and achieve high putout energy. Longitudinal-motion electrostatic actuators can easily have the two-phase spring characteristics by some hinge structure [37] due to the very low viscoelasticity of air (or any other fluid surrounding the actuators), i.e. for DEAs, it is difficult to emulate the spring characteristics.

2.5 Comparison – Superiority of Electrostatic Actuators

As shown in table 2.5.1, existing electrostatic actuators have a drawback about the small generative force because their actuation test was carried out in a easily dielectrical breakdown condition, i.e. wide air gap d. In Subsections 2.4.3 and 2.4.4, the advantage of the short air gap d and unique spring characteristics are explained, indicating that longitudinal-motion electrostatic actuators (with multiple layers) have potential to achieve larger force (surpassing that of biological muscles) and long stroke at the same time, also exhibiting some advantages such as lightweight, flexibility, high-energy efficiency, high responsiveness, low cost and durability.

Table 2.5.1: Comparison of actuator materials. [a]Area strain. [e]Estimated value from calculations. [e,p]Calculated value only using volume of a rubber. [f]Effective modulus. [t]Thickness strain. *Modulus faries between 28-40 GPa for martensite and increases to 80 GPa for austrenite [6].

Actuator	Maximum strain (%)	Maximum stress (MPa)	Elastic modulus (MPa)	Electric field (V/μm)	Specific elastic energy density (J/g)	Volume elastic energy density (J/cm^3)	Efficiency (%)	Specific density (g/cm^3)	Frequency (kHz)	References
Pneumatic (straight-fiber-type)	35	1.3[e]	-	N/A	2.2[e]	1.0[e,p]	-	0.45[e,p]	-	[2]
Shape memory alloy (Flesinol)	5	100	>28000*	N/A	0.78	5	<10	6.45	0.01	[6, 10]
Piezoelectric polymer (PVDF)	0.1	3	3000	30	0.0008	0.0015	<1	1.8	1	[10]
Electrostrictive polymer (P(VDF-TrFE))	4.3	43	1000	150	0.49	0.92	∼80	1.8	>10	[8, 9]
Dielectric elastomer (prestrained acrylic)	380[a] 79[t]	7.2	3.0	412	3.4	3.4	60-80	1	0.03	[8, 38]
Dielectric elastomer (unstrained acrylic)	7.5[a] 7[t]	0.16	3.0	17	0.0057	0.0057	-	1	0.03	[8]
Dielectric elastomer (prestrained silicon)	64[a] 39[t]	3.0	1.0	350	0.75	0.75	90	1	2-20	[8, 38]
Dielectric elastomer (unstrained silicon)	32	1.36	1.0	235	0.22	0.2	90	1	2-20	[8, 38]
Electromagnetic (voice coil)	50	0.03	-	-	0.0015	0.0025	>90	8	20	[8]
Electrostatic (integrated force array)	11	0.0082	0.075[f]	65[e]	0.001	0.0009	>90	0.84[e]	-	[39, 40]
Human muscle (skeletal)	>40	0.35	60	N/A	0.067	0.07	>35	1.04	<10	[10]

2.6 Concluding Remarks

In this chapter, several artificial muscles were compared. Each actuator has some advantages, however, also suffers from the disadvantage due to the actuation principle i.e., heavy system for pneumatic actuators, low responsiveness and low efficiency for SMAs, short strain for piezoelectric polymers and electrostrictive polymers, and creep and high actuation voltage for DEAs.

Electrostatic actuators exhibit some remarkable advantages such as lightweight, high-energy efficiency, high responsiveness and low cost. Transverse-motion type electrostatic actuators have already achieved large force and long stroke, however, it is difficult to reduce the applied voltage (similar disadvantage occurs in DEAs) due to friction between the electrodes. By contrast, longitudinal-motion type electrostatic actuators generate no friction between the electrodes. The greatly short gaps between the electrodes can be realized easily as compared to transverse-motion types, enabling to drive the actuator under very high electric field without breakdown. This can be achieved using two-phase spring elements between the electrodes.

In this study, we newly developed a multiply-layered longitudinal-motion electrostatic actuator which has a structure achieving a proper spring characteristics described above. The actuator also has advantage to make large size easily in order to use as artificial muscles.

3

A Large-scale Stacked-type Electrostatic Actuator (LSEA)

A large-scale stacked-type electrostatic actuator (LSEA) has the potential of achieving high force density and long stroke on a macro scale due to the proper spring characteristics. The characteristics are suitable for use as artificial muscles in robots and power-assist suits. Here, we present the basic structure, operation principle, and characteristics.

3.1 Basic Concept

An LSEA consists of multi-stacked electrode films. The electrode film is a thin conducting substance that is completely laminated with thin and flexible insulating films. The electrode films are bonded by an adhesive in a checkered pattern as shown in Figure 3.1.1(a), making bonded areas and unbonded areas. Care should be taken when applying the adhesive on each electrode film in regard to the alternating pattern (see the adhesive pattern on the top and the second top electrode

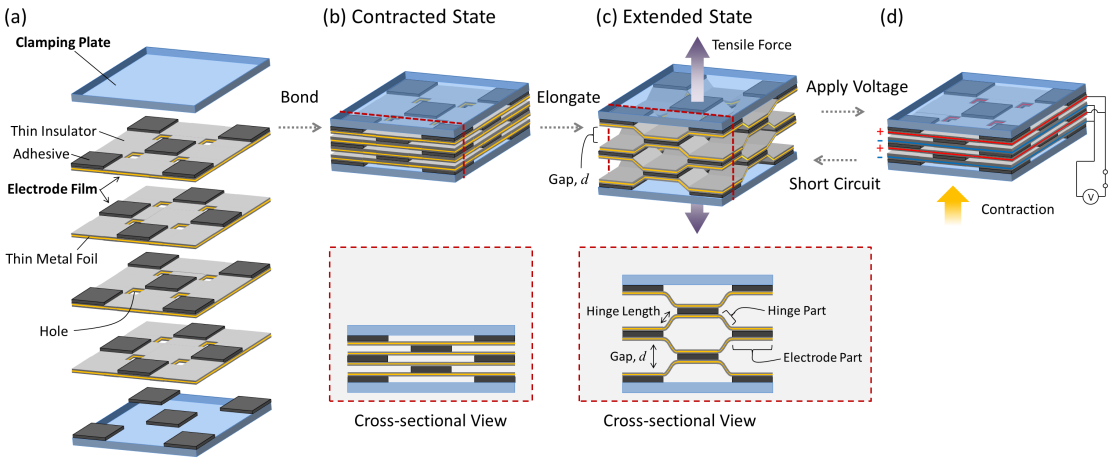

Figure 3.1.1: Schematic and drive principle of a two-layer LSEA.

films in Figure 3.1.1(a)). To connect it to external devices, two clamping plates are bonded on the top and bottom surfaces of the LSEA (Figure 3.1.1(b)). The actuator can be elongated by external tensile force. Figure 3.1.1(c) shows the elongated actuator and its cross-sectional view. Compared to the contracted state, gaps appear between the unbonded areas due to the deformation of parts of the electrode films. In an LSEA, the distorted parts of the electrode films act as hinges – referred to as the hinge parts – and the non-distorted parts act like parallel electrode plates – referred to as the electrode parts. It indicates the insulating films should be a flexible material like a polymer. Here, quadrilateral holes are cut on the electrode films to prevent them from being torn by stress concentration.

An LSEA can be contracted by an electrostatic attractive force when a potential difference is created between each interelectrode by the application of a voltage, i.e. facing electrodes should be charged with unlike charges alternatively. If the electrode intervals are even, the electrostatic force of the LSEA would be equal to that of a layer regardless of the number of layers. Hence, the force generated by an actuator with even electrode intervals can be calculated from the electrostatic force per layer as follows (see Appendix II):

$$F_{\text{elec}}^{\text{LSEA}}(d) = \frac{1}{2}\frac{\varepsilon_0 S V^2}{\varepsilon_2\left(\frac{t}{\varepsilon_1}+\frac{d}{\varepsilon_2}\right)^2}, \tag{3.1}$$

where S [m^2] is the area of the conducting substance per sheet of the electrode films, V [V] is the applied voltage, t [m] is the thickness of the solid insulator per layer, d [m] is the thickness of the insulating fluid per layer (see Figure 3.1.1), ε_0 [F/m] is the electric permittivity of a vacuum, and ε_1 and ε_2 are respectively the relative permittivities of the solid insulator and the insulating fluid. Here, we assumed that the electrode intervals are narrow sufficiently to neglect the electric field at the edge of the electrode parts, and do not take the electrostatic force between the hinge parts into account. Because the actuation force is proportional to the square of the voltage, the response is the same for both negative and positive voltages; i.e., when a sinusoidal voltage is applied with an angular frequency of ω, the actuation response has a frequency of 2ω.

In reality, the electrode intervals vary. The electrostatic force is greater in a narrower gap as indicated by Equation (3.1). Therefore, when a voltage is applied to an LSEA, the narrower gaps contract first, which further expands the wider gaps. The total electrostatic attractive force of the LSEA depends on the expanded gaps, which causes the force to be weaker than that calculated using Equation (3.1), where the gap d is the average of the gaps. On the other hand, change of the positions of the electrode parts by their pull-in phenomenon generates contraction force due to the increment of the elastic force in the hinge parts. The actual generated force of an LSEA is therefore given by the sum of the electrostatic forces acting in the expanded electrode intervals and the increased elastic forces between the hinge parts that result from the contraction of the narrower gaps.

3.2 Characteristics

3.2.1 Spring characteristics

The hinge parts prevent the decrease of the electrostatic force that results from overextension of the electrode intervals. Figure 3.2.1 shows the deformation of the hinge parts in the contracted state, the extension state, and the maximum extended state. The angle between the hinge part and the horizontal line increases when the actuator is acted upon by an external tensile force and elongated in the longitudinal direction (see Figure 3.2.1(b)). At the same time, the LSEA contracts in the transverse direction because the hinge parts are not only under

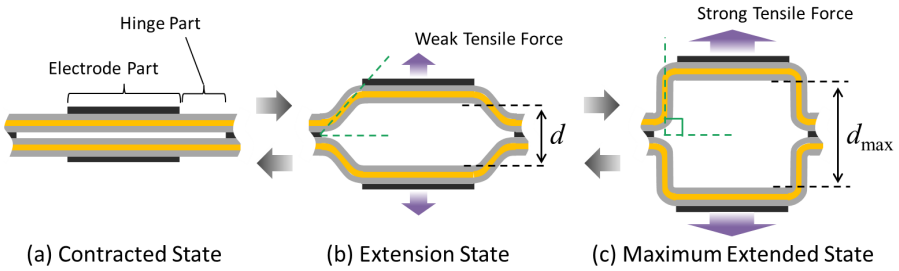

Figure 3.2.1: Deformation of the hinge part.

bending stress but also acted upon by a tensile force that pulls the electrodes in the transverse direction. The spring rate of the hinge parts increases as the external tensile force increases, and the hinge parts can eventually become resistant to further deformation. Unless the adhesive peels off, the electrode intervals cannot extend beyond the maximum gap (see Figure 3.2.1(c)). Therefore, the hinge parts not only connect the electrodes electrically and mechanically, but also prevents overextension of the electrode intervals and reduction of the electrostatic force under $F_{\text{elec}}^{\text{LSEA}}(d_{\max})$.

More quantitatively, deformation of the hinge parts can be calculated approximately by analytical method of deflection of a cantilever beam under tip load. When the rotation of electrode parts is vanishingly small, the hinge part between them behaves as a cantilever beam fixed to the neighbor electrode part and connected with another rotationally symmetric beam (Figure 3.2.2). Here, the contact point between the electrode part and the hinge is considered as its fixed point and

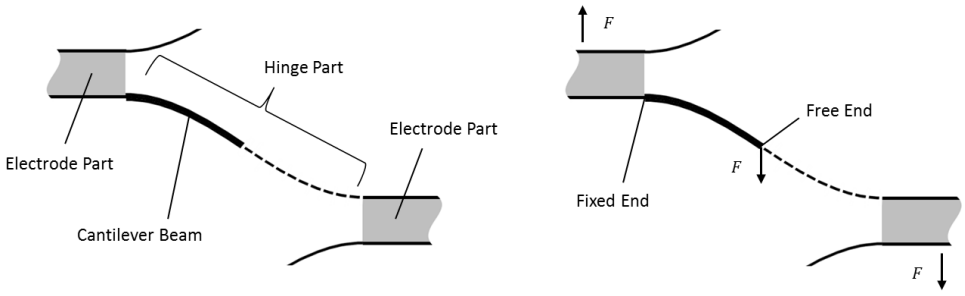

Figure 3.2.2: The hinge part considered as a cantilever beam (left). When the LSEA elongates under a tensile force F, the cantilever beam is subjected to the force F in the tensile direction of the LSEA (right).

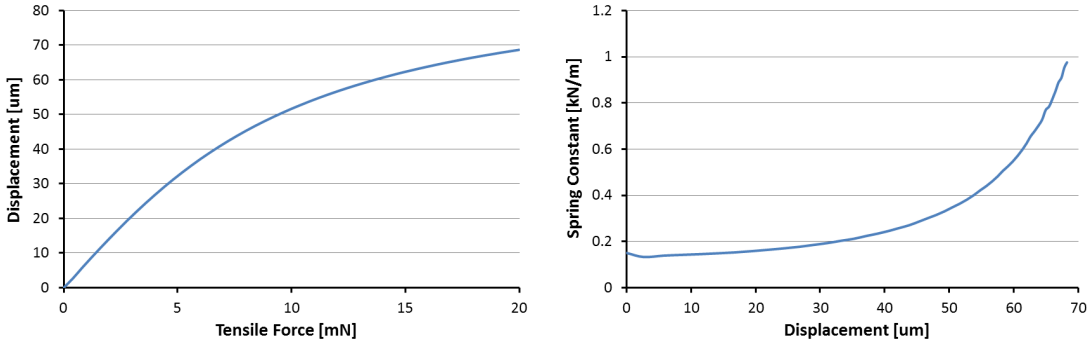

Figure 3.2.3: Spring characteristics of a cantilever beam. The left graph shows the relationship between the displacement and the applied tensile force and the right graph shows change of the spring constant.

the one between two beams as its free end. The deflection is obtained from (III.13) and (III.15) as shown in Appendix III.

Figure 3.2.3 shows the simulated spring characteristics of a cantilever beam made of polyethylene terephthalate (PET), 0.2 mm long, 2mm wide and 8 μm thick. The Young's modulus was set at 540 MPa. As can be seen in Figure 3.2.3, the cantilever beam becomes stiffer against a tensile force as the displacement increases, which indicates that the hinge parts of an LSEA has proper spring characteristics as previously explained.

3.2.2 Stroke Length

The stroke length can be easily increased by stacking many electrode films as shown in Figure 3.2.4. The top and bottom electrode films are fastened to the rigid clamping plates whereas the intermediate electrode films can be easily distorted because only the neighboring electrode films constrain them. Therefore, the deformation amount at the intermediate layer is larger than that at the top and bottom layer. The elongated LSEA has a shape constricted in the transverse direction in the middle. For a sufficiently multiply-layered LSEA, the stroke length is approximately proportionate to the number of layers.

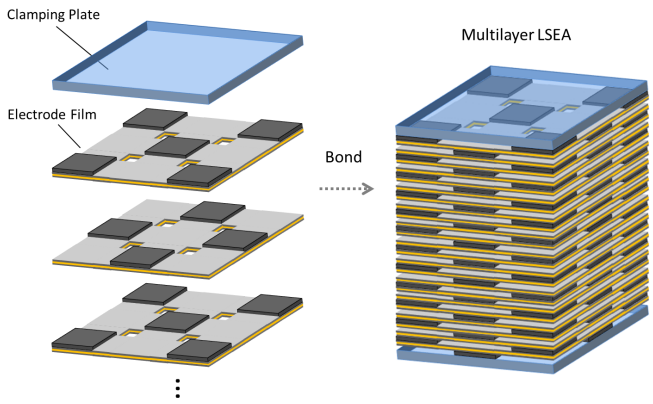

Figure 3.2.4: Longer LSEA stroke can be achieved by multi-stacking.

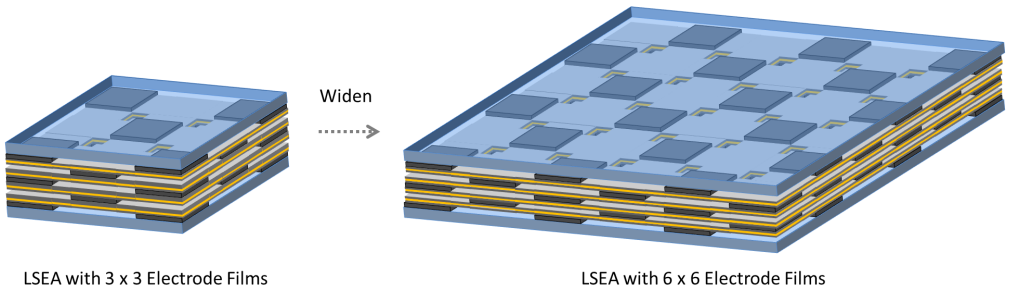

Figure 3.2.5: Large LSEA electrode area can be achieved using n×n electrode films.

3.2.3 Generative Force

The electrostatic force can be increased by increasing the electrode area S. This can be done by increasing the number of electrodes as shown in Figure 3.2.5. Specifically, only large-area electrode films are required for the fabrication of large LSEAs, which simplifies the fabrication process. Shortening of the hinge length is another way of increasing the electrostatic force because the gap d depends on the hinge length (see the cross-sectional view in Figure 3.1.1(c)). It should be noted that shortening of the hinge length decreases only the gap d in Equation (3.1), meaning that it can also be used to increase the area density of the generated force.

3.2.4 Fabrication Process

An LSEA can be made easily simply by stacking and bonding large-area electrode films. The electrode films comprised three-layered (insulator - conductor - insulator) films are commercially available from film processing manufacturers. Here the fabrication process of going from an electrode roll film to an LSEA is shown in the case where a polymer film and etchable metal foil are used as the insulator and the conductor respectively.

The fabrication process can be divided into the following three processes: (A) cutting of the electrode roll film, (B) etching of edge faces and (C) stacking and bonding the electrode films with an adhesive.

(A) Cutting

The electrode roll film is chopped into small pieces and cut them to form the shape of the electrode films. Laser ablation is useful to cut out the electrode films due to a low calorific cutting method. The method is also helpful to process films finely like making quadrilateral holes.

(B) Etching

The bare metal exposed in the side of the electrode films is etched to eliminate a risk of the atmospheric discharge. The etching process is also effective to eliminate the bare metal at pinholes which are defects of the electrode films. If the binder between the insulating film and conductive material can melt, thermocompression bonding can infill the minute air gap between the insulating films after etching.

(C) Stacking

The electrode films are stacked with an adhesive in a checkered pattern as shown in Figure 3.1.1(a). Care should be taken not to misalign the electrode films in the transverse direction by using jigs or manipulators. Printing technology is available when the adhesive is applied.

3.2.5 Other Characteristics

Lightweight

An LSEA consists of an insulator such as a polymer which have a density of about 1 g/cm^3 and a very thin conductive material. Because the most volume of an LSEA is occupied by the insulating films, an LSEA is lightweight even if the conductive material is a metal. The LSEA becomes more light by using conductive polymer or conductive carbon materials as the conductive material.

No friction loss

An LSEA does not lose the driving force by its friction because the contraction force and the external tensile force works perpendicularly to the electrode parts.

Energy saving

The energy loss is low due to the voltage driving when an LSEA holds loads in a same position. An LSEA has the same structure as a parallel capacitor electrically. It stores charges in the very short term in the beginning of the application of a voltage, and after that, very small steady current flows in the insulating films. The steady current I_s can be estimated as follows:

$$I_s \sim \frac{V}{\sigma}\frac{S_{\mathrm{tot}}}{t}, \tag{3.2}$$

where, σ [$\Omega \cdot$ m] is the volume resistivity, S_{tot} [m^2] is the product of the area of the conducting substance per electrode film and the number of electrode films, and t [m] is the thickness of the solid insulator per layer. Mostly the steady current will be lower than I_s because as LSEA has the other insulator between the conductive materials such as the adhesive, the insulating fluid and a binder between the insulating film and the conductive material.

Configuration

LSEAs can work as long as the electrode parts are connected to each other by the hinge parts. Although the electrodes are arranged in an n×n format in the previous figures in this paper, electrode parts can be arranged otherwise, e.g. a

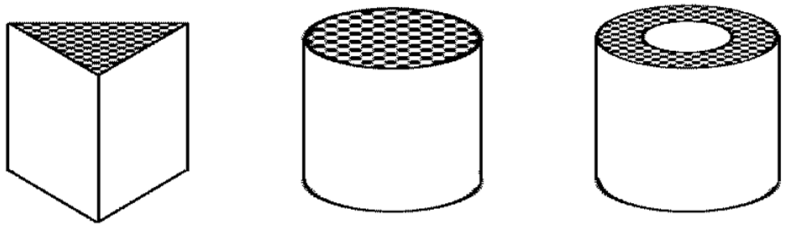

Figure 3.2.6: An example of realizable configurations. These LSEAs can be made by stacking triangular, circular and annulus-shape electrode films starting from the left figure. The checkered pattern on the top electrode films shows their adhesive pattern.

triangular pole type LSEA, round pillar type, cylinder type, etc. can be produced as shown in Figure 3.2.6.

3.3 Concluding Remarks

An LSEA is a multi-layered electrostatic actuator, contracting linearly by the application of a voltage. It is lightweight because it consists of flexible three-layered (insulator - conductor - insulator) films which have a specific gravity of about one. The stroke length can be increased by stacking a lot of electrode films and the force density can be increased by shortening the hinge length which is equivalent to narrowing the gap between the electrode films. Therefore an LSEA can achieve a high output at a small size. Changing the area and the configuration of the electrode films makes it possible to fabricate large-area LSEAs having different shapes. It indicates that an LSEA can achieve an output as high or higher than that of biological muscles even at a large scale, also having high power-weight ratio. An LSEA is, therefore, a strong candidate for an artificial muscle.

4

Prototypes

In this chapter, two prototypes are shown. One of them is a five-layered LSEA for measuring the spring characteristics, and the other one is a fifty-layered LSEA for measuring the contraction property, the generative force and so on. Both LSEAs have 16×16 electrode parts a layer. We also demonstrate the actually-used electrode film and the concrete fabrication process. Especially, we expatiate on the improvement method of adhesivity between the electrode films and the adhesive which is important for the LSEA to achieve proper spring characteristics.

4.1 Electrode Film

A commercial three-ply film (manufactured by Tokyo Film Kako Inc., Japan) was chosen as an electrode film to fabricate prototype actuators. Polyethylene terephthalate (PET) is used as the material of the top and bottom layer of the film. As the conductive layer, copper are evaporated on one PET film and covered by another PET film. To improve the adhesivity between PET film and Cu, a binder is used i.e. the film is five-ply, PET-binder-Cu-binder-PET, film in a precise sense

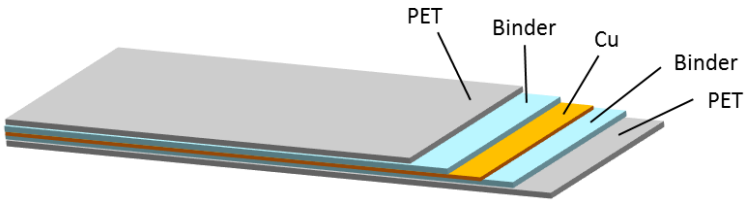

Figure 4.1.1: Schematic of the electrode film.

as shown in Figure 4.1.1. The thickness of PET film is 1.5 μm on one side and the thickness of copper layer is 0.3 μm. The whole thickness of the film was 8.6 μm determined by measuring the thickness of a stack of 20 flims using a micrometer gauge which is accurate to $\pm$0.5 μm. Therefore the thickness of the binder is estimated to be 2.7 μm for each.

4.2 Fabrication Process

4.2.1 Cutting

The electrode films were cut by laser ablation using MATRIX355-1-60 manufactured by Coherent, Inc (see Figure 4.1.2). The wavelength of the laser is 355 nm. The intensity, the repetition rate of the laser and moving speed of sample stage were 300 mW, 30 kHz and 1 mm/s respectively. The right picture in Figure 4.2.1 is an electrode film for 16$\times$16 format after cutting. The quadrilateral holes of

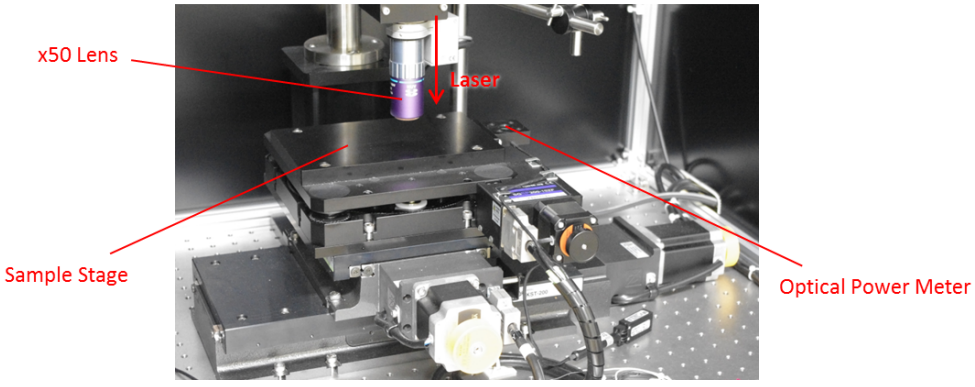

Figure 4.1.2: Laser ablation system.

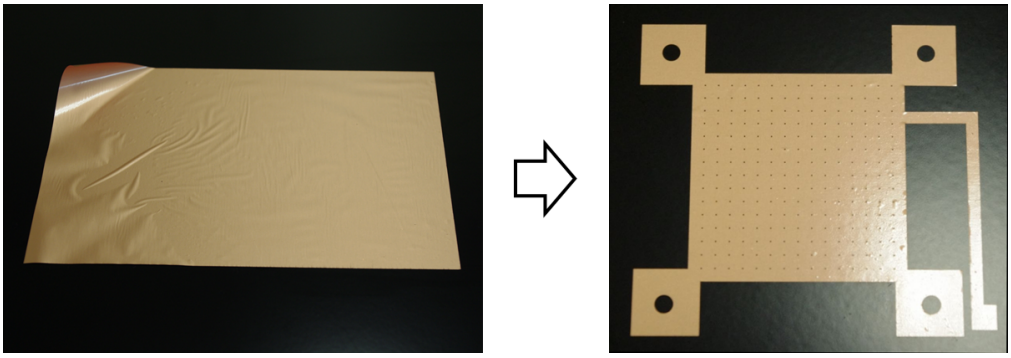

Figure 4.2.1: Pristine electrode film (left) and the electrode film after cutting (right).

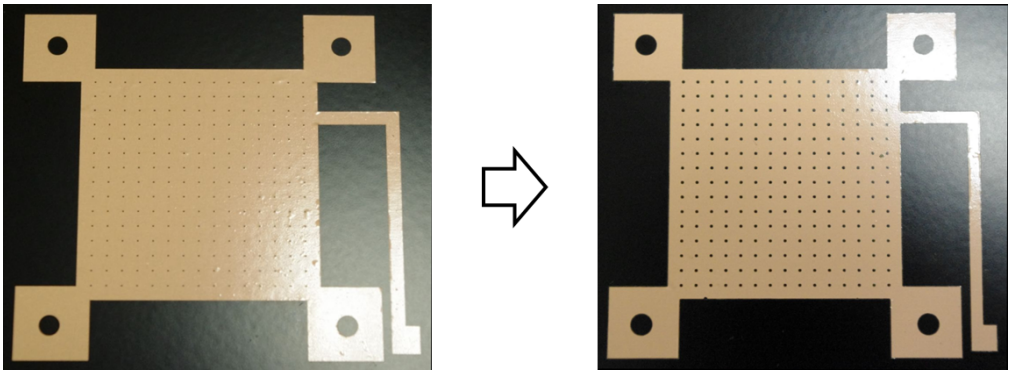

Figure 4.2.2: Cut electrode film (left) and etched film (right).

the area of 0.2 mm × 0.2 mm were cut 2 mm apart. The squares at the corners were cut out for use in position adjustment. The spindly part on the right of the electrode was left to connect with an electric power supply.

4.2.2 Etching

The bare copper on the edge faces was etched at 50 degrees C for 4 hours using saturated aqueous solution of Iron(III) chloride ($FeCl_3$ aq.) to prevent atmospheric discharge. The etching process eliminated the bare copper of about 100 μm from the edge (see Figure 4.2.2). After etching, warpage of the electrode films was corrected by thermocompression at 100 degree C for 30 minutes. The process does not infill the minute air gap between the PET films in this instance because the binder seems not to melt at the temperature.

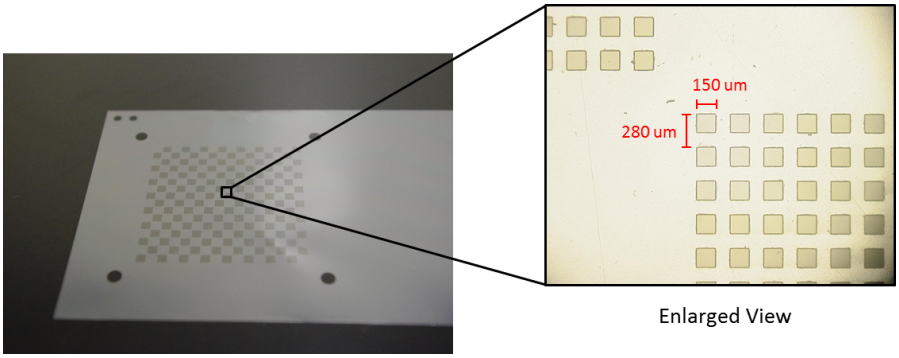

Figure 4.2.3: Mask for adhesive printing.

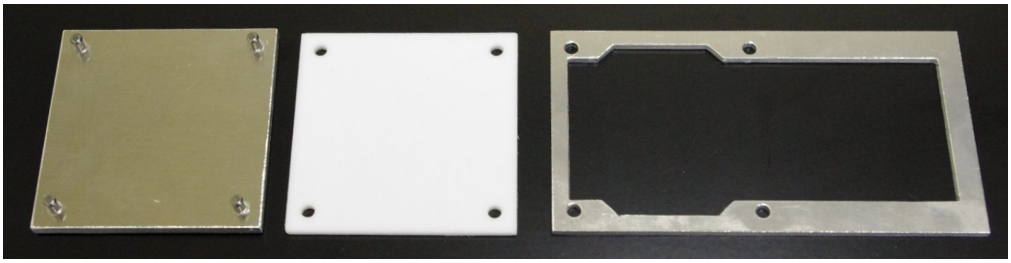

Figure 4.2.4: Jigs and stamp for adhesive printing. The left one is a flat plate to precisely allocate a stamp and a mask. The middle one is a mask made by teflon. The right one is a cover plate to fix a mask.

4.2.3 Stacking

The etched electrode films are stacked on a clamping plate using a flat plate which has four knock pins to precisely allocate the electrode films. Applying an adhesive was performed by an application of screen printing with masks and a stamp. The masks are polyethylene naphthalate (PEN) films of 12 μm thickness having a lot of small holes as shown in Figure 4.2.3. The small holes of the size of 150 μm $\times$ 150 μm were cut by laser ablation at 280-μm intervals to pass the adhesive. The simplest method is thought to apply the adhesive directly to the electrode films, but actually, the method involves the risk of tearing the electrode films due to strong adhesivity when the mask is eliminated. Therefore the adhesive pattern was transcribed once into a teflon stamp which is difficult to be bonded by adhesives, and next, the stamp transcribed the pattern into the electrode films. The adhesive was able to be transferred clearly in this method.

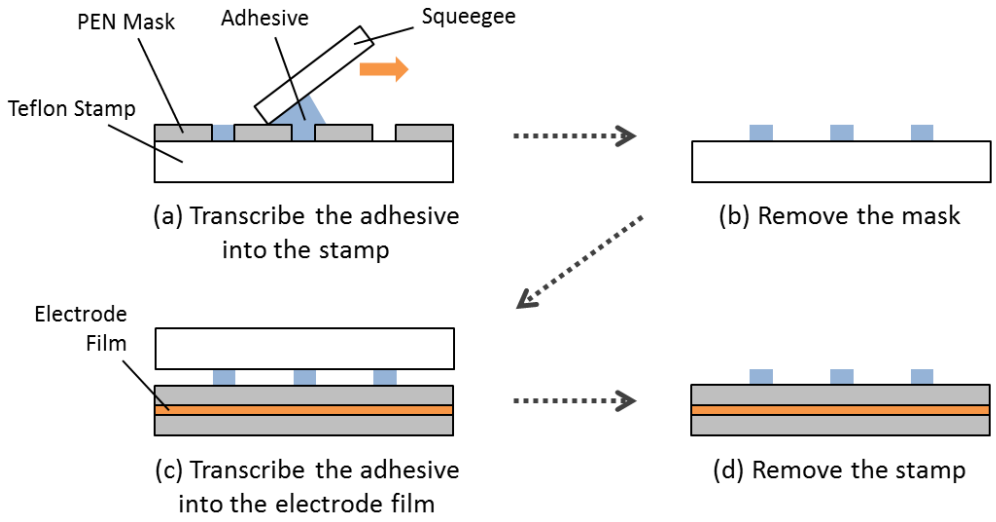

Figure 4.2.5: Schematic of the printing process of the adhesive with masks and a stamp.

Figure 4.2.4 shows jigs and a teflon stamp used for screen printing of the adhesive. Figure 4.2.5 shows schematic of the printing process with masks and a stamp. The concrete stacking process is as follows.

- Electrode films and the jigs are prepared (see Figure 4.2.6 (a)).
- The PEN mask film is overlapped on the teflon plate as shown in Figure 4.2.6 (b) by using jigs in Figure 4.2.4.
- The adhesive is transcribed on the teflon plate through the small holes at the mask using a squeegee.
- The mask is peeled off from the teflon plate. The adhesive remains on the teflon plate.
- The teflon plate is put on the stacked electrode films (Figure 4.2.6 (c)) .
- The teflon plate is peeled off from the electrode films. The adhesive is transcribed into the electrode film. Note that the checkered pattern of the adhesive should be alternate.
- The new electrode film is stacked and pressed with an even pressure of about 1.5 N/cm^2 for 5 minutes.

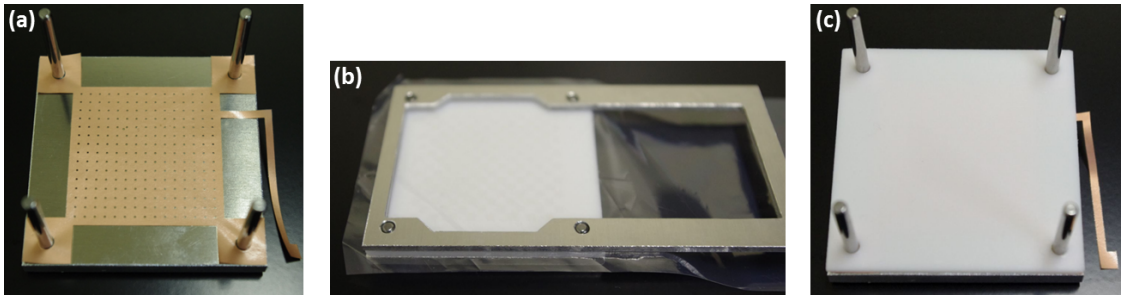

Figure 4.2.6: (a) Electrode film allocated by the knock pins. (b) Appearance of transcription of the adhesive into the teflon plate with the mask. (c) Appearance of transcription of the adhesive into the electrode film.

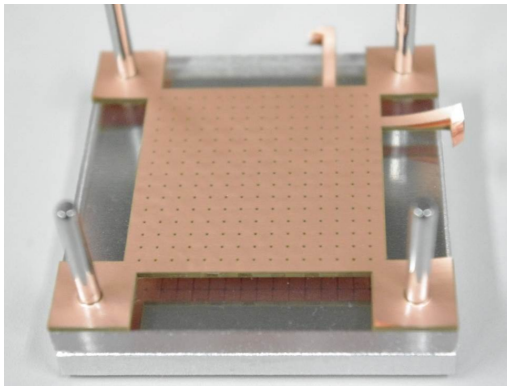

Figure 4.2.7: The stacked electrode films.

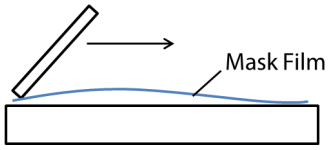

Figure 4.2.8: Schematic showing the position misalignment of the mask.

A silylated urethane adhesive was used to bond the electrode films. The time of the pressure bonding (5 minutes) was determined from the cure time. When bonding the clamping plate and the electrode film, we applied the adhesive on the whole electrode parts in order not to peel off the electrode film from the clamping plate.

The appearance of the stacked electrode films are shown in Figure 4.2.7. In this method, the mask film was shifted 60 μm by a force generated during transcription of the adhesive on the teflon plate using the squeegee as shown in Figure 4.2.8. The misalignment is therefore offset by using masks whose holes are displaced 60 μm in advance. The printed adhesive pattern is shown in Figure 4.2.9. The picture was taken by pressing a printed electrode film to a flat glass plate. The adhesive expanded to a diameter of about 300 μm. As is clear from this picture, the adhesive

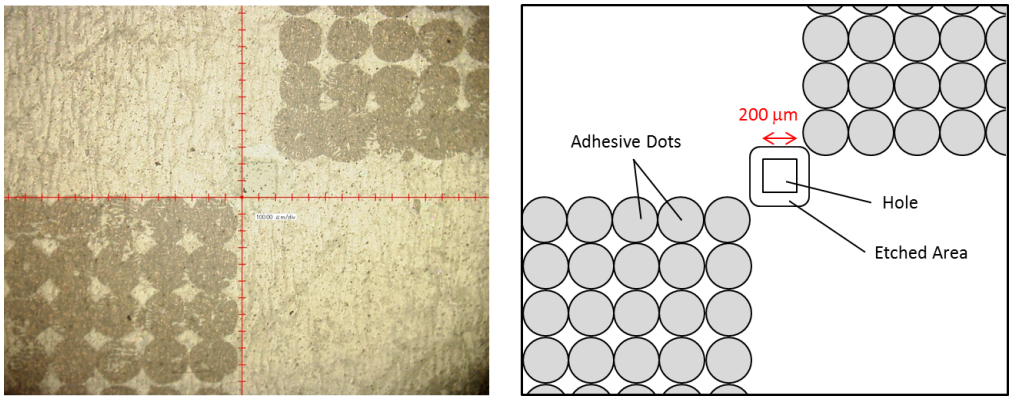

Figure 4.2.9: The printed adhesive pattern and quadrilateral hole (left) and its schematic (right).

was applied in the appropriate areas.

4.3 Adhesion Improvement

PET provides excellent electrical insulation, mechanical strength, workability, safety and cost-effectiveness, being suitable as an insulator film of an LSEA. However, it is one of the difficult materials to bond by an adhesive even though the LSEA requires high adhesivity between the electrode films to achieve the proper spring characteristics. In this section, improvement methods of the adhesivity are presented. We treated the electrode films and the clamping plates with ultrasonic cleaning and UV-ozone process before the stacking process.

4.3.1 Ultrasonic Cleaning process

Ultrasonic cleaning is effective to remove fine dusts and contamination from the surface of PET films. By processing in ethanol, fats and oils attached to the surface of PET films can be removed effectively. In the fabrication process of prototypes, the electrode films and the clamping plates were placed inside an ultrasonic bath filled with ethanol for 5 minutes.

4.3.2 Surface Modification

The adhesivity of plastics is increased by modifying the surface. The surface modification is expected to the following advantages.

Anchor Effect This is affected by surface roughness. Adhesion force is increased by penetration of an adhesive into microasperity or minute grooves on materials. The adhesive behaves like an anchor or a fastener. Corona treatment and plasma processing are effective to roughen the surface of materials. Plasma processing makes nanoscopic asperity.

Chemical Modification Adhesives and adherends have their specific surface tension. When an adhesive and a material have a same surface tension and the boundary tension is zero, the adhesion force reaches the maximum value. Substituting the hydrophobic groups with hydrophilic groups on the surface of materials is generally effective to reduce the boundary tension between various adhesives and the materials. The change can be confirmed by measuring the wettability of the surface of the materials. The modification can be done by UV-ozone processing and plasma processing.

4.3.3 UV-ozone Processing

Principle

UV-ozone processing cleans and chemically modifies the surface of plastic materials using UV and ozone. The cleaning effect also increases the adhesivity between the materials and adhesives secondarily. The processing uses a low-pressure mercury lamp emitting ultraviolet rays of the wavelengths of 254 nm and 185 nm. The UV breaks chemical bondings such as C-H bonds on the surface of the materials (see Figure 4.3.1). On the other hand, UV 185 nm splits oxygen (O_2). The resulting oxygens in the ground state ($O(^3P)$) attach to the other oxygen molecules, forming ozone (O_3). UV 254 nm splits ozone into oxygen molecules and excited oxygen atom ($O(^1D)$). The resulting excited oxygen is added to the surface of the materials, which makes hydrophilic groups such as hydroxy groups ($-OH$) as shown in Figure 4.3.1.

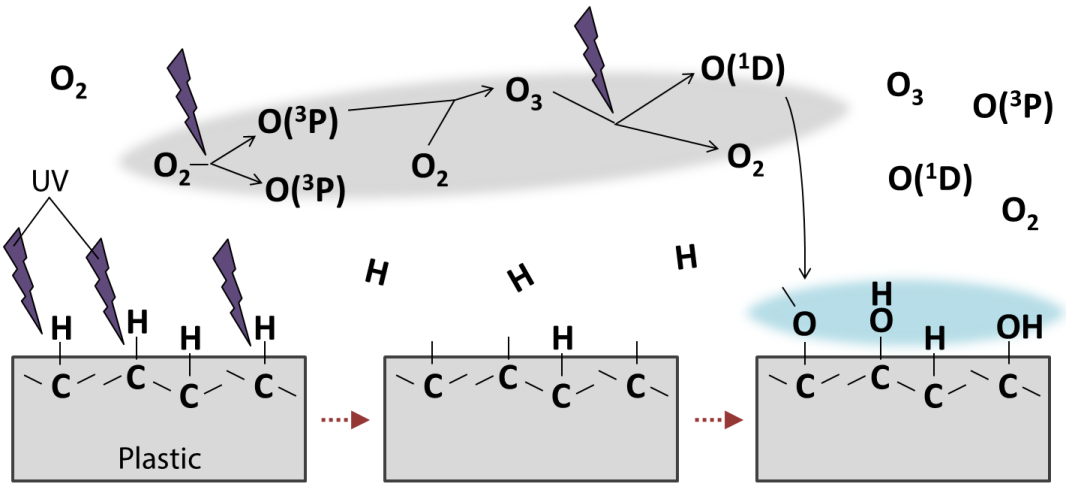

Figure 4.3.1: Schematic of UV-ozone processing.

Experiment

In order to investigate the effect of UV-ozone processing, we measured change of the wettability of a PET film and the adhesion force between electrode films and an adhesive. The UV-ozone processing was carried out using a UV ozone cleaner (UV253E, Filgen, Inc.). The wettability can be investigated by measuring the angle of contact of a water droplet. According to a half-angle method, we can assume that the shape of the fine water droplets is a part of a circle, and calculate the contact angle θ using the equation expressed as follows:

$$\theta = 2\tan^{-1}\frac{h}{r} \tag{4.1}$$

where, h represents the height from the PET surface to the top of the droplet and r represents the radius of the droplet at the contract surface. Figure 4.3.2 shows change of the contact angle as a function of the UV exposure time. The flow rate of oxygen gas into the device was 0.5 L/min. The result indicates that the wettability of the PET surface is increased by UV-ozone processing and saturated with the exposure time of about 10 minutes.

The adhesivity was measured by T-peel test (see Figure 4.3.3). The T-peel test is one of the standard methods to investigate the adhesion force for flexible adherends. This test is suitable for an LSEA to evaluate the adhesivity of the

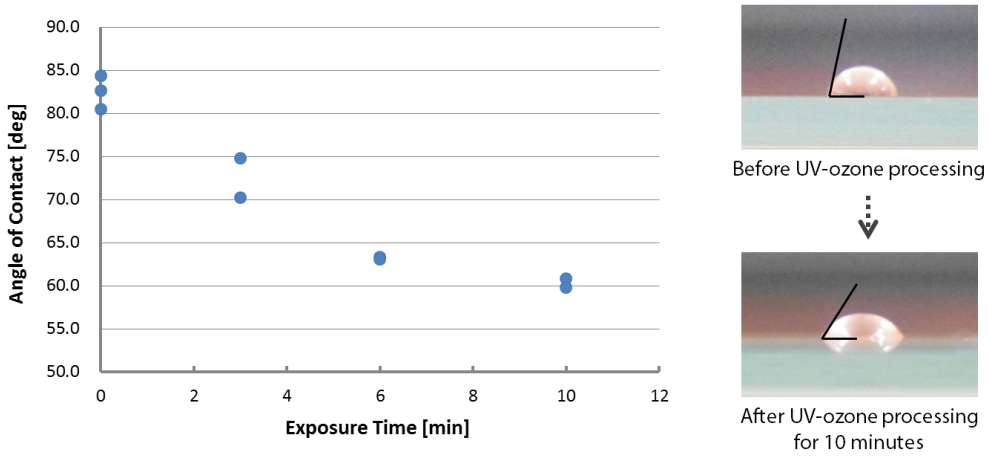

Figure 4.3.2: Change of the wettability of a PET film.

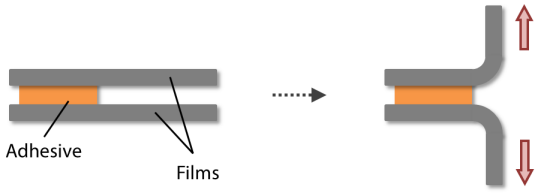

Figure 4.3.3: Schematic of peeling test.

electrode films because it recreates the force acting on the adhesive between the electrode films. We measured the time course of the adhesion force of bonded electrode films. A couple of different bonded electrode films were compared, i.e. that made by electrode films treated only with ultrasonic cleaning and treated with ultrasonic cleaning plus UV-ozone for 5 minutes. Figure 4.3.4 shows the appearance of the bonded electrode films in the T-peel test and Figure 4.3.5 shows change of the adhesion force as a function of elapsed time. Both samples lost the adhesivity shortly after peeling. However the holdable load differs greatly between the pristine electrode films and the ones processed by UV-ozone. The processed electrode films achieve the adhesion force of 195 mN after a day of testing, though the bonded pristine electrode films hold the adhesion force of a mere 23.5 mN. As shown in the graph, the processed films also kept its adhesivity after that.

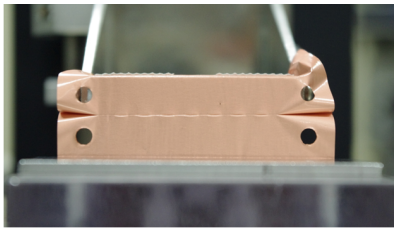

Figure 4.3.4: Electrode film during T-peel test.

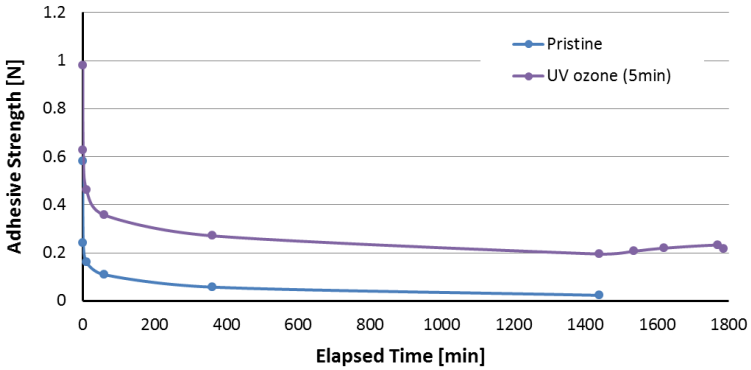

Figure 4.3.5: Change of the adhesion force between the adhesive and the electrode films with and without UV-ozone processing with respect to time.

4.4 Prototypes

In this study, we fabricated two prototypes (prototypes A and B) of the LSEA to determine their spring characteristics and other performances such as the generated force, the stroke, the responsiveness and the energy consumption. Prototype A was a short-stroke actuator made to examine the performance of its hinge parts. In contrast, Prototype B was a long-stroke actuator made to investigate various performances of an LSEA.

4.4.1 Prototype A

To confirm that the hinge parts prevent the overextension of the electrode intervals, Prototype A was fabricated as shown in Figure 4.4.1. The prototype was a 16×16 LSEA with five layers. Totally 12 electrode films were used to make the prototype because two electrode films make a gap between the electrode parts, i.e. 10 electrode films need to make a five-layered LSEA, and rest of the two electrode films fixed to the clamping plates fully. It had square electrodes of area 4 mm^2 and

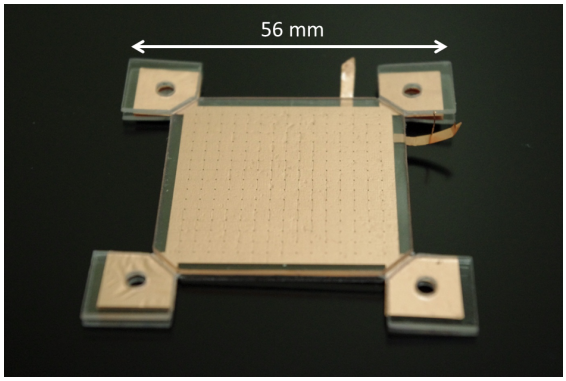

Figure 4.4.1: Prototype used for investigating the spring characteristics (Prototype A).

200 μm long hinge parts. The prototype was not etched the bare copper on the edge faces and was also not treated with UV-ozone processing. The clamping plates were PET plates of 1 mm thick. To connect it to external devices, double-stick tapes were used.

4.4.2 Prototype B

Prototype B had 50 layers, which is 10 times that of Prototype A and is used 102 electrode films. All of the electrode films and the clamping plates were etched the bare copper on the edge faces and treated with UV-ozone processing for 5 minutes. The configuration and dimensions of the electrode films were same as Prototype A. The clamping plates were PET plates of 2 mm and 5 mm thick. Both clamping plates had screw holes to connect external devices. Copper wires were attached to the electrode films by a conductive silver paste to enable the supply of voltage (see Figure 4.4.2).

Moreover, four external stoppers were used to protect the LSEA from a large external tensile force. The stoppers (plastic poles jointed to plastic disks) were attached by using a jig whose projecting metal plates inserted between the clamping plates kept the stretch length of Prototype B constant as shown in Figure 4.4.3. The stoppers restricted the movement of the LSEA to between 0 and about 1 mm from the completely contracted state. Table 4.4.1 lists properties of Prototypes A and B for comparison.

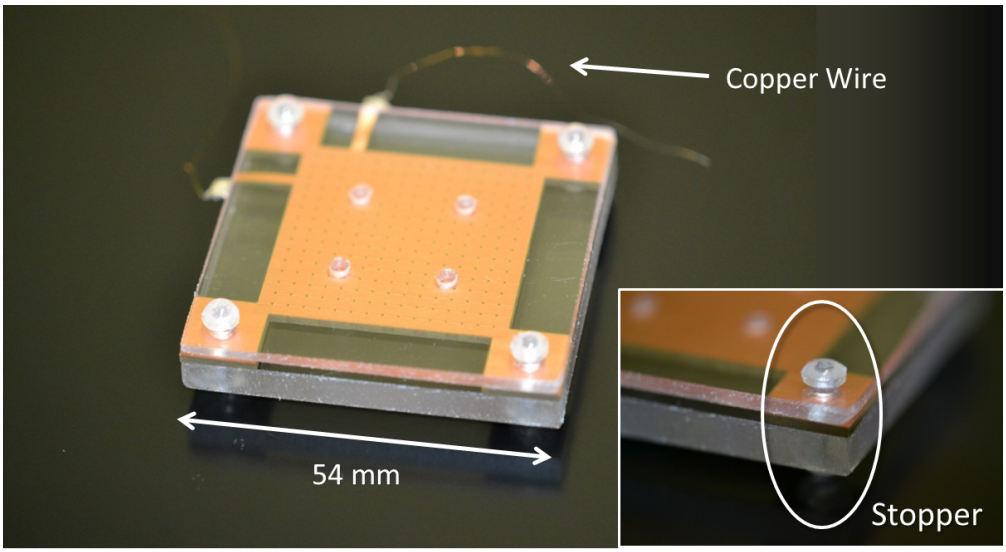

Figure 4.4.2: 50-layer LSEA with external stoppers (Prototype B).

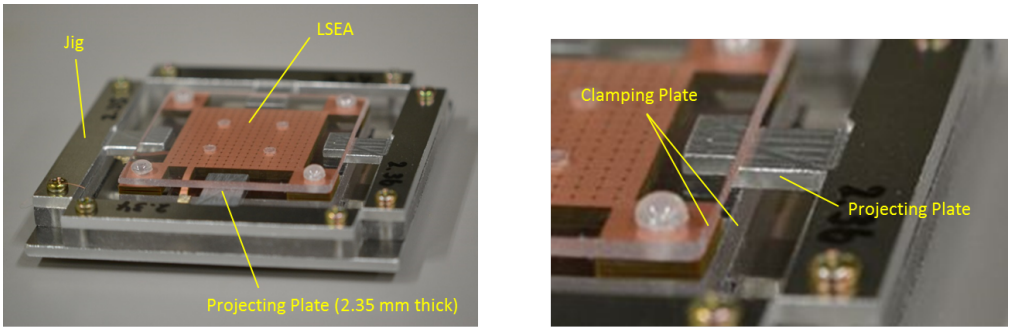

Figure 4.4.3: Jig for attachment of the external stoppers and Prototype B (left) and its enlarge view (right).

Table 4.4.1: Key data[a] of the prototypes.

Prototype	N_{elec}	N_{layer}	S_{elec}	L_{hinge}	S	M_{LSEA}
A	16×16	5	4 mm^2	200 μm	12.6 cm^2	0.28 g
B	16×16	50	4 mm^2	200 μm	12.6 cm^2	2.4 g

[a] N_{elec}, N_{layer}, S_{elec}, L_{hinge}, and S respectively denote the number of electrodes, number of layers, area of an electrode, hinge length, and area of the conducting substance per electrode film. M_{LSEA} denotes the mass of the LSEA without the clamping plates.

4.5 Concluding Remarks

In this chapter, the fabrication process and the prototypes of LSEAs were presented. The easy fabrication process is one of the advantages of LSEAs, i.e. only making laminated films (also commercially available) and cutting, etching and stacking them. Ultrasonic cleaning processing and UV-ozone processing were effective to improve the adhesion force at boundary face between adhesives and plastic films.

5

Spring Characteristics

This chapter presents measured spring characteristics of prototypes A and B in detail. The spring characteristics is the most important factor determining the performance such as the generated force, the contraction property, the responsiveness. The spring characteristics was measured in atmospheric pressure and vacuum to investigate the effect of an external pressure and the effect of an air drag. The measurement of each spring characteristics was carried out from the perspective of the following.

Prototype A to examine the spring characteristics of the hinge parts.

Prototype B to estimate the effect of the degree of vacuum.

5.1 Measuring Instrument

Measuring the elongation as a function of the force acting on a prototype is important because the gaps between the electrodes settle the elastic force of the hinge parts and the electrostatic force according to (3.1). This section presents

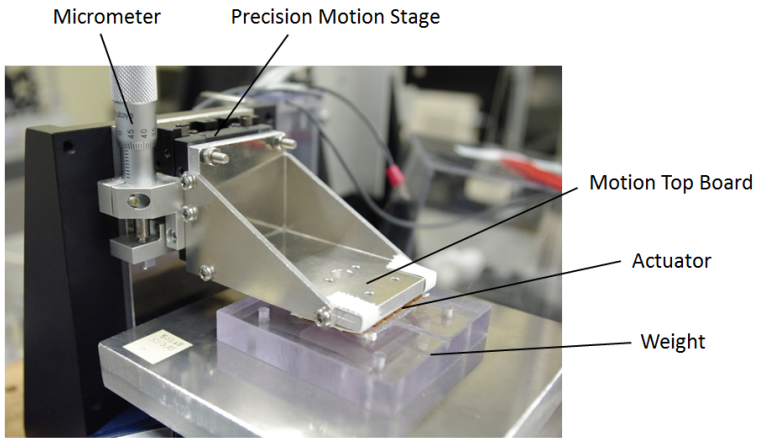

Figure 5.1.1: Appearance of the F-d measuring instrument for Prototype A.

instruments measuring elongation and force simultaneously for each prototype. In addition, setup for measurement in vacuum is shown.

5.1.1 F-d Measuring Instrument for Prototype A

Appearance of the F-d measuring instrument for Prototype A is shown in Figure 5.1.1. The prototype was fixed to a movable top board and a load with double-stick tapes. The movable top board was fixed to a precision motion stage so that the travel distance could be set by the micrometer manually, changing the elongation of the prototype. The load was placed on a electric balance which displayed 100 mg in a unit. Therefore, the elongation of the prototype and the force acting on the weight can be measured simultaneously. The natural length of Prototype A was defined as the unloaded length. The extra displacement caused by movement of the electric balance and deformation of the adhesive tapes was taken into account for investigation of the displacement of the prototype.

5.1.2 F-d Measuring Instrument for Prototype B

Figure 5.1.2 shows the F-d measuring instrument for Prototype B. The top clamping plate was fixed to the movable board connected with the motorized stage, and the bottom clamping plate was fixed to the quartz force sensor (Type 9207, Kistler Instruments AG of Switzerland). The prototype was contracted and elongated using the motorized stage, which enables to measure the displacement and the force

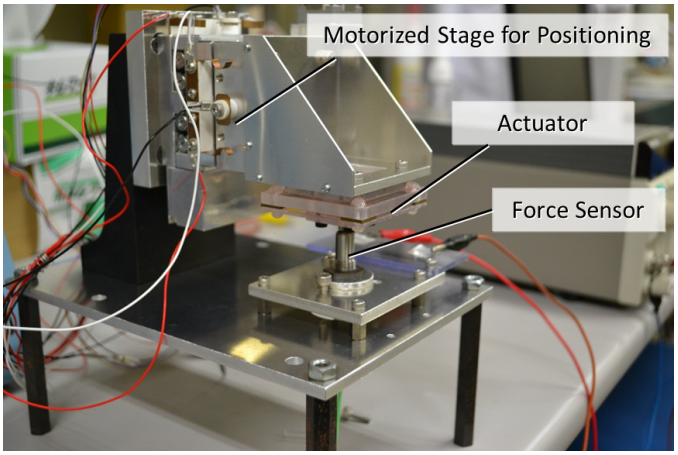

Figure 5.1.2: Appearance of the F-d measuring instrument for Prototype B.

simultaneously as well as the case of Prototype A. The travel distance and travel speed of the stage were controlled by a PC. The elongated length of the prototype was measured using a digital camera with a resolution of 1920×1080 pixels and frame rate of 23 fps.

The force sensor was highly sensitive and capable of measuring less than 1 mN, which enabled the measurement of minute differences in the force acting on the prototype. However it was able to measure only the relative value against the force at the start time of measurement, which required to measure the actual force at a measuring point separately.

5.1.3 Vacuum Vessel

The performance of Prototype B was also examined in vacuum. Figures 5.1.3 and 5.1.4 show the setup for measurement in vacuum and appearance of the vacuum vessel, respectively. This vessel was able to achieve high vacuum less than 5.0×10^{-6} Torr. The terminals for high-voltage source and the digital camera were installed at the vacuum vessel, enabling the same measurement in vacuum as in atmospheric pressure. The strokes of the prototype could be also measured by attaching a load to the bottom clamping plate instead of the force sensor, as shown in Figure 5.1.3. The degree of vacuum was determined by using a convectron gauge of the range from 1000 Torr to 0 Torr. The measurement was carried out in atmospheric

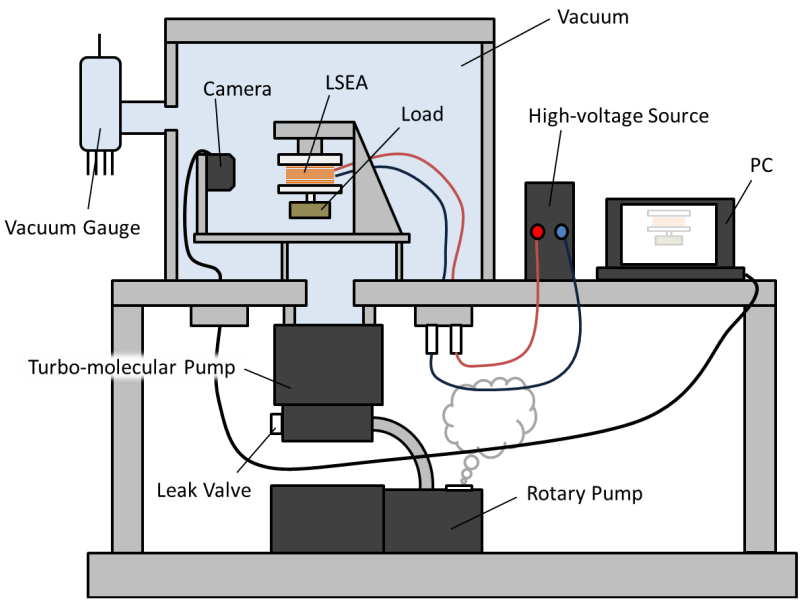

Figure 5.1.3: Schematic of the setup for measurement in vacuum.

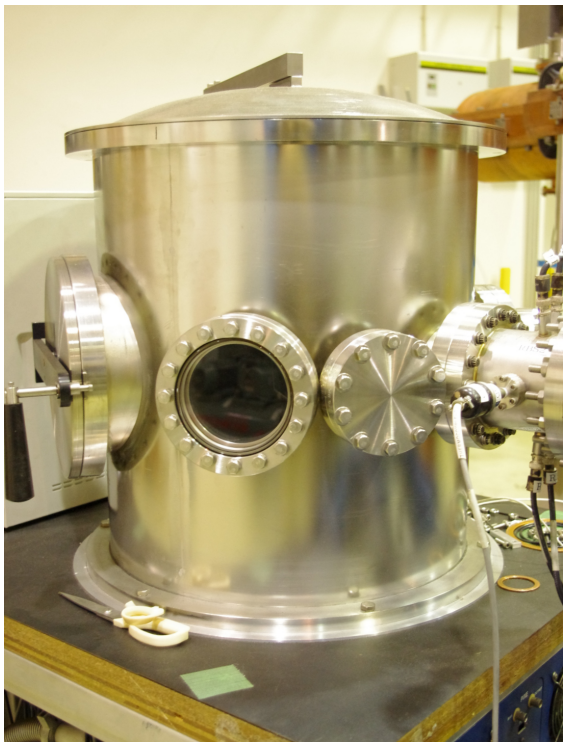

Figure 5.1.4: Appearance of the vacuum vessel.

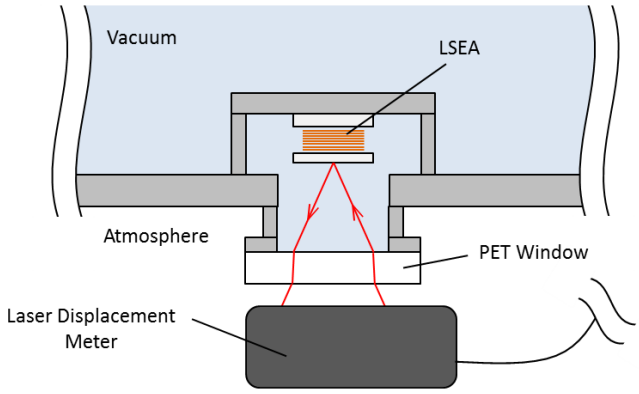

Figure 5.1.5: Schematic of the displacement measurement by the laser displacement meter.

pressure, 0.8 atm, 0.6 atm, 0.4 atm, 0.2 atm and high vacuum ($< 5.0 \times 10^{-6}$ Torr). Every degree of vacuum does not be included in glow discharge zone.

Laser displacement meter

In order to determine the slight change of the natural length of the prototype in vacuum, a laser displacement meter (LK-G85, KEYENCE Co Ltd, Japan) was used, being accurate to ± 0.2 μm. We determined the displacement of the prototype by measuement of the regular reflection light as pictured in Figure 5.1.5. Deformation of a PET window on the vessel was corrected for investigation of the displacement of the prototype in vacuum.

5.2 Prototype A

Figure 5.2.1 shows the spring characteristics of Prototype A. The horizontal axis represents the elastic force, and the first vertical axis represents the average extension per layer, which was calculated by dividing the elongated length of the LSEA by the number of layers. The spring constant per layer was calculated from the slope by using least square. The average spring constant was 38 kN/m per layer in the 0–30 μm range, which is referred to as the soft range; and 138 kN/m per layer in the 75–150 μm range, which is referred to as the hard range. The spring constant in the hard range was 3.6 times that in the soft range. The non-linear spring characteristics show that the LSEA structure can prevent overextension of

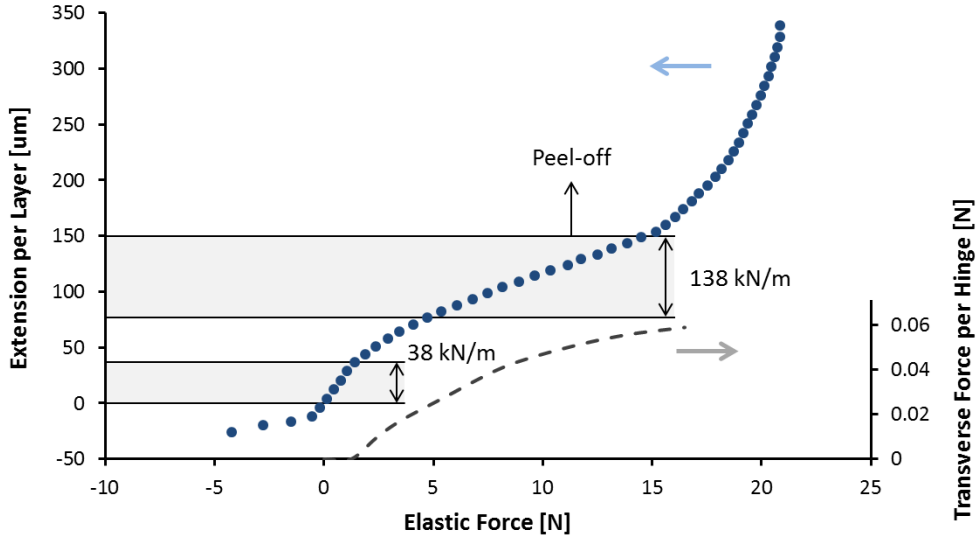

Figure 5.2.1: Spring characteristics of Prototype A.

the electrode intervals. However, the adhesive peeled off over 150 μm of the extension per layer. The observation indicates the necessity of treating with UV-ozone processing and attaching an external stopper to prevent the LSEA adhesive from being peeling off by an external force.

We must add that the prototype was pulled once by a force of 5 N before the measurement, and peeling part of the adhesive might occur, making the hinge lengths longer. According to the simulation of a cantilever beam, the hinge length should have been 290 um (90 um longer than the desired value) to match the calculated value to the measured extension of the prototype. In the simulation, we assumed that the thickness of the PET films, the binder and the copper were 3.0 μm, 5.3 μm and 0.3 μm, and their Young's moduli were 4.2 GPa, 9.8 MPa and 55 GPa respectively as developed later. The simulation also showed that the transverse force acting on the hinges (see Subsection 3.2.1) should increased as the prototype was elongated as shown in Figure 5.2.1. The force worked to prevent the prototype elongating. It is interesting to note that the transverse force appeared over the soft range. The force were calculated with the hinge length kept constant. The actual transverse force might have larger values than the calculated force because peeling off the adhesive seemed to progress over 5 N. Leastwise, the result indicates the spring characteristics of LSEAs come from a synergistic effect

between

(a) the geometric effect of the hinge parts as shown in Figure 3.2.3 and

(b) the effect of the transverse force preventing the prototype elongating.

The effect (b) recedes for the middle layer of multi-layered LSEAs, but it can be controlled by connecting short-length LSEAs and rigid plates alternatively in series.

5.3 Prototype B

The spring characteristics of the prototype were measured as a function of the degree of vacuum. Here, we first explain the procedure for determining the zero points of the displacement and the applied force of the prototype before showing the spring characteristics.

5.3.1 Relationship between the elongation of the prototype and the travel distance of the stage

We defined the elongated length per layer of Prototype B as to match the gap length between the electrode parts, i.e. the elongated length of 0 μm representes the completely contracted state (with no air gaps). In order to determine the thickness of the prototype at the completely contracted state, the relationship between the elongated length of the prototype and the travel distance of the stage was measured. Figure 5.3.1 shows the measuring results of the elongation of the prototype as a function of the travel distance of the movable stage in atmospheric pressure and a vacuum. Both results were similar to each other, having two following phases.

- **Completely contracted phase** – The thickness of the prototype showed little change although the stage moved. The slight displacement of the prototype indicated the deformation of the adhesive.
- **Deformation phase** – The travel distance of the movable stage roughly equaled to the elongation of the prototype. The displacement of the prototype mainly depended on the deformation of the hinge parts.

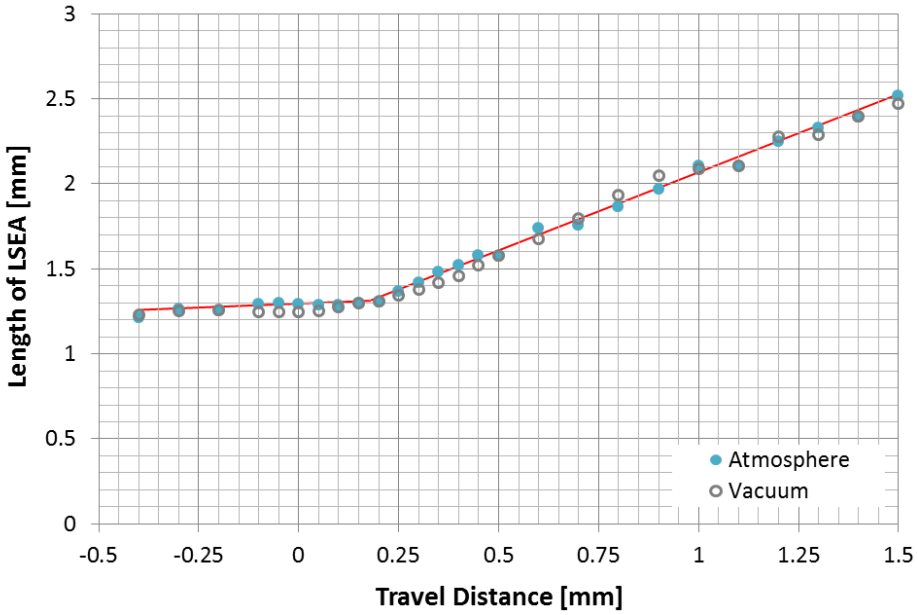

Figure 5.3.1: Relationship between the elongation of the prototype and the travel distance of the movable stage.

The measurement was carried out within the allowable range of load for the movable stage. The step motor in the stage, therefore, did not lose steps. The movement of the stage in completely contracted phase seem to make deformation of the quartz force sensor.

If the travel distance is defined as x and the elonagation of the prototype as y, their relationship is expressed as follows:

$$\begin{cases} y = 0.12x + 1.286 & \text{(completely contracted phase)} \\ y = 0.91x + 1.149 & \text{(deformation phase)} \end{cases} \tag{5.1}$$

From the cross point of the two lines, the thickness of Prototype B was determined as 1.31 mm, i.e. 0 μm elongated length per layer was defined as that when the prototype was 1.31 mm thick. We also obtained the thickness of the adhesive by subtracting total thickness of the electrode films from thickness of the completely contracted prototype. The thickness of the adhesive was 4.2 μm per sheet of the electrode films. Equation (5.1) was used as a compensation formula for the experiment below.

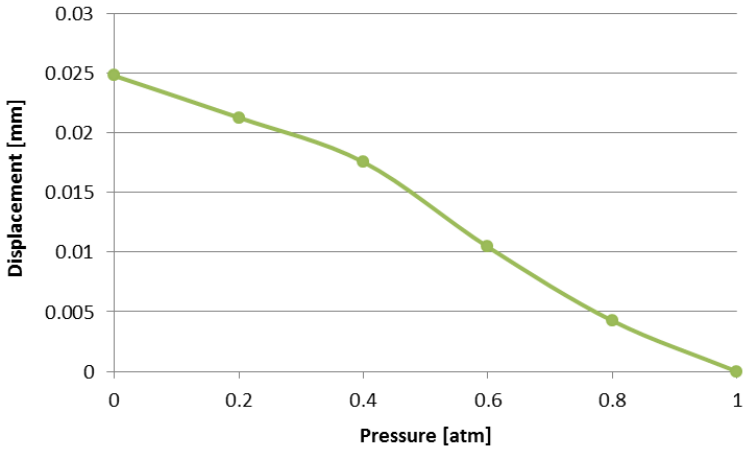

Figure 5.3.2: Change of the elongated length of the prototype with respect to the degree of vacuum. The length in atmospheric pressure was set as a standard (0 mm).

5.3.2 Relationship between the Elongation of the Prototype and a Load Weight

As described above, the quartz force sensor can measure only the relative value. In order to actual force acting on the prototype, we measured the thickness of the prototype connected the bottom clamping plates with a load instead of the force sensor in atmospheric pressure. This measurement showed that the thickness of the prototype was 1.74 mm when the load was 0.111 N. We can obtain the actual force value from the force sensor by shifting linearly the measured force value using the relationship.

In vacuum, the thickness of the prototype was expected to increase due to the expansion of the materials. We carried out the same experiment with changing the degree of vacuum. In the experiment, the relative change of the elongated length was measured by using the laser displacement meter. The length in atmospheric pressure was set as a standard. The result (Figure 5.3.2) shows that the elongated length of the prototype increased by 25 μm with increasing the degree of vacuum.

5.3.3 Spring Characteristics and the Degree of Vacuum

The spring characteristics of Prototype B are shown in Figure 5.3.3. Each spring characteristics measured for the third time in a row (the start and the end point

were set in the neighborhood of 0 N). The elongation and contraction speeds were unified at 50 μm/s. As you can see, all of the spring characteristics indicate hysteresis, having excellent repeatability. The spring characteristics comprised the three ranges described below:

- **Completely contracted range** – The prototype exhibited stiffness for the range between 0 and 5 μm.
- **Soft range** – The prototype was soft for the range between 5 and 20 μm.
- **Stopper range** – The prototype was stiff for the range above 20 μm because the clamping plates came into contact with the stoppers.

In the completely contracted range, the prototype was compressed by the external force and was in the completely contracted state. The spring constant was mainly as a result of the elasticity of the adhesive. It is to be noted that 5 μm approximately equaled to the thickness of the adhesive of 4.2 μm per sheet of the electrode films. In the soft range, the prototype was elongated by the external tensile force and was in the soft range described in Section 5.2. The spring constant ranged between 59 kN/m and 68 kN/m. This value was higher than the spring rate of Prototype A in the soft range, indicating that peel-off of the adhesive in Prototype B was less than that of Prototype A. The stopper range was similar to the hard range described in Section 5.2. However, whereas the stiffness of the LSEA in the stopper range was as a result of the action of the external stoppers, that in the hard range was due to the performance of the hinge parts regardless of the external stoppers. The mechanisms are therefore different. The LSEA is still in the soft range while in the stopper range. The stopper range is necessary to prevent the external tensile force from destroying the LSEA. The hard range is necessary to prevent the decrease of the electrostatic force that results from overextension of the electrode intervals in each layer.

The spring constants at the soft range differed as shown in Figure 5.3.4 though they were same seemingly. The graph shows the spring constants during elongation and contraction, and their average ('Overall' in the graph). The average spring constant gradually increased from 62.6 kN/m in atmospheric pressure to 65.5 kN/m in vacuum.

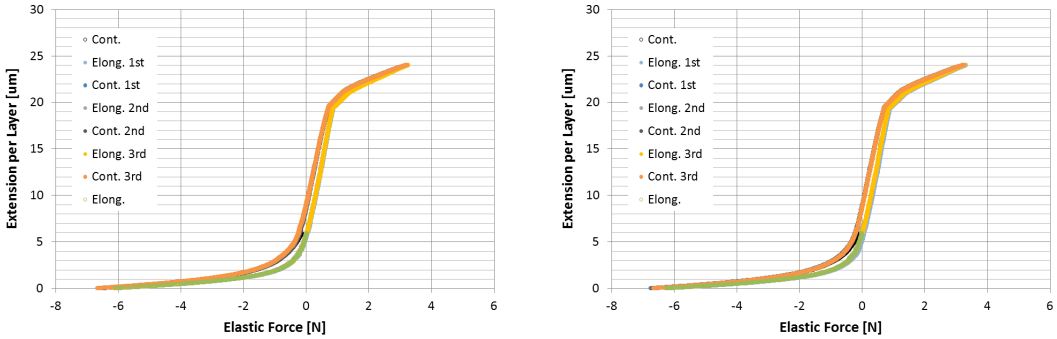

(a) Atmospheric Pressure **(b)** 0.8 atm

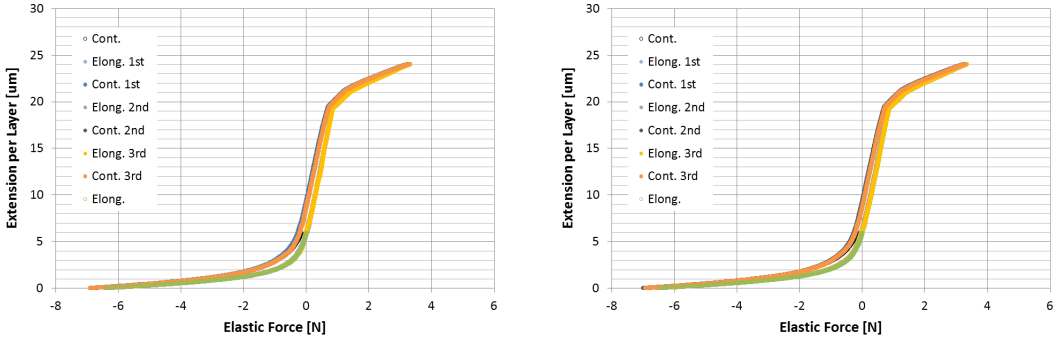

(c) 0.6 atm **(d)** 0.4 atm

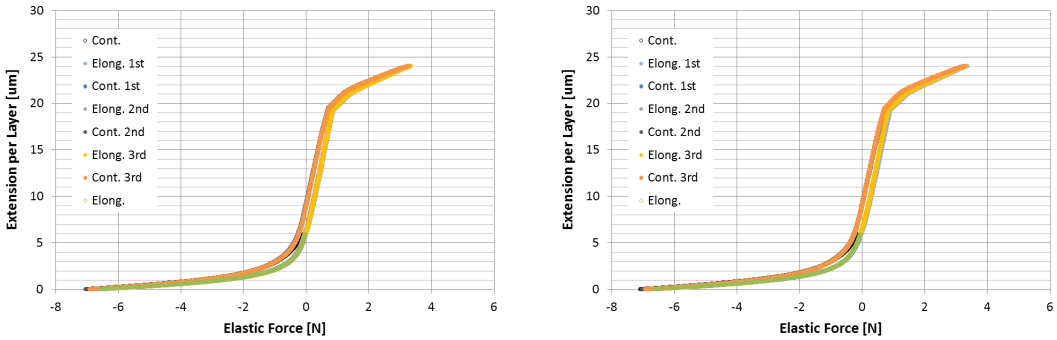

(e) 0.2 atm **(f)** Vacuum

Figure 5.3.3: Spring characteristics in the different degree of vacuum.

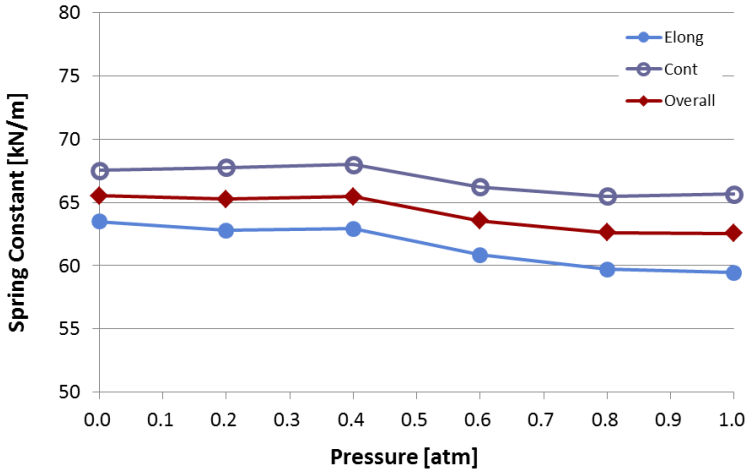

Figure 5.3.4: Change of the spring characteristics with respect to the degree of vacuum.

In order to explain the phenomenon, we estimate the expansion of the adhesive and the binder between the PET films using the result in Figure 5.3.2. First, we assumed that the elongation of the prototype at a vacuum was caused by the expansion of the adhesive and the binder. We can calculate the Young's modulus E [Pa] of a complex material consisting of n different materials connected in series in the longitudinal direction. When the Young's modulus and the thickness of Material i ($i = 1, 2, \cdots, n$) are E_i [Pa] and t_i [m] respectively, the Young's modulus of the complex material of $t = \sum_i t_i$ [m] thick is expressed as follows:

$$\frac{t}{E} = \sum_{i=1}^{n} \frac{t_i}{E_i} \quad \text{(Longitudinal direction)}, \tag{5.2}$$

$$Et = \sum_{i=1}^{n} E_i t_i \quad \text{(Transverse direction)}. \tag{5.3}$$

With the obtained thicknesses of the adhesive and the binder, the lower limit of the Young's modulus of the binder was calculated as 2.19 MPa by using Equation (5.2).

The Young's modulus of the binder led the beam length of 122.8 μm to obtain the spring constant in atmospheric pressure, 62.6 kN/m, where we seemed the half hinge as a cantilever beam consisting of PET(1.5 μm)-binder(5.3 μm)-PET(1.5 μm). As the Young's modulus of the PET film, 4.15 GPa was used (see Appendix IV). The result indicated that the hinge lengths of Prototype B were 245.6 μm

averagely. On the other hand, the thickness of the binder in vacuum should have been 5.477 μm/sheet (0.177 μm/sheet thicker than the thickness of the binder in atmospheric pressure) to match the rigidity of the beam to the spring constant of the prototype in vacuum, 65.5 kN/m. Here, we assumed the hinge lengths were constant. Using the same calculation, we calculated that the beam length was 136.3 μm and the expansion of the binder in vacuum was 0.146 μm/sheet thick, assuming that the upper limit of the Young's modulus of the binder was 4 GPa.

Second, the range of the Young's modulus of the binder was determined from 3.03 MPa to 3.67 MPa which achieved the calculated expansion of the binder from 0.146 μm/sheet to 0.177 μm/sheet. This result determined the Young's moduli of the adhesive and the copper in the prototype from the expansion relationship between the adhesive and the binder, the result of tensile test of a electrode film (see APPENDIX IV) and Equation (5.3). These Young's moduli were as follow:

- Binder: 3.35±0.32 MPa
- Adhesive: 5.33±1.00 MPa
- Copper: 56.3±35 GPa .

We simulated the hinge part as a cantilever beam with the Young's moduli of the binder and the copper described above, and obtained that the hinge length should have been 245.6 μm to recreate the spring constant in atmospheric pressure. The Young's modulus of the binder led 0.16 μm/sheet as the expansion of the binder (in the same manner, 84 nm/sheet was obtained as the expansion of the adhesive). This value was valid to recreate the spring constant in vacuum, showing 65.8 kN/m averagely. Therefore we found that the expansion of the binder induced increment of the spring constant of the prototype quantitatively.

In addition, the hinge length of 245.6 μm due to the misalignment of the electrode films, variability of the amount of the adhesive and peel-off of the adhesive. The prototype probably had positioning error caused by the processing accuracy of used machine tools about 10 μm, though we should know how the error changes the effective hinge length because this error does not change the '*average*' hinge length. The rest of the error, then, came from the adhesive. As Figure 4.2.9 shows, the pattern of the printed adhesive on the electrode parts was an aggregate of the small circles. The wavy outline is weak for T shape peeling at the beginning of

peeling. This indicates that about 10 - 20 μm long of the adhesive peeled off in each edge until the sufficient adhesion force was obtained.

5.3.4 Spring Characteristics and the Speed of Contraction and Elongation

LSEAs have the narrow gaps between the electrode parts which are sensitive to effect of air drag. In order to investigate the effect of air, the spring characteristics for a contraction and elongation speed of 50 μm/s and 500 μm/s were measured both in atmospheric pressure and a vacuum with changing the travel speed of the motorized stage.

The measurement result is shown in Figure 5.3.5, indicating that the spring rate exhibits hysteresis. All of the spring characteristics shifted to the right as the prototype elongated, and to the left as it contracted regardless of the degree of vacuum. This is due to the plastic deformation of the adhesive. Figure 5.3.6 also indicates occurrence of the plastic deformation of the adhesive because both spring constants in atmospheric pressure and vacuum increased as the contraction and elongation speed became fast.

Furthermore, the hysteresis was stronger as the elongation and contraction speed increased in atmospheric pressure. This indicates that the viscosity of air impedes the deformation of the prototype as the air flows into or out from the electrode intervals. According to the principles of hydrodynamics, the air drag F_{air} [N] that extends the gap between two parallel plates (of the thickness of d [m] and the area of S [m^2]) in a viscous fluid is proportional to the speed of the extension $\dot{d}$:

$$F_{\mathrm{air}}(d, \dot{d}) \;=\; \frac{3\rho\nu S^2}{2\pi d^3}\dot{d}, \tag{5.4}$$

where ρ is the density of air and ν is the kinetic viscosity of air. Therefore, as the travel speed of the motorized stage increases, a larger force is required to elongate and contract the prototype. In addition, the elastic force of the prototype made a significant change when the prototype switched from the completely contracted range to the soft range. The phenomenon was also due to the viscosity of air as is clear to see Figure 5.3.5d which shows that the prototype had no protrusion

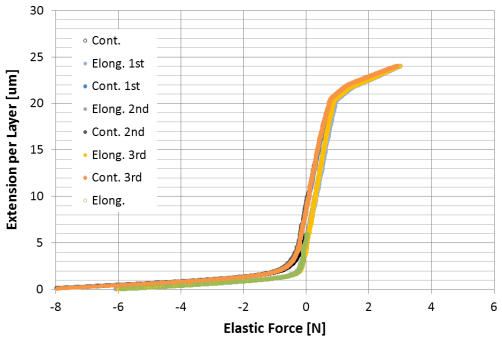

(a) Contraction and elongation speed of 50 μm/s in atmospheric pressure

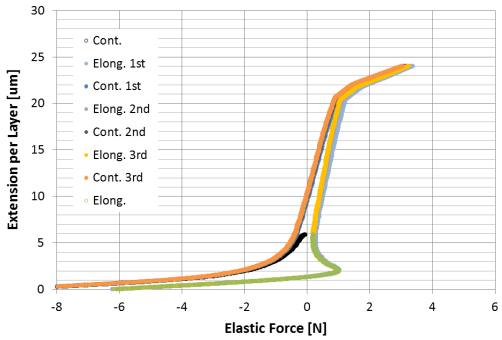

(b) Contraction and elongation speed of 500 μm/s in atmospheric pressure

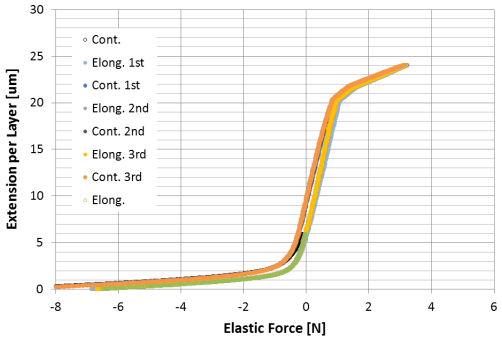

(c) Contraction and elongation speed of 50 μm/s in vacuum

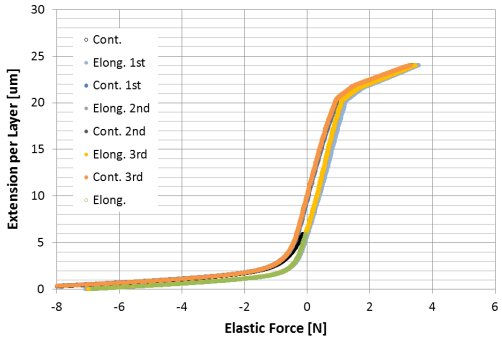

(d) Contraction and elongation speed of 500 μm/s in vacuum

Figure 5.3.5: Spring characteristics for the contraction and elongation speed of of 50 μm/s and 500 μm/s in atmospheric pressure and vacuum.

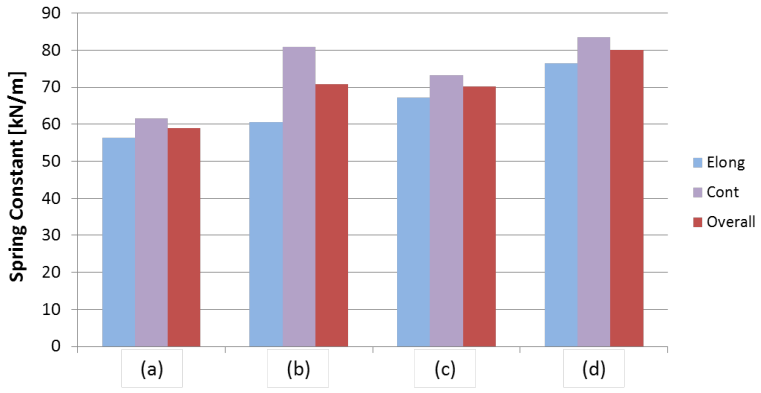

Figure 5.3.6: Spring constants during elongation and contraction, and their average ('Overall' in the graph).

between the completely contracted range and the soft range in vacuum.

According to Equation (5.4), the force required to extend the electrode intervals is inversely proportional to the cube of the intervals. In a theoretical model of two parallel plates, the gap between the electrodes cannot be extended irrespective of the magnitude of the acting tensile force. In practice, the gap between the closed electrodes can be opened by a tensile force because the electrodes are not strictly parallel plates and air can flow between them. A large force is, however, required to open the gaps. Once the gaps are opened, air easily flows into them. This is the reason for the protrusion that appears in the graph of the spring characteristics.

5.4 Concluding Remarks

The spring characteristics of Prototype A showed experimentally that LSEAs have proper spring characteristics for use as artificial muscles, i.e. the hinge parts having soft and hard range prevent overextension of the electrode intervals. The spring characteristics came from the configuration of the hinge parts and the effect of the transverse force acting on the hinge parts. The spring constant in the soft range was 38 kN/m per layer and that in the hard range was 138 kN/m.

The measurement of the spring characteristics of Prototype B showed the behavior in vacuum and the effect of air drag. The spring constant in the soft range changed with respect to the degree of vacuum from 62.6 kN/m in atmospheric pressure to 65.5 kN/m almost linearly. The calculation of the deflection of the hinge parts led that the binder layer expanded 0.16 μm (about 3 % of the thickness) per sheet of the electrode films in vacuum as compared to that in atmospheric pressure. The effect of air drag was appeared prominently when the prototype elongated from the completely contracted range to the soft range due to the short gap between the electrodes less than 3 μm.

The adhesive in both prototypes peeled from the electrode films, lengthening the effective hinge length. Improvement of the adhesion force is one of the problem to achieve durable LSEAs.

6

Actuation Characteristics

Measurement of the spring characteristics showed the structural advantage for LSEAs to use as artificial muscles and indicated some problems to solve such as peel-off of the adhesive and the effect of air drag. Here, the actuation characteristics of the prototype like the stroke, the generative force and the responsiveness are presented.

6.1 Contraction Ratio

6.1.1 Measurement Condition

In order to investigate the contraction property, brass loads were connected with the bottom clamping plate of the prototype instead of the force sensor. The loads weighed 0.12 N, 0.54 N, 0.85 N, 1.03 N and 1.27 N. The load of 0.12 N is the weight of the clamping plate. We applied voltages within a range from 50 V to 300 V at 50 V intervals in sequence. To avoid the reducing the electrostatic force by charging, the polarity of the applied voltage was switched alternately. The stroke length was calculated as the displacement after 2.5 s of application of a voltage from the

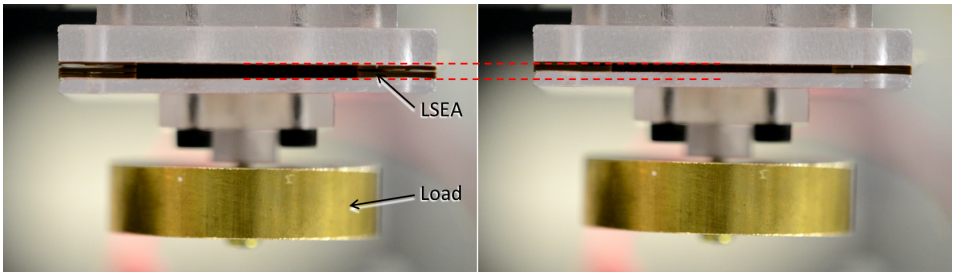

Figure 6.1.1: Prototype B at the deactivated state (left) and the activated state (right). The prototype lifted a load of 1.15 N at 250 V.

initial stretch length before activation. The displacement was measured by using the digital camera described in Subsection 5.1.2. The contraction ratio was defined as a ratio of the stroke divided by the initial stretch length for comparison with muscles or other actuators having different stroke. In this calculation, the thickness of the clamping plates was not taken into account.

6.1.2 Contraction Ratio in Atmospheric Pressure

An appearance of the prototype B at the deactivated state and the activated state is shown in Figure 6.1.1. The relationship between the applied voltage and the contraction ratio of the prototype B is presented in Figure 6.1.2. The maximum contraction ratio was -28.8 % at the voltage of 300V and the load of 0.85 N. This contraction ratio is similar to that of a muscle [10]. The contraction ratio at 0.12 N was smaller than that at 0.54 N when high voltage was applied although the load was lightweight. The reason is that the prototype was too hard to widen the electrode intervals sufficiently by a light load. This result indicates softer hinge parts should be used to achieve the larger contraction ratio even when the load is light because the flexibility of the actuator mainly depends on the elasticity of the hinge parts. Soft hinge parts will be achieved by reducing the thickness of the electrode films.

From this measurement, we calculated the actuation energy density of the prototype. The net actuation energy E_{act} can be calculated by use of the external

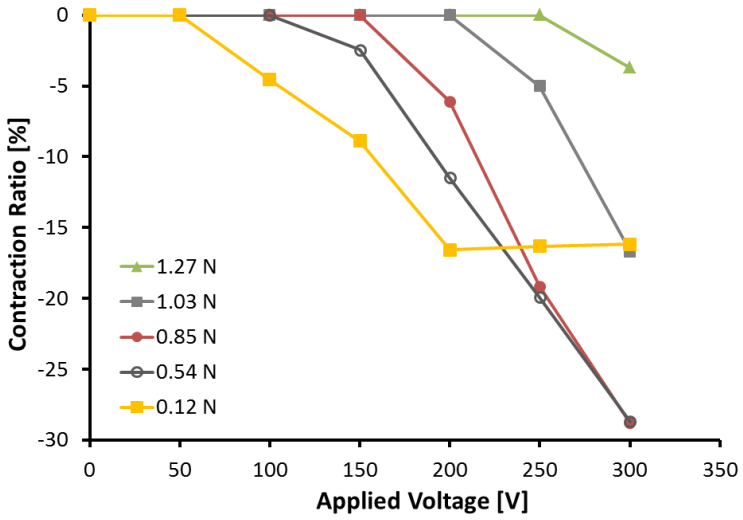

Figure 6.1.2: Relationship between the contraction ratio and the applied voltage in atmospheric pressure.

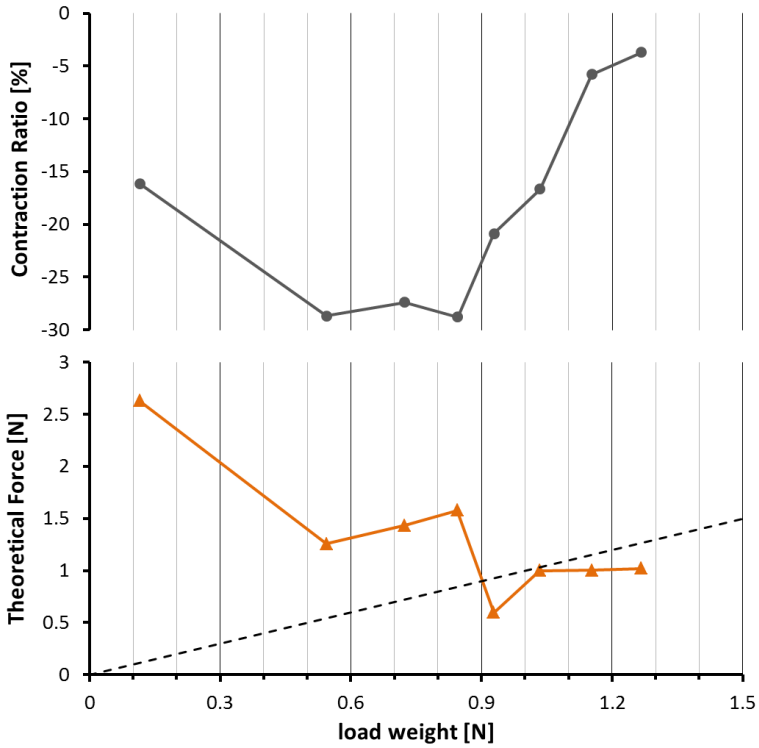

Figure 6.1.3: The contraction ratio as a function of the load weight and the calculated generative force.

force F_{ext} and the stroke L_{str} expressed as follows:

$$E_{\mathrm{act}} = F_{\mathrm{ext}} \cdot L_{\mathrm{str}}, \tag{6.1}$$

then, the net actuation energy density E_{rel} can be calculated by E_{act} divided by the mass of the prototype M of 2.4 g (excluding the mass of the clamping plates):

$$E_{\mathrm{rel}} = \frac{E_{\mathrm{act}}}{M}. \tag{6.2}$$

The maximum actuation energy density was 0.25J/kg at 300V and the load of 0.85N. The value was about 100 times lower than that of a muscle [10]. However, the actuator has the potential to achieve the high actuation energy density equivalent to or greater than a muscle because the energy density (and the force density) can be increased by shortening the hinge length which is the same as reducing the gaps between the electrode parts.

Lower graph in Figure 6.1.3 presents relationship between the load and the generative force calculated by subtracting the load weight from sum of the electrostatic force and the elastic force. The electrostatic force was calculated by Equation (3.1) using the average gap length as the gap d. The elastic force was obtained from the spring characteristics. The electrostatic force was substantially constant over the load of 0.54N because the actuator was roughly completely elongated. The dotted line in Figure 6.1.3 denotes that the calculated force equals to the load weight, i.e. the prototype cannot lift the load up in a range where the graph is lower than the dotted line if Equation (3.1) is applicable to the actuator strictly. In practice, the prototype lifted heavy load up even when the load weight was larger than the calculated electrostatic force as shown upper graph in Figure 6.1.3. The reason can be explained by variability of the electrode intervals. In the prototype, the electrostatic force contracts the narrowest electrode intervals first, following Equation (3.1) strictly, i.e. the equation is applicable to each electrode part. The motion transfers to other electrodes via the hinge, narrowing surrounding gaps between the electrodes. Some wide gaps which cannot contract first can contract by the transmission of the motion. Therefore, the actuator can contract by the cascade. To quantify the effect of the cascade, more experiments and simulations will be needed. The comparison between the load and the calculated generative force, however, can show the load weight to start reducing the contraction ratio.

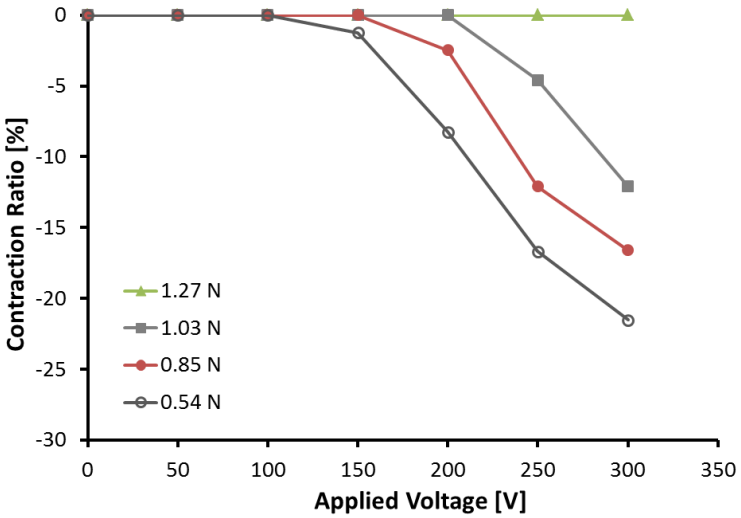

Figure 6.1.4: Relationship between the contraction ratio and the applied voltage in vacuum.

6.1.3 Contraction Ratio in Vacuum

The same experiment was carried out under vacuum. The degree of vacuum was less than 6.0×10^{-6} Torr to avoid glow discharge. Figure 6.1.4 shows the relationship between the contraction ratio and the applied voltage in vacuum. The contraction ratios in vacuum were smaller than that in atmospheric pressure despite the zero viscosity. The cause became apparent to compare the initial stretch length in atmospheric pressure and vacuum. The change of the stretch length with respect to the applied load weight is shown in Figure 6.1.5. As is clear from the graph, the prototype in vacuum showed high rigidity as compare to the prototype in atmospheric pressure.

This is thought to be due to the different spring constant in atmospheric pressure and vacuum. A stiff spring property causes shortening the stretch length at the deactivated state of an LSEA. As was described earlier, the binder in the electrode films and the adhesive were expanded by reduction of the atmospheric pressure, and the expansion of the binder increased the spring constant of the prototype. Therefore, the expansion of the materials of the prototype in vacuum reduced the initial stretch length due to increasing the spring constant. This effect caused the reduction of the contraction ratio in vacuum as compare to that in atmospheric

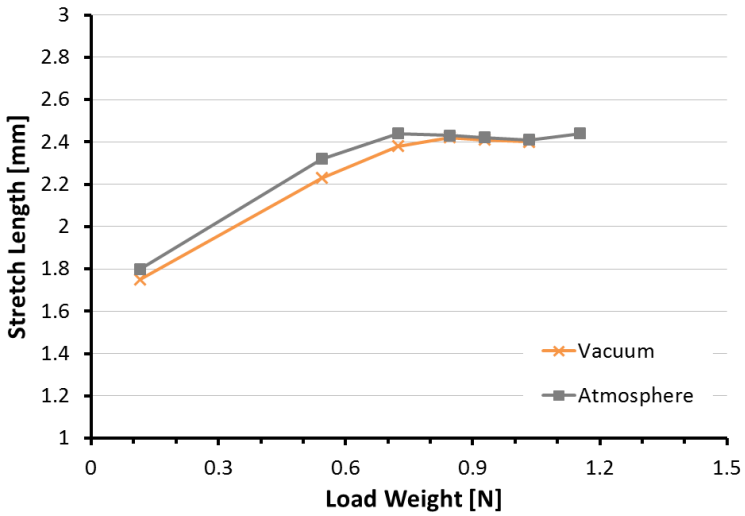

Figure 6.1.5: Difference of the initial stretch length of the prototype between in atmospheric pressure and a vacuum.

pressure when the load is lightweight. The reduction of the contraction ratio at the stretch length reached its upper limit will be explained later (see SUBSECTION 6.2.5).

We must add finally that the difference up to 90 μm of the measured stretch length could not be explained only by this approach which indicated the difference of the stretch length was about 25 μm as shown in Figure 5.3.2. The large difference seems the problem coming from the measurement accuracy of the digital camera which determined the length of the prototype.

6.1.4 Relationship with Storage Condition

In this experiment, we measured relationship between the applied voltage and the contraction ratio after elongated storage and contracted storage respectively. In the elongated storage condition, the prototype was elongated by a load of 0.12 N for 2 weeks. In the contracted storage condition, the prototype was contracted by an external force of 1.35 N for 2 weeks.

Figures 6.1.6a and 6.1.6b show the contraction ratio after the elongated storage and the contracted storage respectively. The maximum stroke was achieved at 300 V after the elongated storage when the LSEA held the load of 0.85 N up, and the contraction ratio was -21.5 % at the time. On the other hand, the contraction

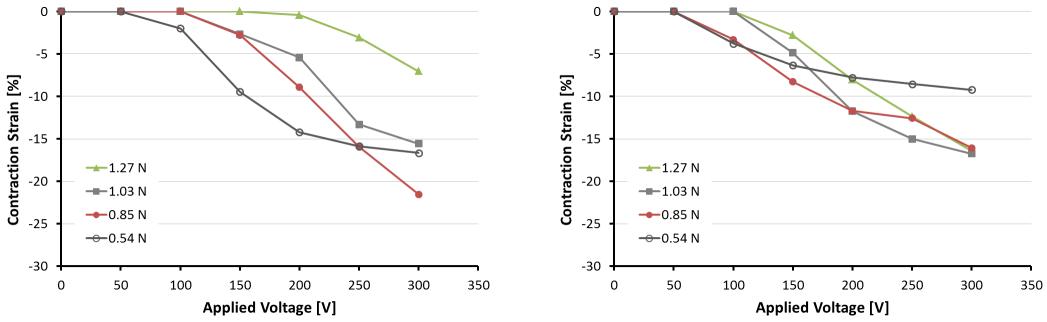

(a) Elongated storage condition **(b)** Contracted storage condition

Figure 6.1.6: Relationship between the contraction ratio and the storage condition of the prototype.

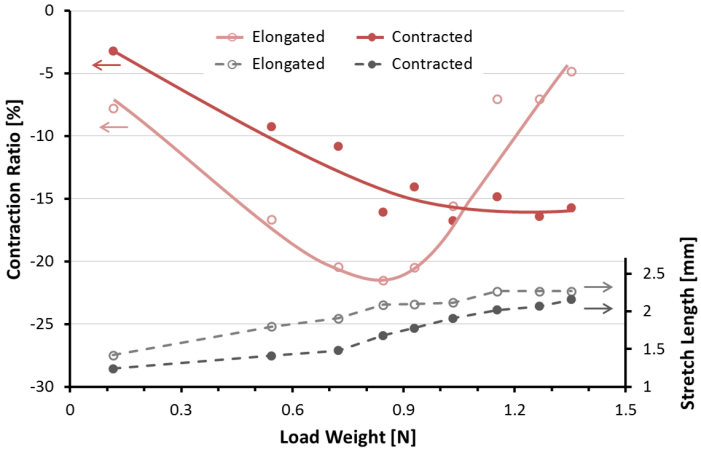

Figure 6.1.7: Relationship between the contraction ratio and the initial stretch length at 300 V.

ratio was −16.1 % under the same load and voltage after the contracted storage. The prototype, however, achieved higher contraction ratio after the contracted storage when it held up heavy loads over 1 N.

These differences are caused by the difference of the initial stretch length of the prototype under the same load. Figure 6.1.7 shows the contraction ratio and the stretch length as a function of the load weight at 300 V. The open circle represents the measurement value after the elongated storage and the filled circle represents the measurement value after the contracted storage. A comparison of the

stretch length bespeaks the prototype became harder to stretch after the contracted storage than that after the elongated storage. The prototype being hard to stretch has the short electrode interval. It can therefore contract due to the large generative force even if the load is heavy, while the contraction ratio decreases when the load is lightweight. By contrast, the prototype was easy to stretch after two weeks of elongation, which was caused by the plastic deformation and partly peeling of the adhesive. The peeling makes the hinge length longer, decreasing the electrostatic force. The contraction ratio, therefore, decreases when the load is larger than the generative force. This measurement indicates stiffer and more forceful adhesive will improve reproducibility of the contraction ratio regardless of the storage condition and prevent the generative force from unnecessarily decreasing.

6.2 Responsiveness

6.2.1 Measurement Condition

In the same manner described in Subsection 6.1.1, we measured the contraction ratio as a function of elapsed time to clarify the responsiveness. The sampling time was 33 ms, depending on the frame rate of the digital camera used to measure the displacement. We also performed the measurement of the contraction and elongation response both in atmospheric pressure and vacuum to clarify the effect of the air drag between the electrode parts. In the measurement, the degree of vacuum was kept below 6.0×10^{-6} Torr to avoid glow discharge.

6.2.2 Responsiveness in Atmospheric Pressure

Figure 6.2.1 shows the change of the contraction ratio with respect to the elapsed time under the application of a rectangular wave shifting the value between GND and 300 V at 2.5 s intervals repeatedly. The load weight was 1.15 N. In addition, the polarity of the applied voltage was switched alternately. The prototype contracted gradually and slowly although electrostatic actuators make the electrostatic force quickly. The responsiveness was greatly affected by the inertia of the load because the generative force almost equaled to weight of the load.

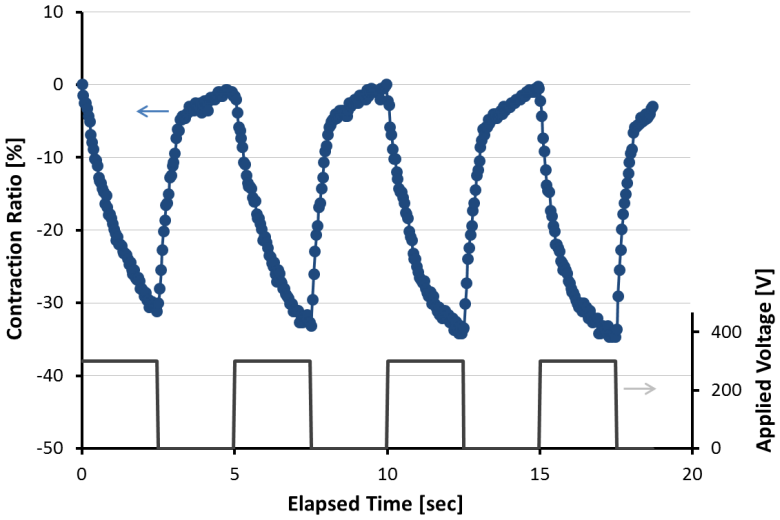

Figure 6.2.1: Waveform of the applied voltage and the contraction ratio.

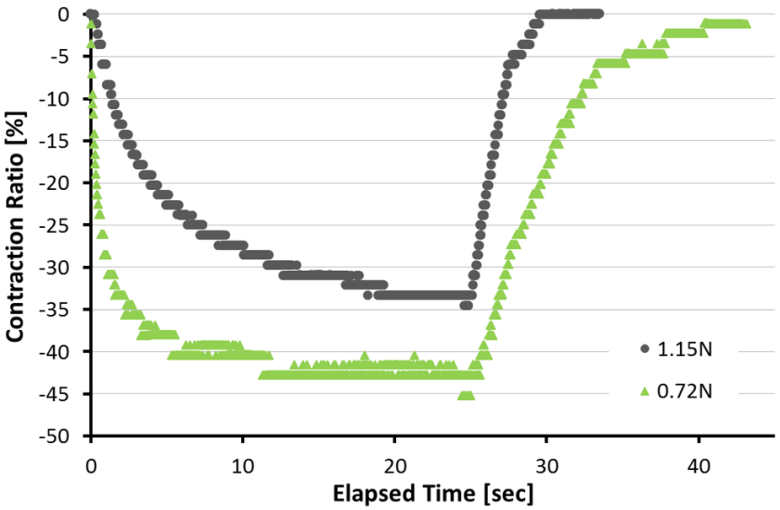

Figure 6.2.2: Comparison of the contraction ratio at the different loads.

Figure 6.2.2 shows the responsiveness at different loads of 0.72 N and 1.15 N. Discontinuous change of the graphs is caused by resolution of the camera, not reflecting the motion of each layer of the prototype. The prototype lifted a load dynamically for few seconds and kept contracting bit by bit after that, which indicates the prototype traded off the elapsed time against the contraction ratio. The contraction rate at 0.72 N was faster than that at 1.15 N because the inertia is small. The contraction rate was slow, even the maximum rate at the first 1 s from the beginning of the contraction (-28.5 %/s at 0.72 N and -6.0 %/s at 1.15 N). Inertia of the load was considered as a major reason for the slow responsiveness, yet viscosity of air and variability of the electrode intervals, etc., were also suggested as the suspect in the reduction of the contraction rate.

6.2.3 Responsiveness in Vacuum

In order to investigate the effect of the viscosity of air, we compared the contraction ratio in the same condition except for the degree of vacuum. Figure 6.2.3 presents the responsiveness of the prototype in atmospheric pressure and vacuum, showing the effect of air drag. The contraction time (defined as time during activated by the application of a voltage) was 10 s and the weight of the load was 0.72 N. The initial stretch length in vacuum was 2.43 mm similar to 2.44 mm of that in atmospheric pressure.

At the first 1 s from the beginning of the contraction, the prototype contracted dynamically regardless of difference of the pressure in Figure 6.2.3(a). After the dynamic contraction, the prototype in vacuum started to hardly contract earlier than in atmospheric pressure (see Figure 6.2.3(b)), however, the difference of the contraction ratio in atmospheric pressure and vacuum was constant in the range of (b). This shows that, regardless of difference of the pressure, a part of the electrode parts attracted to and collided with each other by pull-in phenomenon in the range of (a), and the change of the electrode intervals by the first pull-in induced the second collision between some of the rest electrode pairs (which could not contract first) in the range of (b). Similarly, the velocities of elongation were consistent between in atmospheric pressure and vacuum in the early range after switching into the deactivate state where the prototype was elongate rapidly as shown in Figure

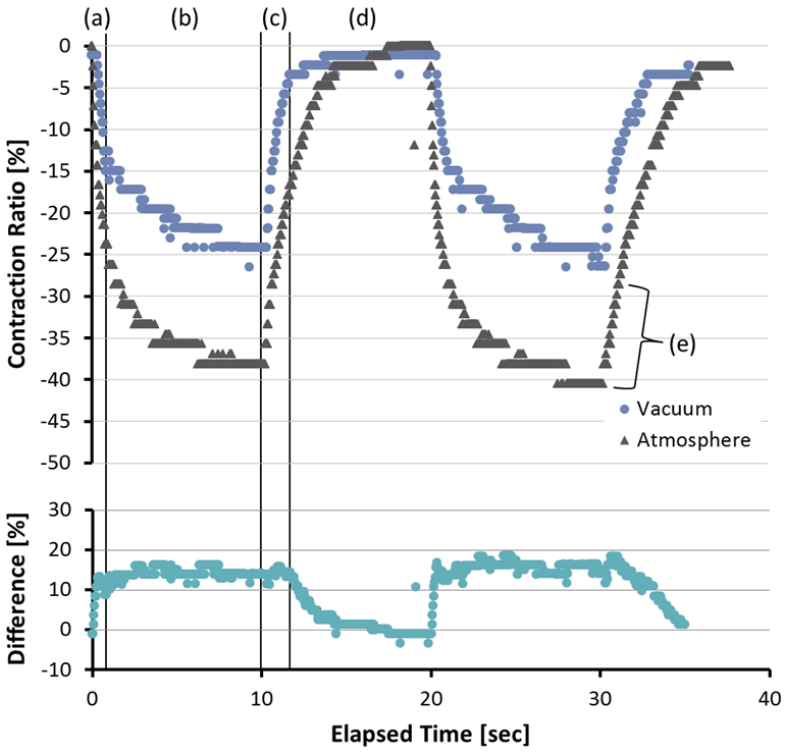

Figure 6.2.3: Comparison of the contraction ratio in atmospheric pressure and vacuum (upper) and their difference (bottom).

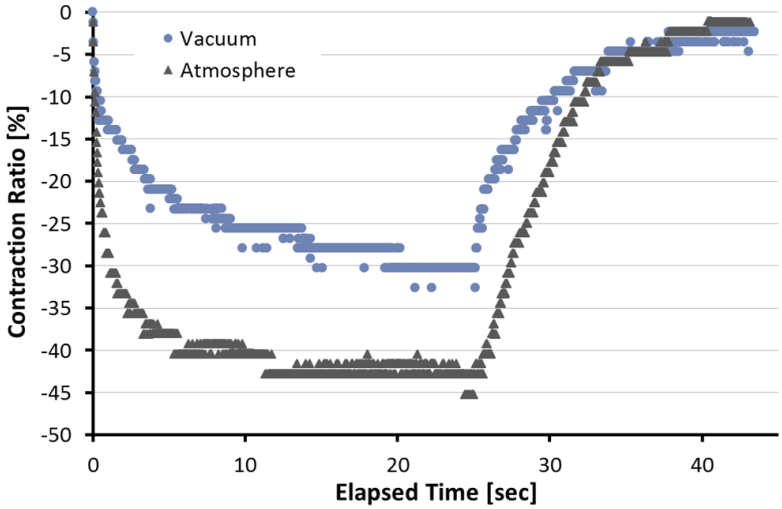

Figure 6.2.4: Comparison of the contraction ratio in atmospheric pressure and vacuum under contraction time of 25 s.

6.2.3(c). After the rapid elongation, the prototype became difficult to elongate in the range of the contraction ratio from -5 % to 0 % regardless of difference of the pressure as shown in Figure 6.2.3(d).

According to Equation (5.4), the air drag disturbing the elongation and contraction of the prototype is inversely proportional to the cube of the gap length between the electrode parts. The fact indicates that great effect of air drag becomes obvious when the electrode intervals are narrow. The measurement result, however, clarifies there was no difference in the velocity of contraction or elongation in atmospheric pressure and vacuum even when the electrode intervals were narrow in the range of (c). It should be noted that slight effect of the air drag appeared when the contraction ratio was over 40 %, the average gap length between the electrode parts of about 3 μm (see Figure 6.2.3(e)). The same thing was observed in another experiment as shown in Figure 6.2.4.

The slow contraction speed as shown in Figure 6.2.3(b) will depend on the variability of the electrode intervals. The variability produces sequential contraction of the electrode parts as previously explained in this subsection. It takes more time to start to contract the wide gaps with increasing the variability because the wider gaps increase. In the experiment, the hinge length of the prototype has about ± 10 μm variability due to the accuracy in making process. The variability should be reduced by more precise making process to reduce time of the slow contraction.

Slowdown of the elongation will come from charging. Residual charges keep generating attractive force between the facing electrodes even after short-circuiting the electrodes until the charges are annihilated by discharge. Especially, the effect appeared in the range of the contraction ratio from -5 % to 0 %. Large external tensile force helps to elongate against the attractive force by the residual charges as shown by difference of the elongation speed between 0.72 N and 1.15 N in Figure 6.2.2. This result indicates faster response can be achieved by using a pair of the actuators, one actuator contracts helping to elongate the other, like an antagonist muscle.

6.2.4 Responsiveness and Contraction Time

Figure 6.2.5 shows relationship between the contraction time and the contraction ratio at 300 V with the load of 1.15 N. The contraction ratios at the point of elongating were -7.6 % at 0.25 s of the contraction time, -21.1 % at 0.5 sec,

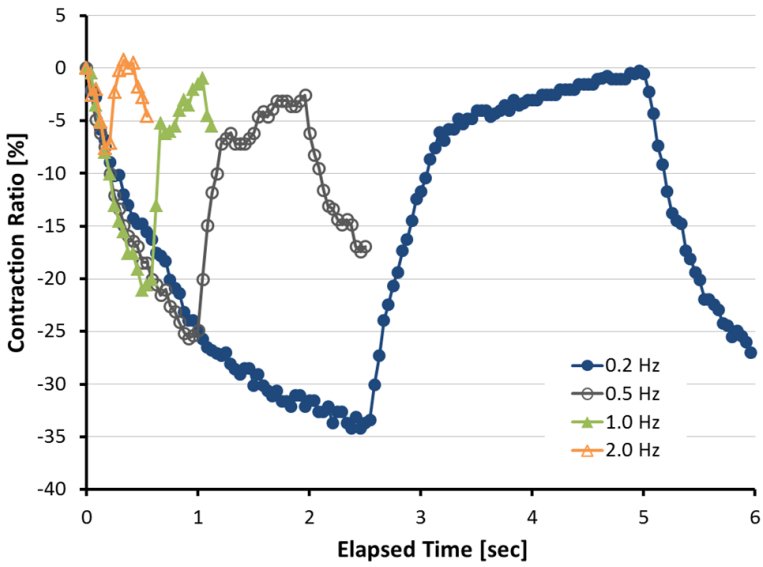

Figure 6.2.5: Comparison of the contraction ratio under the different time of application of 300 V.

-25.6 % at 1.0 s and -34.2 % at 2.5 s respectively and the maximum actuation energy density was 0.35 J/kg at 2.5 s of the contraction time. This result shows the contraction ratio decreases as the actuation frequency increases, showing the correspondence of the all change of the contraction ratios with respect to the elapsed time. Therefore, the actuator will be able to keep long stroke in a wide range of the actuation frequency by increasing the generative force.

6.2.5 Reference of the Reduction of the Contraction Ratio in Vacuum

We compared the change of the contract ratio with respect to the contraction time in atmospheric pressure and vacuum in order to investigate the relationship between the responsiveness and the effect of stiffness of the hinge parts. A load of 0.72 N was used in the experiment. The load elongated the prototype until the initial stretch length reached its upper limit of 2.42 mm in this measurement.

Figure 6.2.6a shows the measurement result of the contraction ratio. As was expected, the contraction ratio decreased under vacuum. In the measurement, increasing the spring constant seems to be the solo candidate to change geometric

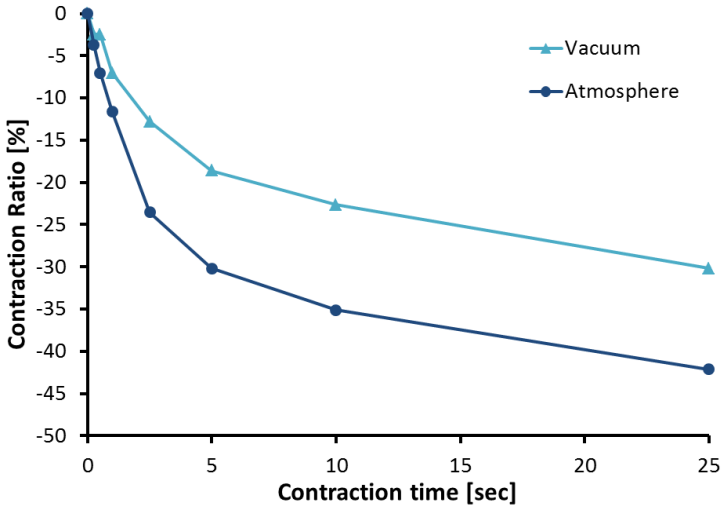

(a) Contraction ratio

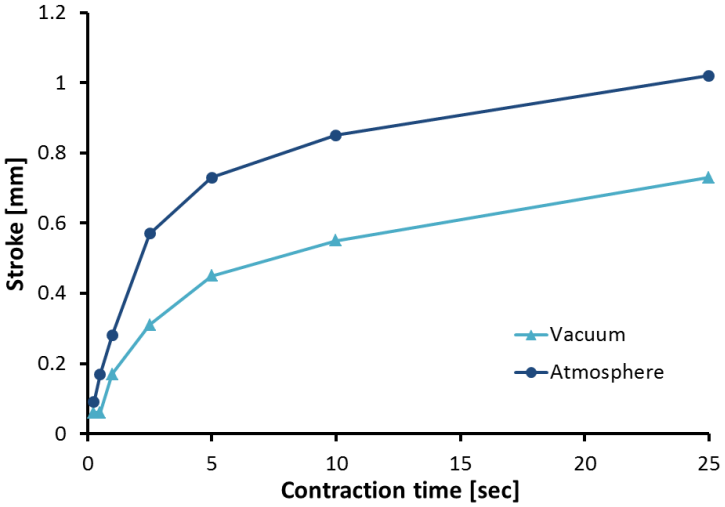

(b) Stroke (from the same initial stretch length of 2.42 mm)

Figure 6.2.6: Changes of the contraction ratio and the stroke with respect to the contraction time in atmospheric pressure and a vacuum.

form of the prototype and decrease the contraction ratio because the stretch length did not change. Actually, the measured stroke was decreased as shown in Figure 6.2.6b though the initial stretch length was constant. As shown in SUBSECTIONS 6.3.2 and 6.3.3, however, the large spring constant will help to achieve large generative force and the force value will constant regardless of the displacement of the prototype. Therefore, the increased spring constant is not the reason of the reduction of the contraction ratio.

Now we consider the electrical condition of the prototype in vacuum as the reason to explain the phenomenon. Yamano et al., observed surface charge density on PET film under AC frequency high voltage in the atmospheric condition and vacuum condition with Pockels effect [41, 42]. They reported that the surface charge distributions extend to the whole area of the PET surface after surface discharge in vacuum although the distributions exist centering around the electrode in atmospheric pressure. The surface charging in vacuum condition will reduce the electric field at air gaps in Prototype B. In addition, the surface discharge occurs at the triple junction among the PET film, the metal electrode and vacuum. It indicates that the edge faces and quadrilateral holes of the electrode film charge up after application of a voltage (if surface discharge occurs), and the charge distributions will contribute to the reduction of the generative force of LSEAs. In order to investigate the effect, we have to measure the charge density in the electrode films precisely in the future.

6.3 GENERATIVE FORCE

We enabled to know the approximate generative force by measuring the load weight to start reducing the contraction ratio in SECTION 6.1. We supposed from the result that the generative force of the prototype was similar to the electrostatic force calculated by (3.1) using the average gap length d. In order to investigate that in detail, we measured the generative force as a function of the average extension per layer – which equals to the average gap d between the electrode parts – both in atmospheric pressure and vacuum.

6.3.1 Measurement Condition

The generative force with respect to the extension was measured by using F-d measuring instrument detailed in Subsection 5.1.2. The generative force was defined as the measured force after a lapse of T_{elapse} [s] of the application of 300 V. 0 N of the generative force was set at the measured value right before the application a voltage, and therefore, the generative force represents sum of the electrostatic force and amount of the elastic force change coming from the displacement of the electrode parts. To remove the effect of charging, we carried out the next measurement after waiting for more than 3 minutes. The extension per layer ranged from 0.45 μm to 24.0 μm. Note that the prototype did not reach at the hard range through the whole experiment.

6.3.2 Relationship between the Generative Force and the Extension

Figure 6.3.1 shows the relationship between the generative force and the average gap length d between the electrode parts in atmospheric pressure after a lapse of $T_{\text{elapse}} = 12.5$ [s]. The error shows variability of the five measured values determined in a single measurement. Figure 6.3.2 shows the generative force measured in two different days. The dots represent the average values measured after a lapse of $T_{\text{elapse}} = 12.5$ [s]. The large error shows the large variability of the generative force caused by the different measurement days. The different measurement condition, such as temperature, humidity, etc., makes the minute difference in the initial position of the electrode parts, changing the pull-in condition. Therefore, it is difficult to quantitatively evaluate the generative force as a function of the gap length between the electrode parts.

The curve in this figure denotes the electrostatic force calculated by Equation (3.1) using the average gap d. The measurement shows the following qualitative results with respect to the gap d.

- $\underline{d < 12\ [\mu\text{m}]}$ The generative force was approximately constant except for that at 0.45 μm/layer of the gap length, and smaller than the calculated electrostatic force.

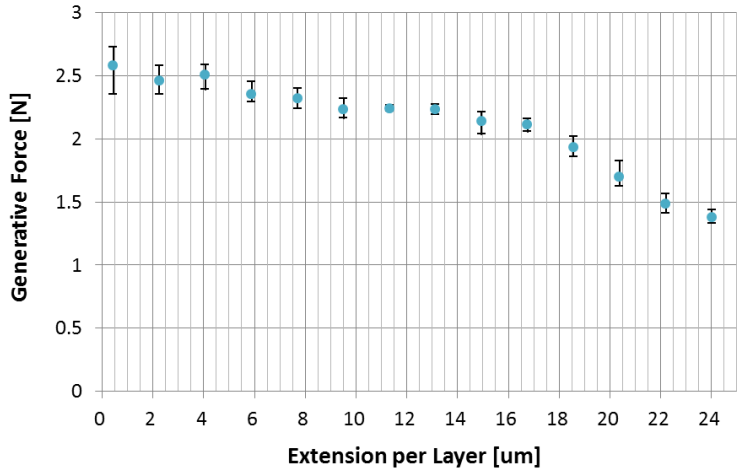

Figure 6.3.1: Generative force at 300 V after a lapse of 12.5 s as a function of the gap between the electrodes in atmospheric pressure.

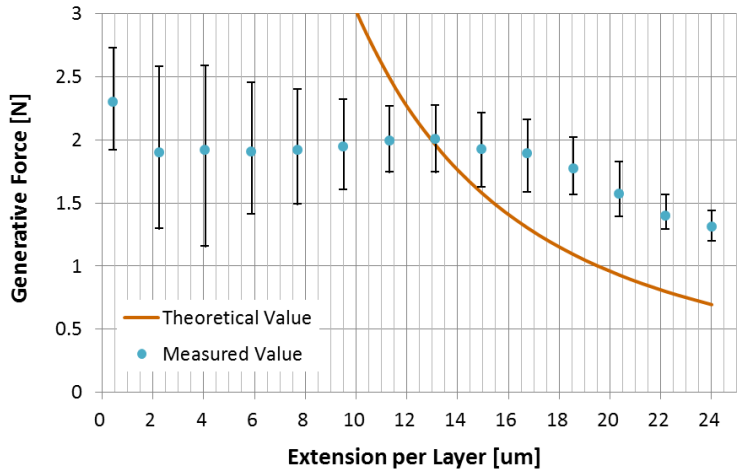

Figure 6.3.2: Average generative force at 300 V after a lapse of 12.5 s as a function of the gap between the electrodes in atmospheric pressure and the curve of the calculated electrostatic force.

- d = 12-14 [μm] The generative force was similar to the calculated electrostatic force.

- d > 14 [μm] The generative force was larger than the calculated electrostatic force.

These reason can be explained qualitatively using a simple model of a multi-layered electrostatic actuator. Let us consider a multi-layered electrostatic actuator consisting of many parallel plate electrodes (laminated with an insulator) connected with the neighbor electrode by a spring. The springs are linear spring of the spring constant k, and each air gap between the electrodes is set at d first. When a voltage V is applied between the electrodes, the electrostatic force is expressed as Equation (3.1).

If all of the initial gaps between the electrodes are strictly d, the generative force equals to Euqation (3.1) regardless of the elasticity of the springs. Here, let's take a look at the stability of the air gap at the time by calculating energy of a two-layered actuator. The potential energy of the actuator is expressed below as a sum of the elastic energy and the electrostatic energy in regard to the displacement of the air gap d':

$$U_{\mathrm{tot}}(d') = kd'^2 - \frac{1}{2}\frac{\varepsilon_0 S V^2}{\dfrac{t}{\varepsilon_1} + \dfrac{d-d'}{\varepsilon_2}} - \frac{1}{2}\frac{\varepsilon_0 S V^2}{\dfrac{t}{\varepsilon_1} + \dfrac{d+d'}{\varepsilon_2}}, \tag{6.3}$$

where, the first term denotes the total elastic energy of the two spring, the second term is the electrostatic energy between the electrode of the gap of $(d - d')$ and the third one is the electrostatic energy of the gap of $(d + d')$. The variables are the same as them in Equation (3.1). The air gap $(d - d')$ is stable at the local minimum of U_{tot}. Figure 6.3.3 is the potential energy of a two-layer actuator having the initial air gap $d = 25[\mu\mathrm{m}]$. This graph shows that the initial gap d is not always stable, depending on the spring constant and the magnitude of the electrostatic force.

In order to estimate the actual generative force of Prototype B, a pull-in model should be considered. Here we discuss a quasi-static model to simplify the calculation. Let us consider n-layered actuator whose $(i - 1)$ layers have been completely contracted already (therefore, the electrostatic force has been also applied)

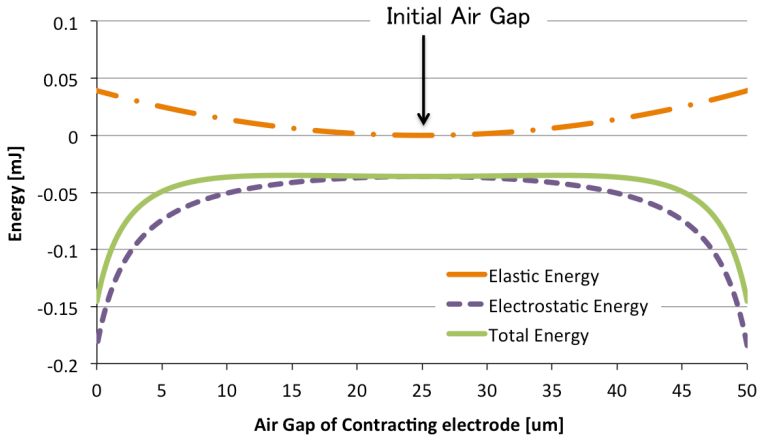

Figure 6.3.3: Potential energy of a two-layered electrostatic actuator with respect to the air gap $(d - d')$.

as shown in Figure 6.3.4 (ii). In this state, the air gap in the rest of the $n-(i-1)$ layers is $\dfrac{n}{n-(i-1)}d$. When a layer displaces $\dfrac{n}{n-(i-1)}d'$ $(0 \leq d' \leq d)$ virtually, the air gap $d_{\rm cont}$ between the layer (called 'contracting layer') and $d_{\rm rest}$ between the rest of n layers are

$$d_{\rm cont} = \frac{n}{n-(i-1)}(d-d') \ , \quad d_{\rm rest} = \frac{n}{n-(i-1)}\left(d - \frac{d'}{n-i}\right). \tag{6.4}$$

Then, the total potential energy after the displacement is expressed as follows:

$$U_{\rm tot}(d') = U_{\rm elas}(d') + U_{\rm elec}(d'), \tag{6.5}$$

here,

$$U_{\rm elas}(d') = (n-i)\cdot k\left\{\frac{n}{n-(i-1)}\left(1+\frac{1}{n-i}\right)d'\right\}^2 \tag{6.6}$$

$$\begin{aligned} U_{\rm elec}(d') = & -\frac{1}{2}\frac{\varepsilon_0 S V^2}{\dfrac{t}{\varepsilon_1}+\dfrac{1}{\varepsilon_2}\dfrac{n}{n-(i-1)}(d-d')} \\ & -(n-i)\cdot\frac{1}{2}\frac{\varepsilon_0 S V^2}{\dfrac{t}{\varepsilon_1}+\dfrac{1}{\varepsilon_2}\dfrac{n}{n-(i-1)}\left(d+\dfrac{d'}{n-i}\right)}. \end{aligned} \tag{6.7}$$

The minus value of a differential of the total potential energy $U_{\rm tot}$ by d' represents

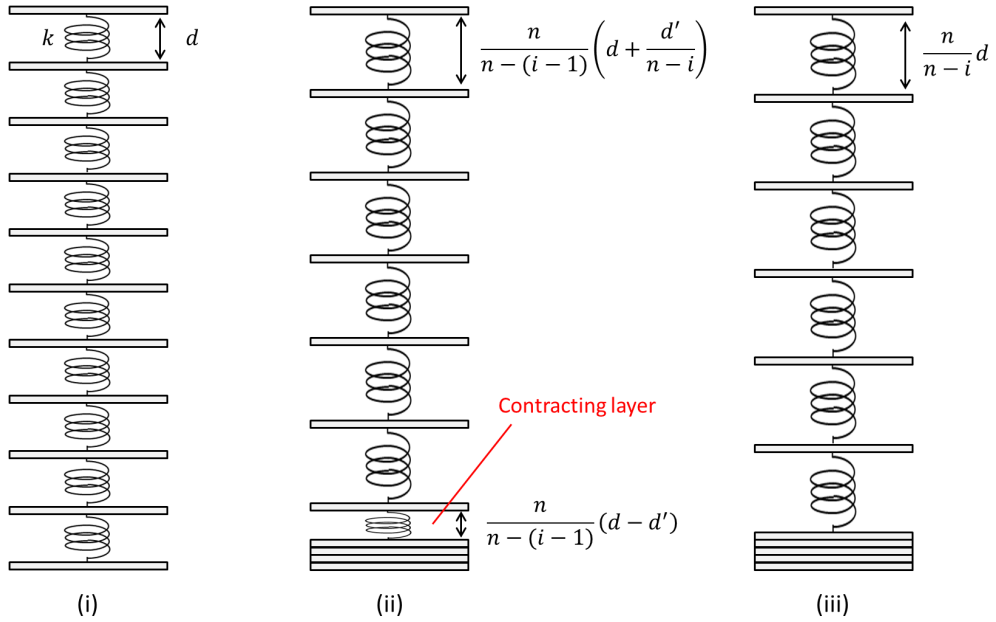

Figure 6.3.4: Schematic of the multi-layered electrostatic actuator whose electrodes are connected with the adjacent electrode by a spring k. (i) Initial condition, (ii) a state under contraction of a layer (the $i-1$ layers already have been completely contracted) and (iii) a state where the i layers have been completely contracted.

increase of d', i.e. continuation of the contraction. Therefore the pull-in condition equation is shown as follows:

$$\frac{dU_{\text{tot}}(d')}{dd'} < 0 \quad \text{in regard to} \quad {}^{\forall}d' \ (0 \leq d' < d). \tag{6.8}$$

The equation implies that the contracting layer will be completely contracted if the attractive force surpasses the repulsive force for all d'. In other words, the condition equation is true when the sum of the electrostatic force between the contracting layer (attractive force) and the rest of the layers (repulsive force) surpasses the increment of the elastic force of the springs between the contracting layer (repulsive force) and the rest of the layers (repulsive force) at the displacement d'_0 where the differential of the net force is zero. This is expressed in mathematical forms below:

$$F_{\text{elec}}(d'_0) - F_{\text{elas}}(d'_0) > 0 \quad \text{when} \quad \frac{d}{dd'}\left(F_{\text{elec}}(d') - F_{\text{elas}}(d')\right)\Big|_{d'=d'_0} = 0 \tag{6.9}$$

here,

$$F_{\mathrm{elas}}(d') = k\frac{nd'}{n-(i-1)}\left(1+\frac{1}{n-i})\right) \tag{6.10}$$

$$F_{\mathrm{elec}}(d') = F_{\mathrm{elec}}^{\mathrm{LSEA}}\left(\frac{n}{n-(i-1)}(d-d')\right) - F_{\mathrm{elec}}^{\mathrm{LSEA}}\left(\frac{n}{n-(i-1)}\left(d+\frac{d'}{n-i}\right)\right) \tag{6.11}$$

Furthermore, the differential and the second order differential of $F_{\mathrm{elec}}(d')$ are both plus for all d' $(0 \leq d' < d)$. Therefore, the pull-in condition equation is expressed as follows:

$$\frac{d}{dd'}\left(F_{\mathrm{elec}}(d') - F_{\mathrm{elas}}(d')\right)\Big|_{d'=0} > 0, \tag{6.12}$$

and, we also gain the pull-in condition equation of the air gap d by solving Equation (6.12):

$$d < -\frac{\varepsilon_2}{\varepsilon_1}t + \frac{n}{n-(i-1)}\sqrt[3]{\frac{\varepsilon_2\varepsilon_0 SV^2}{k}} \tag{6.13}$$

The calculated result about 50-layer actuator is shown in Figure 6.3.5. In this calculation, spring constant in the soft range was used as k. For comparison, a force values calculated from Equation (3.1) by using the average air gap d (no pull-in model) and the experiment value in Figure 6.3.2. The pull-in model corresponds well with the experiment value especially for short d, indicating that pull-in model is closer to the actual actuator than no pull-in model. The calculation, however, cannot explain the measured value over $d = 6$ quantitatively. Table 6.3.1 shows the comparison of the number of the pull-in layers i in pull-in model and another pull-in model where we arrange the number of pull-in layers i to fit the experiment value. This indicates pull-in phenomenon might occur in more layers of Prototype B.

The difference will be explained by three reasons as follows. One of the reasons is errors caused by quasi-static pull-in model. Figure 6.3.6 shows potential energy at $d = 24\mu$m and $i = 20$. As the total energy shows, the air gap cannot decrease due to a mountain of the potential. however, difference between the potential energy at initial air gap and the maximum potential energy is only 10μJ. This value is the same as kinetic energy of a electrode layer with 0.6-0.7 m/s of the speed. Therefore, if a few layers start to contract, surrounding electrodes have some speed

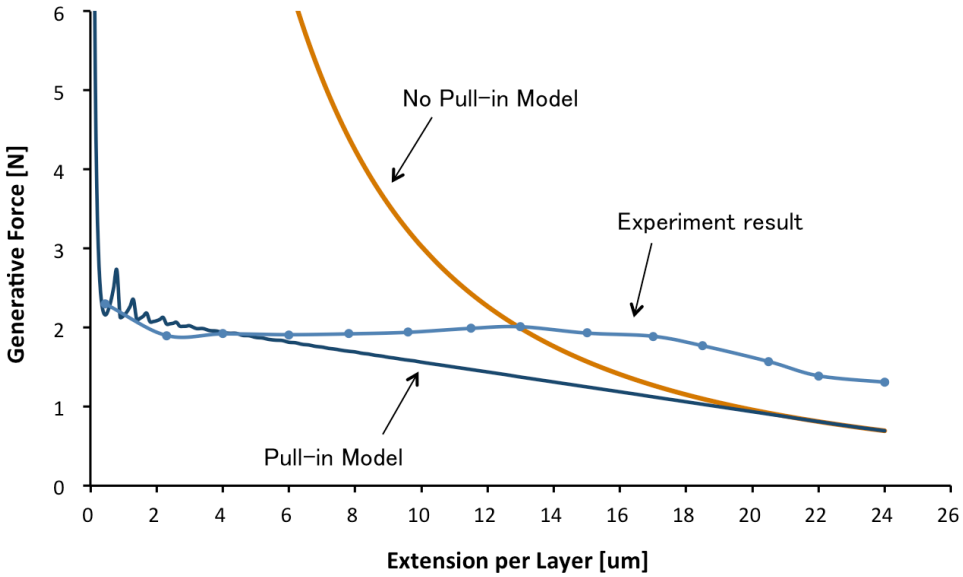

Figure 6.3.5: Generative force of calculated model (pull-in model and no pull-in model) and the experiment result.

and additional layers having kinetic energy can contract like a chain reaction.

Another reason is the variability of the air gaps. It induces difference of the electrostatic force and makes the layers easier to pull in. Although it is hard to solve this pull-in model, we can solve it approximately when the air gap in the contracting layer is $d - \delta$ ($\delta \ll d$). Here the rest of the layers have $d + \dfrac{\delta}{n-i}$. The approximate solution of Inequality (6.12) is

$$d < -\frac{\varepsilon_2}{\varepsilon_1}t + \frac{n}{n-(i-1)}\sqrt[3]{\frac{\varepsilon_2\varepsilon_0 SV^2}{k}}(1+\delta'), \tag{6.14}$$

Table 6.3.1: Number of the pull-in layers i in the pull-in model (Model 1) and that suited to the experiment result (Model 2).

Air gap [μm]	0.45	2.30	4.0	6.0	7.8	9.6	11.5	13.0	15.0	17.0	18.5	20.5	22.0	24.0
Model 1	49	45	41	37	33	29	25	21	17	12	9	5	1	0
Model 2	49	45	41	39	38	36	35	34	32	30	28	25	22	20

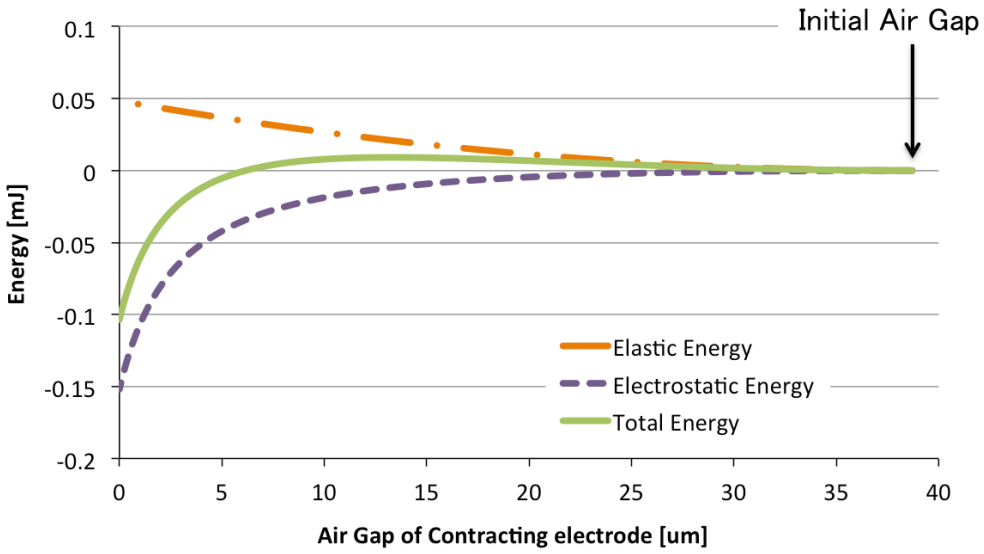

Figure 6.3.6: Calculated potential energy of 50-layered actuator at $d = 24\mu\mathrm{m}$ and $i = 20$.

here, $\delta'(\delta' \ll 1)$ is

$$\delta' = \delta \cdot \frac{3n\left(n - i - \dfrac{1}{n-i}\right)}{\{n-(i-1)\}^2} \cdot \frac{1}{\dfrac{\varepsilon_2}{\varepsilon_1}t + \dfrac{n}{n-(i-1)}}. \tag{6.15}$$

As the inequality shows, the d is permitted to have larger value than that in $\delta = 0$. It indicates the possibility that more layers in the actual actuators will contract completely. In this calculation, we should also consider the difference of the spring constant at each layer. This calculation will be future work.

Finally, it should be noted that the generative force is not contained the external force to pull the prototype in this measurement, and the sum of the generative force and the external force is 2.2 N almost constantly regardless of the air gaps in the pull-in model. It indicates that Prototype B can lift a load of 2.2 N regardless of the stretch length. The value correspond to the minimum value of the sum of the electrostatic force and the elastic force, i.e., the electrode parts will move until the electrode parts settle at the stable position, and at the time, the forces acting on the electrode parts will balance when they will reach at the minimum.

6.3.3 Generative Force and the Degree of Vacuum

Figure 6.3.7 shows the the generative force measured in two different days in the different degree of vacuum. In this measurement, The value T_{elapse} was 12.5 s (Figure 6.3.7a is exactly the same as Figure 6.3.2). The generative force had a tendency to decrease as the degree of vacuum increased. The relationship between the generative force and the degree of vacuum is shown in Figures 6.3.8 for $T_{\text{elapse}} = 12.5$ [s] and 6.3.9 for $T_{\text{elapse}} = 60$ [s]. The graph legends denotes the average extension per layer of the prototype. Both figures show the generative force decreased linearly with the degree of vacuum regardless of the extension length, having the same slope.

The change of the generative force may be due to the effect of charging in vacuum as mentioned in Subsection 6.2.5. For more quantitative investigation, we should measure precisely the surface charging of electrode films along with clarification of the reduction of the contraction ratio. Here, we point out that the change of the spring constant in regard to the degree of vacuum is not the reason of the phenomenon because the harder hinges are associated with increased rather than decreased generative force due to calculation by using the method explained previously in Subsection 6.3.2 with spring constant in the soft range in vacuum.

6.3.4 Problem – Significant Increment of the Generative Force at High Vacuum at Short T_{elapse}

There is a problem to solve about the generative force in vacuum except for the quantitative evaluation of the generative force. Figure 6.3.10 shows the generative force with respect to the degree of vacuum at $T_{\text{elapse}} = 2.5$ [s]. As you can see, the generative force significantly increased at high vacuum (~ 0 atm) although ones at 0.2 atm and 0.4 atm were lower than it. In fact, this phenomenon also appeared at $T_{\text{elapse}} = 12.5$ (see Figure 6.3.8).

We cannot figure out what is behind it in this study, however, we have a clue to solve the problem. Figure 6.3.11a shows the change of the generative force as a function of the elapsed time in each pressure. The starting points of the application of the voltage were defined as 0 s. It should be noted that the graph seem to be

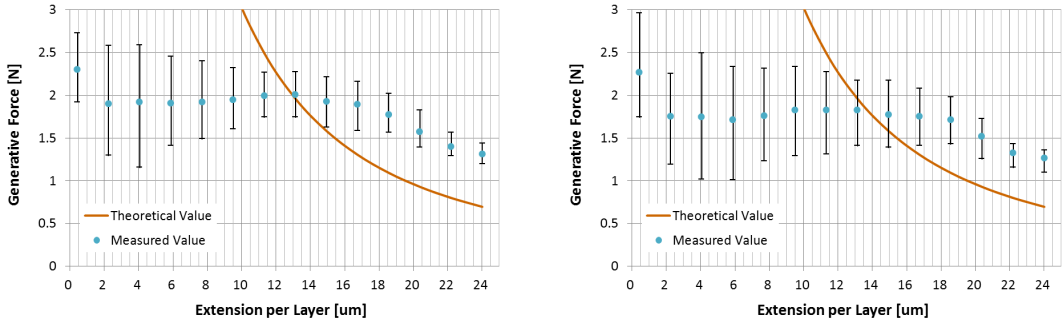

(a) Atmospheric Pressure

(b) 0.8 atm

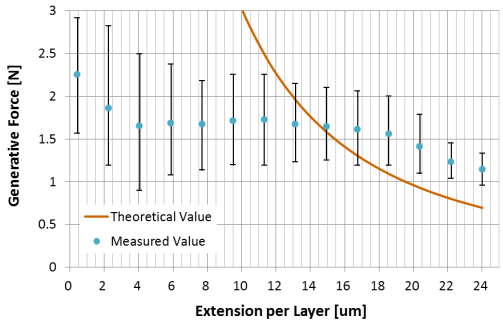

(c) 0.6 atm

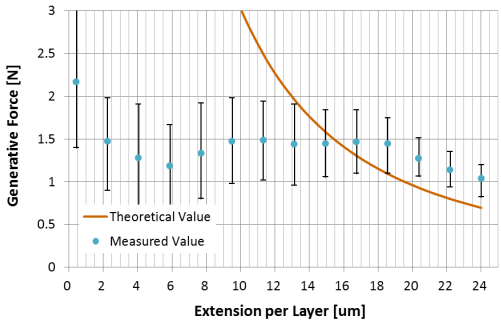

(d) 0.4 atm

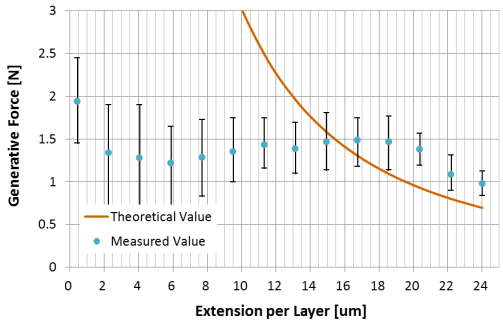

(e) 0.2 atm

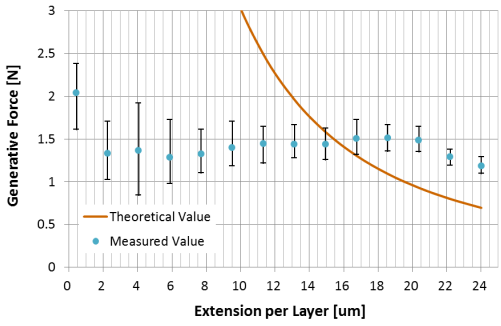

(f) Vacuum

Figure 6.3.7: Generative force at 300 V after a lapse of 12.5 s as a function of the gap between the electrodes in the different degree of vacuum.

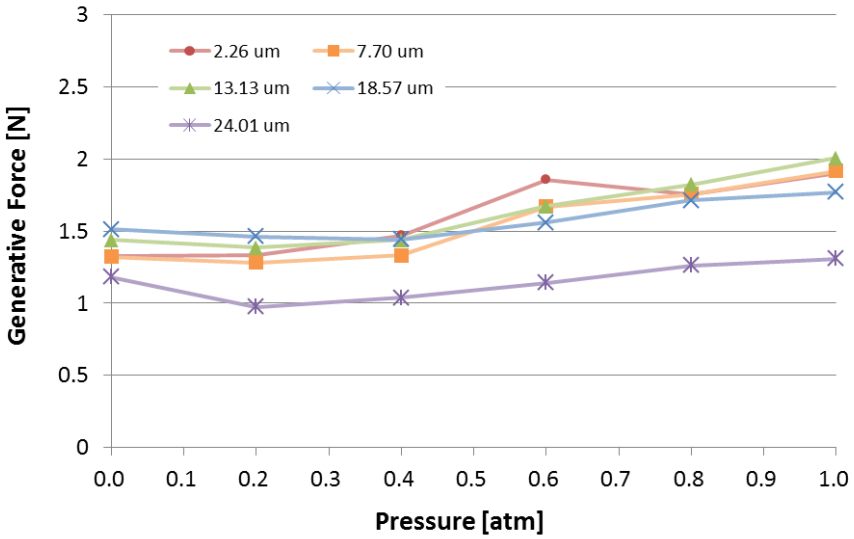

Figure 6.3.8: The generative force after a lapse of 12.5 s as a function of the degree of vacuum.

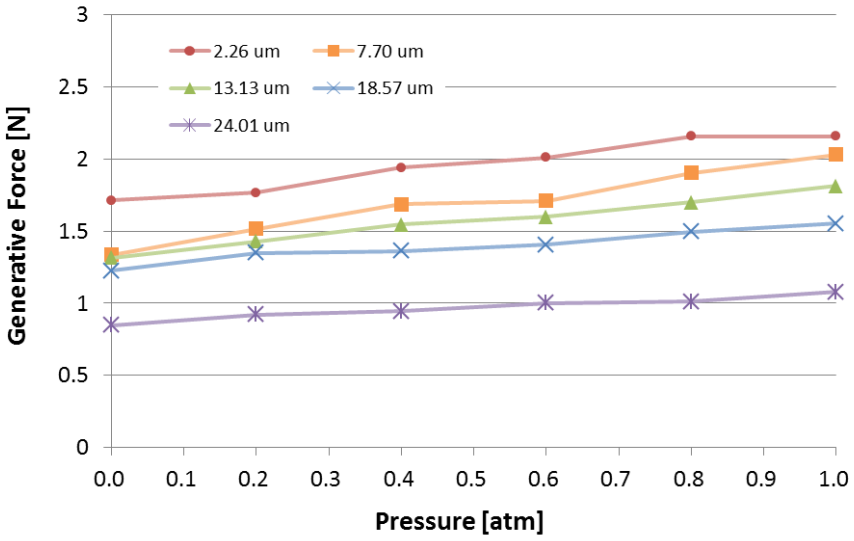

Figure 6.3.9: The generative force after a lapse of 60 s as a function of the degree of vacuum.

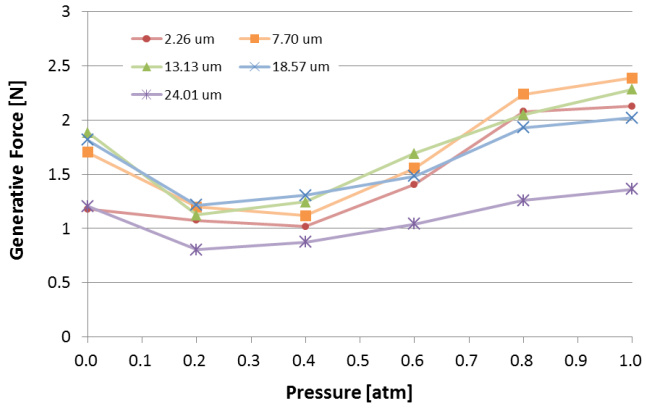

Figure 6.3.10: The generative force at 300 V after a lapse of 2.5 s as a function of the degree of vacuum.

similar to the contraction property, but the prototype did not change its length in this experiment. Figure 6.3.11b was made by shifting the graphs in Figure 6.3.11a in order to accord the vertexes. This figure exhibits that all of the slopes after the initial rise matched well, showing that only initial rises were different. The change of the initial rise seems to come from the electrical properties, not the spring characteristics of the prototype. Our hypothesis is as follows:

- The initial rise in high vacuum can be increase for any reason
- After the initial rise, the generative force reaches the static steady taking time. The steady state depends on the spring characteristics, and therefore the generative force is proportional to the degree of vacuum.

In order to prove it, the charged state of the materials, the surface state, etc. should be investigated particularly in different degree of vacuum (or in different gases if needed).

6.4 Concluding Remarks

Contraction ratio

The measurement of the contraction ratio revealed that the prototype had the high contraction ratio of -28.8 % at a load of 0.85 N at 300 V either equaling

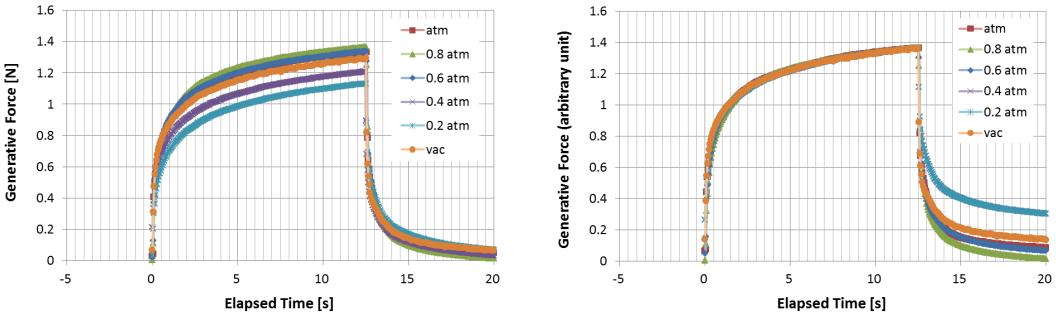

(a) Measured values **(b)** Comparison of the slope

Figure 6.3.11: Change of the generative force under the different degree of vacuum.

or surpassing the contraction strain of biological muscles. The contraction ratio decreased not only at a heavy load (over 1 N) but also a light load (0.12 N) due to stiffness of the hinges in the soft range. The effect of stiffness of the hinge parts also appeared in the measurement of the contraction property in vacuum, resulting on the reduction of the initial stretch length, because expansion of the binder increased the flexural rigidity (second moment of area, more properly) of the hinges.

The actuation energy density was 0.25 J/kg at a load of 0.85 N at 300 V which was about hundredth of that of muscles because the electrostatic force was not sufficiently high. To overcome these drawbacks, thin and short (but tough and hard-breakdown) hinge parts should be used for LSEAs.

The comparison of the storage condition indicated that the actuation performance changed due to the plastic deformation or peeling of the adhesive. More forceful adhesive will improve reproducibility of the contraction ratio regardless of the storage condition and keep the actuation performance for long periods.

Responsiveness

The responsiveness of the prototype easily changed with the applied load due to inertia of the load. To achieve the high responsiveness, sufficiently high electrostatic force is necessary. The comparison of the responsiveness in atmospheric pressure and vacuum showed that the effect of air drag was not dominant and it slightly appeared only when the average gap between the electrodes was less than 3 μm in the experiment.

Generative force

The relationship between the generative force and the gap between the electrode parts was measured. The generative force was smaller at the narrow extension than the electrostatic force calculated by using the average gap because the actual behavior of the prototype should have been expressed by pull-in model. However, the generative force exceeded the calculated electrostatic force at somewhat elongated state. This indicates more air gaps contracted completely than that we expected because of the dynamic pull-in phenomenon or the variability of the gap lengths and the spring constants.

The decreasing of the generative force in regard to the degree of vacuum seems to come from difference of the charging condition between atmospheric condition and vacuum condition, which should be solved quantitatively by measurement. Clarification of the charging condition is important future work in order to explain the reduction of the contraction ratio in vacuum as well as the generative force. Furthermore, we have to solve the problem about the significant increment of the generative force at high vacuum at short T_{elapse}.

7

Power Consumption

Generally, electrostatic actuators have an advantage about the high energy efficiency. Especially, the energy loss is very low due to the voltage driving when it keep holding a load in the same position, only slight leak current flows in the actuators. In this chapter, we estimated the power consumption of Prototype B by measuring the current flowing after the application of a voltage both in atmospheric pressure and vacuum.

7.1 Measurement Method

We measured the electric current applied to the prototype after the application of 300 V in the different extension per layer d in atmospheric pressure and vacuum. The prototype was fix the top and bottom clamping plate by the measuring instrument as shown in Figure 5.1.2. The voltage was applied from an ultra high resistance meter (8340A, manufactured by ADCMT, Japan) which has the measurement range from 10 fA to 19.999 mA. In this measurement, we measured the change of the current for 180 s starting from the application of the voltage. The sampling rate was 8.87 Hz. In addition, we also measured the steady current de-

fined as the current after 10 min of application of 300 V at $d = 5.9[\mu\text{m/layer}]$ in atmospheric pressure.

7.2 Steady Current

The measured steady current was 2.1×10^2 nA although the steady current flowing into the insulated capacitor is ideally zero. According to Equation (3.2), the current applied to Prototype B can be estimated approximately by the volume resistivity $\sigma = 10^{18}[\Omega \cdot \text{cm}]$ of the PET films. Here, S_{tot} is the product of the electrode area per sheet, 12.6 cm^2, and the number of electrode films, about 100, and t is the thickness of the PET film per layer, 3 μm, in this case. The steady current I_s was obtained as about 1 nA which was below hundredth of the measurement value although we estimated it much more by neglecting the thickness of the binder and air gap.

The calculation indicates the existence of the creeping discharge on the electrode films of the prototype. It seems to be due to the bear copper along the edge faces of the prototype. If we can infill the minute air gap between the PET films with some insulator, the steady current will be less than hundredth of the measured value.

7.3 Power Consumption

Figure 7.3.1 shows the measured current in the different extension per layer of 0.45 μm, 5.9 μm, 15.0 μm and 24.0 μm in atmospheric pressure. The high steady current at $d = 0.45[\mu\text{m/layer}]$ seemed to be due to the narrow air gap and increasing the contact area of the electrode films, inducing more creeping discharge.

The current rapidly decreased at the first few seconds, however, the reduction rate was slow although the resistance component arranged in series with the prototype was almost zero. The slow reduction rate came from the change of the capacitance of the prototype. As shown in the previous section, the prototype was electrically equivalent to a capacitor placed in parallel with a resistor. Therefore, the current applied in the capacitor is calculated by the difference between

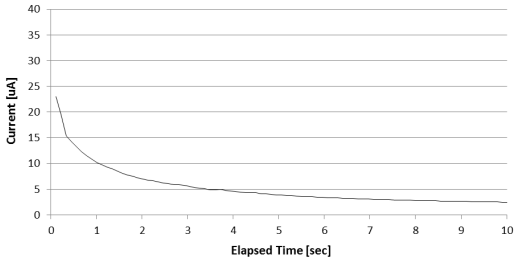

(a) $d = 0.45\mu\mathrm{m/layer}$ (0-10 s)

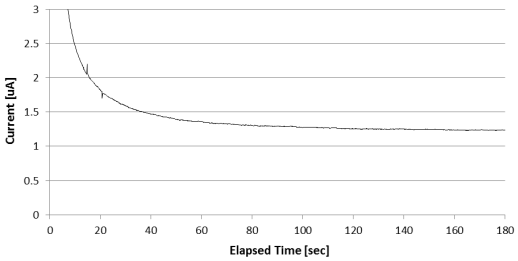

(b) $d = 0.45\mu\mathrm{m/layer}$ (0-180 s)

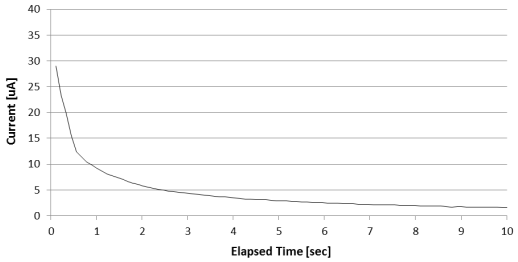

(c) $d = 5.9\mu\mathrm{m/layer}$ (0-10 s)

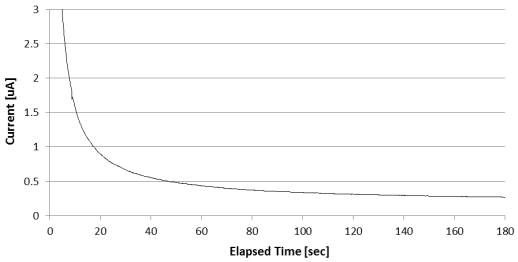

(d) $d = 5.9\mu\mathrm{m/layer}$ (0-180 s)

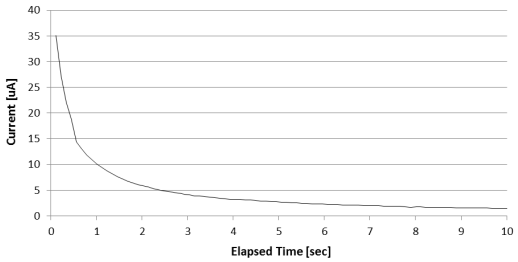

(e) $d = 15.0\mu\mathrm{m/layer}$ (0-10 s)

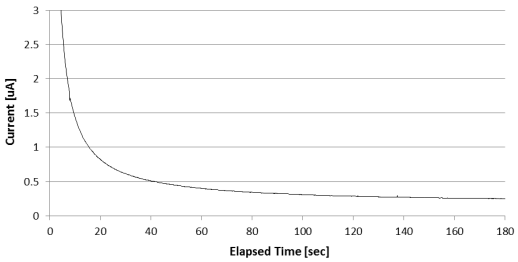

(f) $d = 15.0\mu\mathrm{m/layer}$ (0-180 s)

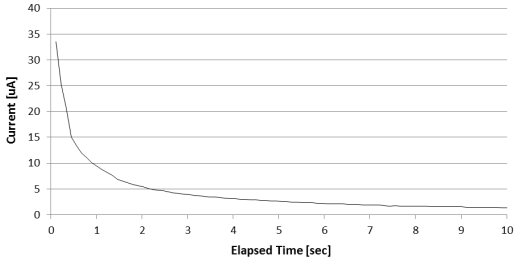

(g) $d = 24.0\mu\mathrm{m/layer}$ (0-10 s)

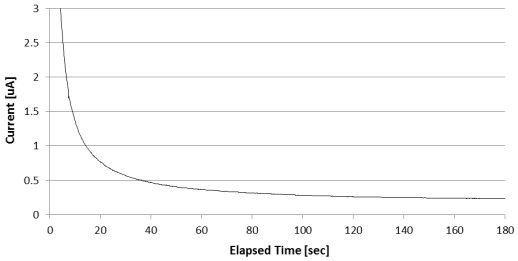

(h) $d = 24.0\mu\mathrm{m/layer}$ (0-180 s)

Figure 7.3.1: Power consumption in the different average gaps between the electrode parts for 10 s starting from the application of 300 V (left graphs) and 180 s (right graphs).

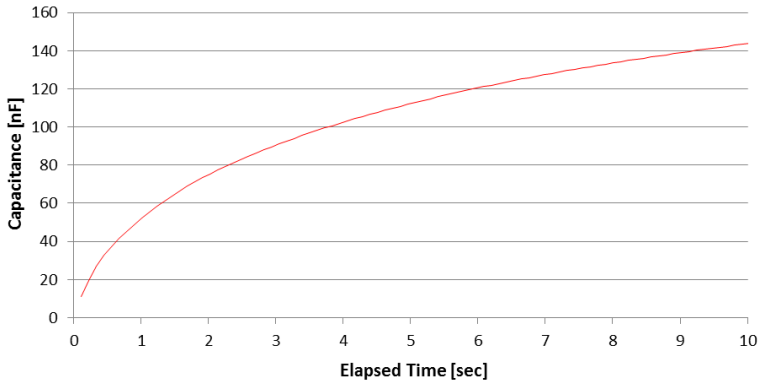

Figure 7.3.2: Change of the capacitance with respect of time of application of 300 V (0-10 s).

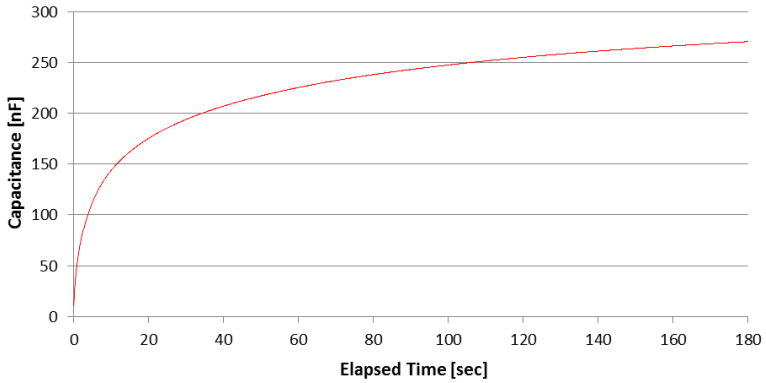

Figure 7.3.3: Change of the capacitance with respect of time of application of 300 V (0-180 s).

the measured current I and the steady current I_s. Then, the capacitance C is calculated by using the following equation:

$$C(t) = \frac{1}{V} \int_0^t (I(t) - I_s)\, dt \tag{7.1}$$

Here, we assumed that the charge stored in the prototype was calculated by $C(t)V$ approximately due to the almost zero resistance in series.

The calculation result at the extension per layer of 5.9 μm is shown in Figures 7.3.2 and 7.3.3. The graphs show that capacitance of the prototype increased wit respect to elapsed time after the application of 300 V, which was the reason of the slow reduction of the current flow. In this measurement, the total length of the

prototype was fixed by the measuring instrument. The change of the capacitance, therefore, came from the displacement of the electrode parts such as clinging with each other by pull-in phenomenon.

The power consumption was decreased to about 1 mW after 2-3 s from the application of the voltage, containing a power consumption caused by the steady current (0.1 mW at $d = 5.9[\mu\text{m/layer}]$). The energy consumption at the steady state can be improved by sealing the bear copper along the edge faces.

7.4 Power Consumption in Vacuum

Figure 7.4.1 shows the measured current in the different extension per layer of 0.45 μm, 5.9 μm, 15.0 μm and 24.0 μm in vacuum. The chagne of the current in atmospheric pressure and vacuum had little difference other than the steady current. The steady current at $d = 0.45[\mu\text{m/layer}]$ in vacuum was 0.25 μA higher than that in atmospheric pressure, and at the other extensions, the steady currents were 25-30 nA higher than that in atmospheric pressure. This indicated that the insulation property of air against the creep discharge was excellent as compared to vacuum.

7.5 Concluding Remarks

The power consumption of the prototype showed the existence of the creep discharge, resulting in the energy loss at the steady state. The reason of this discharge came from the bear copper along the edge faces of the electrode films. The current flow in atmospheric pressure and vacuum had no remarkable difference except for increasing the steady current in vacuum.

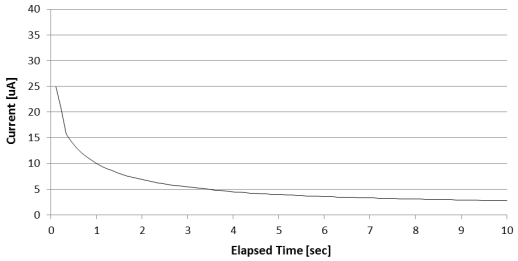

(a) $d = 0.45\mu\mathrm{m/layer}$ (0-10 s)

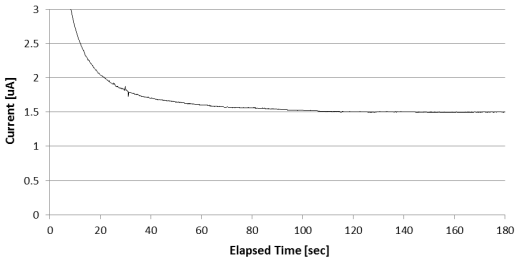

(b) $d = 0.45\mu\mathrm{m/layer}$ (0-180 s)

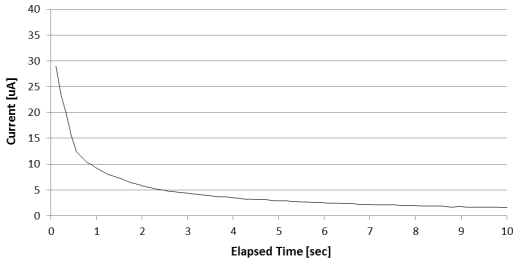

(c) $d = 5.9\mu\mathrm{m/layer}$ (0-10 s)

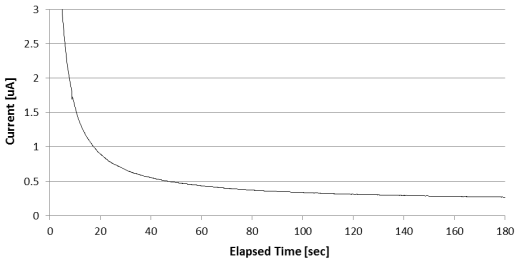

(d) $d = 5.9\mu\mathrm{m/layer}$ (0-180 s)

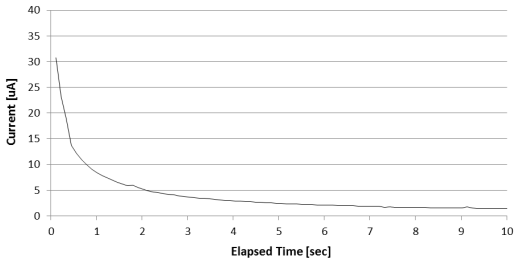

(e) $d = 15.0\mu\mathrm{m/layer}$ (0-10 s)

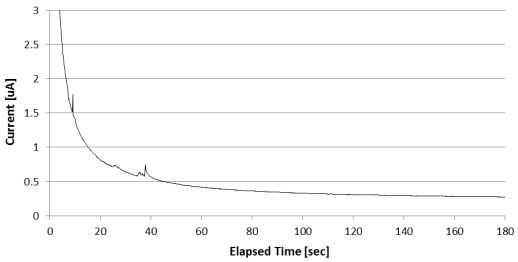

(f) $d = 15.0\mu\mathrm{m/layer}$ (0-180 s)

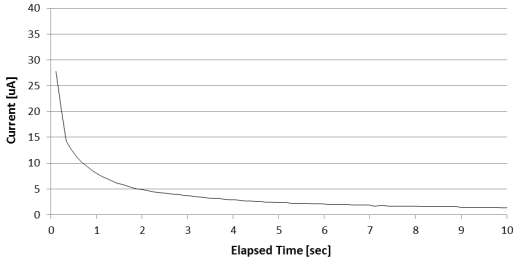

(g) $d = 24.0\mu\mathrm{m/layer}$ (0-10 s)

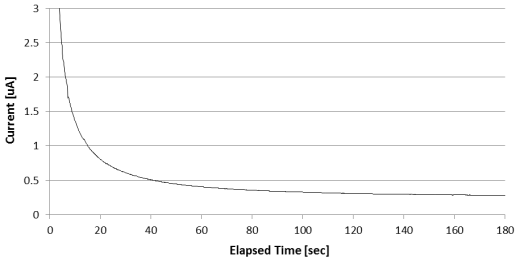

(h) $d = 24.0\mu\mathrm{m/layer}$ (0-180 s)

Figure 7.4.1: Power consumption in the different average gaps between the electrode parts for 10 s starting from the application of 300 V (left graphs) and 180 s (right graphs) in vacuum.

8 Simulation

In this chapter, we will described about a physics engine in order to simulate the performances of the LSEAs both during elongation and contraction. The physics engine is currently under development, therefore we limit to mainly explain the modeling and the calculation method here. We will also show some calculated results, but quantitative evaluation is future work.

8.1 Outline

In chapters on experiments, we obtained some results such as the spring characteristics, the contraction ratio and the generative force. The reasons of the these performance were explained qualitatively by using a deflection model of a cantilever beam or a 50-layered LSEA model. These methods, however, have several drawbacks, e.g. they cannot incorporate the effect of variability of hinge lengths or the constraint of the electrode films due to the clamping plates. Therefore, we attempted to develop a physics engine in order to calculate the performance of the LSEAs quantitatively.

Figure 8.1.1 shows outline of the simulation. First, we set up parameters such

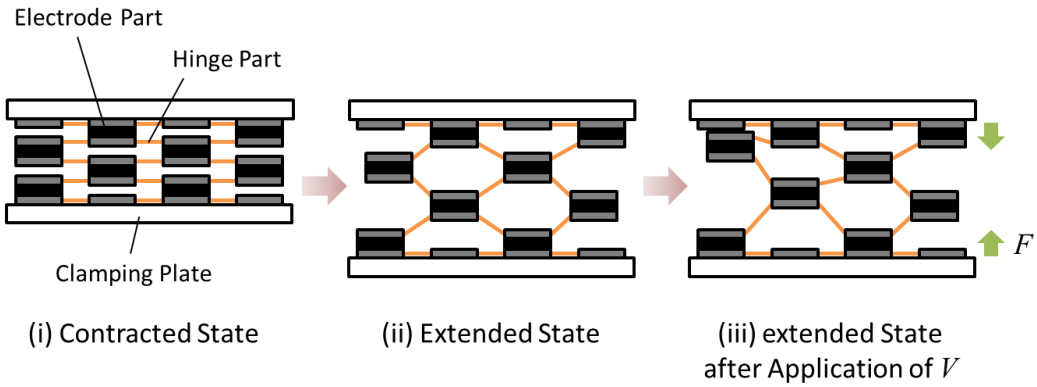

Figure 8.1.1: Outline of the simulation.

as dimensions of the electrodes and the hinges containing their variabilities, mass of the electrode and the clamping plate, and so on (Figure 8.1.1 (i)). Next, the physics engine calculates elongation of the LSEAs by external forces like gravity of the clamping plate or other applied external force (Figure 8.1.1 (ii)). In this calculation, we will find the physics of the LSEAs in the elongation process. The physics of the LSEAs in the contraction process will be also clarified by installing the electrostatic forces between the electrodes (Figure 8.1.1 (iii)). From the next section, the simulated model, the calculated forces and torques and the simulation process are explained.

8.2 Modeling

In general, finite element method (FEM) is often used to solve complex problems containing distortion of materials. FEM seems materials as groups of elements whose form changes are calculated by stress acting on nodes placed at vertexes of the elements. Therefore FEM requires a lot of elements to solve deformation precisely even if the model is not so complex. The method can be applied to elongation and contraction model of LSEAs by using periodic boundary condition if the configurations of the LSEAs are cyclic. Some complex models such as variability of the hinge parts, however, is difficult for FEM to simulate correctly.

To overcome this issue, we attempted to develop a physics engine specialized to solve LSEA models. This engine calculates forces and torques acting on the

electrode parts and solve equation of motion for and rotation around center of gravity of electrode units (detailed later). Here, we explain about the simulation model of the LSEAs.

8.2.1 Electrode Model

In this simulation, electrode parts of the LSEAs are treated as rigid bodies in order to reduce the calculation cost. Actual electrode parts are bendable, but the deflection was slight enough to be negligible because the electrode parts were pulled strongly by tensile forces when the LSEAs actuated, which supported the solutions of the simulation will not change significantly under the hypothesis.

Figure 8.2.1 shows the schematic electrode model (the dotted lines show outline of the hinge parts). Here, an 'electrode' is defined as a partial electrode film bonded with an adjacent electrode, and an 'electrode unit' is defined as a unit of two electrodes and an adhesive block which connects them. The electrode units are arranged as shown in Figure 8.2.2 (the hinge parts are abbreviate). Each electrode part and unit is labeled by the number of the positions. After calculating the applied forces to the electrode units, this simulation calculates the deformation of the LSEAs as motion of and rotation around the center of gravity of the electrode units. The mass of a electrode unit is 0.188 [mg] which contains the mass of the surrounding hinges, i.e. the motion of the hinges themselves is not considered. In addition, the adhesive is also treated as rigid bodies.

The dimensions of the simulated model is as follows (see 8.2.1). The average width of the electrodes is 2 [mm], the average length of the hinges is 0.2 [mm], the

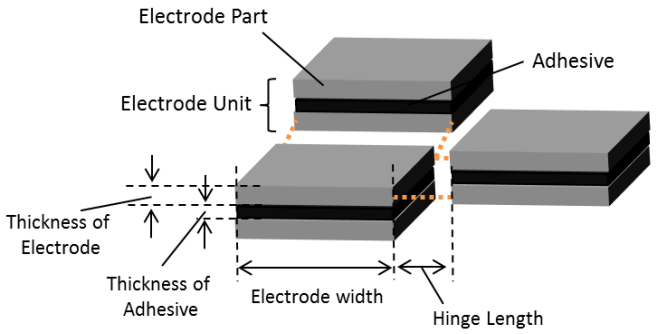

Figure 8.2.1: Schematic of electrode parts and electrode units with the part names.

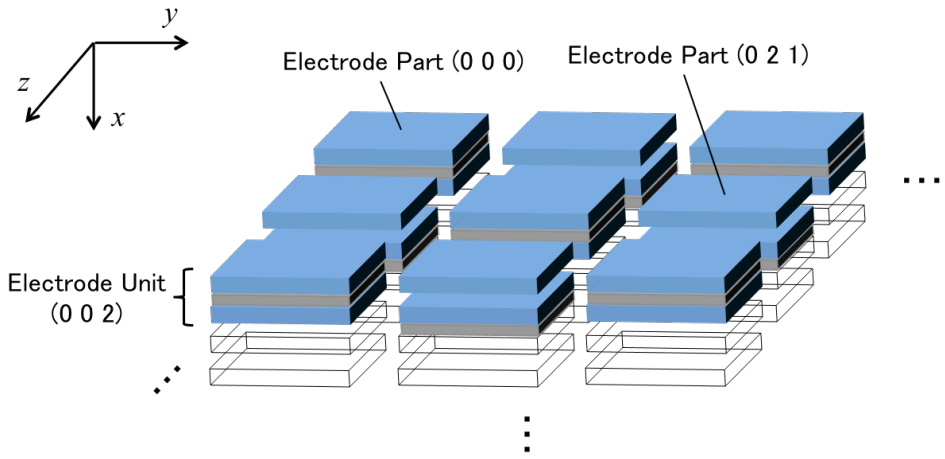

Figure 8.2.2: Arranged electrode units.

electrode thickness is 8.6 [μm], the adhesive thickness is 4.2 [μm], and the thickness of the clamping plate is 2 [mm]. Changing the widths of the electrodes and the hinge lengths enable to simulate the variability or the change of the positions of the adhesive.

8.2.2 Hinge Model

Calculation model of a cantilever beam can be applied to some simple deformation of hinge parts as calculated previously. On the other hand, calculation of the hinge parts is complex in practice e.g. stretch or torsion of the hinge lengths, which makes the analytical calculation difficult. Therefore, approximate model should be needed.

Let us consider some of the deformation of the hinge parts as shown in Figure 8.2.3. Arrows in this figure represent the direction of forces acting on the electrode units. This examples shows that the hinge parts generate a force to restore the shape. The force generated in the longitudinal direction mainly comes from the tensile stress of the hinge materials (see Figure 8.2.3 (a) and (b)). This force is calculated by using a linear spring. The reactive force due to bending of the hinge parts acts mainly at the connecting point with the electrode units where the bending moment is larger than that at the center of the hinges (see Figure 8.2.3 (c)-(e)). This force can be expressed approximately by using a torsion spring

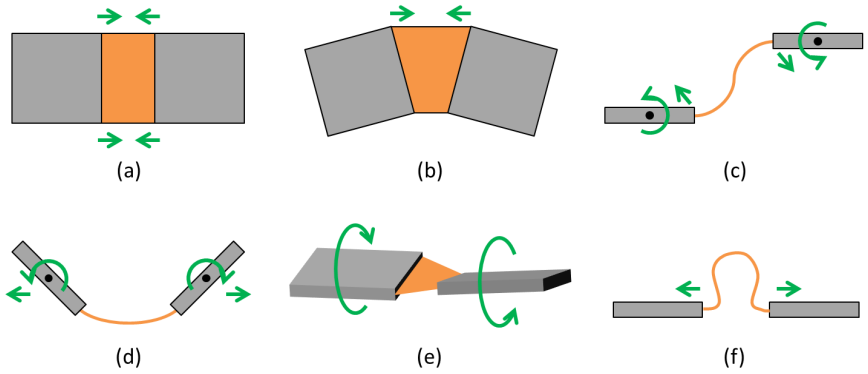

Figure 8.2.3: A variety of deformed hinges and the forces acting on the electrode parts at the time.

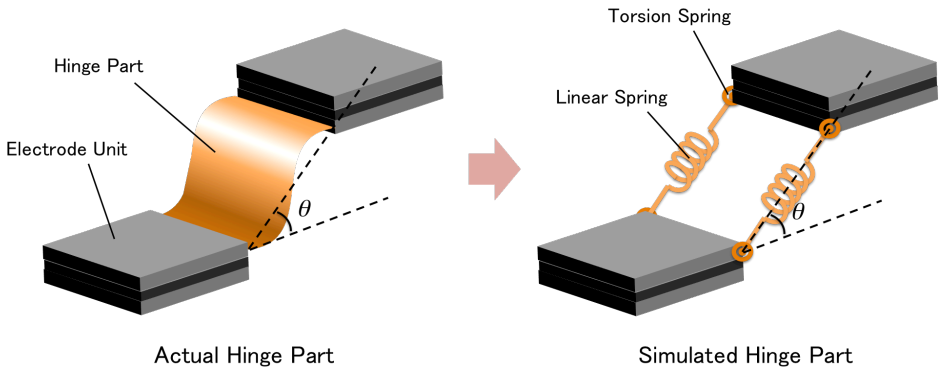

Figure 8.2.4: Schematic of the actual hinge parts (left) and the simulated hinge model (right).

whose force is calculated by the angle between the electrode and the hinge. The deformation in Figure 8.2.3 (f) is an exception, however, the force is also expressed approximately by a linear spring having a different spring constant in the case of elongation.

From the above discussion, we builded up an approximate model of the hinge parts as shown in Figure 8.2.4. The hinge part is placed by two linear springs and four torsion springs as follows.

Linear Spring: Linear springs are connected at corners of the adjacent electrodes. The natural lengths are the hinge lengths. The springs have two different spring constants for elongation (k_{elong}) and contraction (k_{contr}). The spring constant k_{elong} is determined by the tensile stress of the hinge materials.

Torsion Spring: Torsion springs are placed at each corner of the electrodes. The torque is expressed as a product of the spring coefficient K and the angle θ between the electrode and the hinge. The coefficient K is calculated from deflection of a cantilever beam.

8.2.3 Force and Torque

In this section, we describe the forces and torques acting on the electrode units in this simulation. Figure 8.2.5 shows gravity and a force and a torque generated by the deformation of a hinge part. Besides them, electrostatic force, air drag and collision force also act on the electrode units.

Gravity

Gravity $\boldsymbol{F}_{\text{grav}}$ acts on the electrode units. Let the mass of the electrode unit is m and acceleration of gravity is $\boldsymbol{g}$, then

$$\boldsymbol{F}_{\text{grav}} = m\boldsymbol{g}. \tag{8.1}$$

The acceleration of gravity $\boldsymbol{g}$ is pointed to the positive sense of the x-axis direction in Figure 8.2.2 in this simulation.

Elastic Force

Elastic force generated by deformation of the hinges is a sum of elastic forces of the linear springs and the torsion springs. Elastic force $\boldsymbol{F}_{\text{lin}}$ generated from the

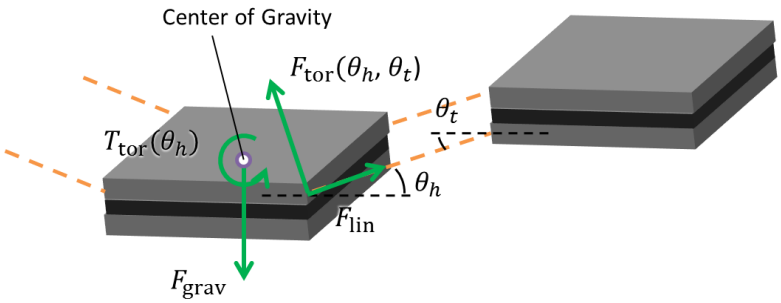

Figure 8.2.5: Gravity of the electrode unit, and a force and a torque resulting from the elasticity of a hinge part.

linear spring is expressed as follows:

$$\boldsymbol{F}_{\mathrm{lin}}(l) \;=\; k(l)(l - l_{\mathrm{init}}) \cdot \hat{\boldsymbol{r}}_l, \tag{8.2}$$

where l is a hinge length calculated as the distance between the corner points of the facing electrode units, l_{init} is the initial hinge length and $\hat{\boldsymbol{r}}_l$ is a unit vector on a line jointing the corner points (let the positive sense is as the direction of the arrow $\boldsymbol{F}_{\mathrm{lin}}$ in Figure 8.2.5). The spring rate k switches depending on the hinge length l:

$$k(l) = \begin{cases} k_{\mathrm{elong}}, & \text{when } l > l_{\mathrm{init}} \\ k_{\mathrm{contr}}, & \text{when } l \leq l_{\mathrm{init}} \end{cases} . \tag{8.3}$$

Each spring constant is defined as $k_{\mathrm{elong}} = 178$ [kN/m] and $k_{\mathrm{contra}} = 0$ [N/m] in this simulation. The spring constant k_{elong} is determined from Young's modulus of PET, 4.15 GPa, and thickness of the hinge part.

Effect of the elasticity of the torsion springs is considered as shown in Figure 8.2.6. Let us consider the equilibrium of force and torque acting on a hinge part. When the hinge part is bended by the electrode units, bending moments act on the end points of the hinge part. The moment can be expressed approximately by the torques generated by the torsion springs $K\theta_1$ and $K\theta_2$. Here, θ_1 and θ_2 are angles between the electrode units and the hinge (see Figure 8.2.6). If the torques are different, forces F_1 and F_2 are needed not to rotate the hinge. From simple calculation of equilibrium of the torques, the forces F_1 and F_2 are obtained as follows:

$$F_1 = F_2 = \frac{K|\theta_1 - \theta_2|}{l}. \tag{8.4}$$

The force (torque) acting on the electrode units is obtained as the reaction force (torque), i.e. the effect of the torsion springs is expressed by following force $\boldsymbol{F}_{\mathrm{for}}$ and torque $\boldsymbol{T}_{\mathrm{tor}}$:

$$\boldsymbol{F}_{\mathrm{tor}}(\theta_h, \theta_t) \;=\; \frac{|K(\theta_h)\theta_h - K(\theta_t)\theta_t|}{l} \cdot \hat{\boldsymbol{r}}_{\mathrm{tor,f}} \tag{8.5}$$

$$\boldsymbol{T}_{\mathrm{tor}}(\theta_h) \;=\; K(\theta_h)\frac{I\theta_h}{I - md_{\mathrm{cc}}^2} \cdot \hat{\boldsymbol{r}}_{\mathrm{tor,t}} \tag{8.6}$$

where θ_h and θ_t denote angles between the hinge part and the objective electrode units (see Figure 8.2.5), l is a distance between the corner points between the

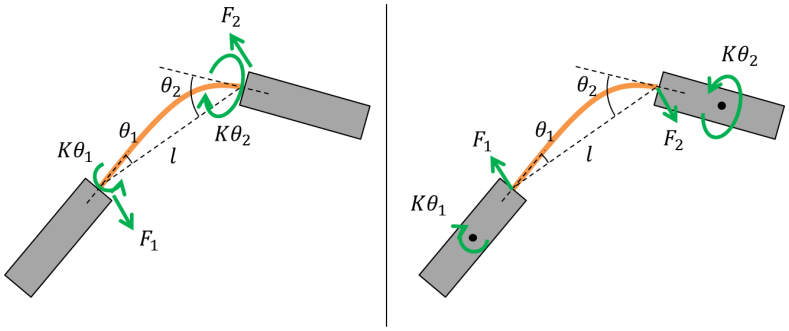

Figure 8.2.6: Force and torque acting on the hinge part (left) and force and torque acting on the electrode units (right).

objective electrode unit and the adjacent electrode unit, I is the moment of inertia of the electrode units, d_{cc} is a projected distance between the center of gravity of the objective electrode unit and the corner of the objective electrode unit on the side face of the objective electrode unit. $\hat{\boldsymbol{r}}_{\mathrm{tor,f}}$ represents a unit vector pointing to the direction which prevents the hinge from rotating, and $\hat{\boldsymbol{r}}_{\mathrm{tor,t}}$ represents a unit vector pointing to a direction normal to the side face of the objective electrode unit. The sense is a direction to reduce θ. The spring rate K is calculated by deflection of a cantilever beam simulated the hinge parts of the half length. For example, when the Young's modulus of PET film is 540 MPa,

$$K(\theta) = \sum_{i=0}^{5} a_i |\theta|^i \quad [\mathrm{mNmm/rad}], \tag{8.7}$$

here,

$$\begin{aligned} a_5 = 3.41, \quad a_4 = -9.82, \quad a_3 = 10.4 \\ a_2 = -4.67, \quad a = 1 = 0.908, \quad a_0 = 0.637. \end{aligned} \tag{8.8}$$

Electrostatic Force

Let the distances between the corners of the objective electrode unit and the facing electrode unit are d_1, d_2, d_3, d_4 respectively (see Figure 8.2.7). If all of the distances are the same, the electrostatic force between the electrode units is described by

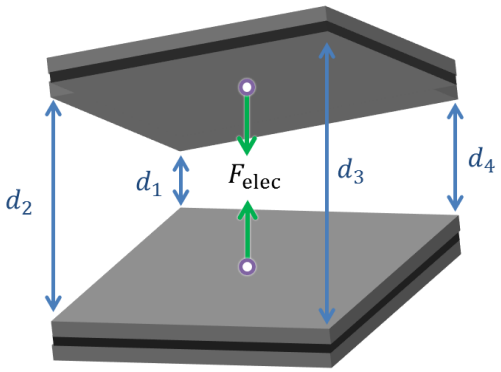

Figure 8.2.7: Electrostatic force and the distances d_i $(i = 1, 2, 3, 4)$ between the corners of the electrode units.

the same formula as Equation (3.1):

$$F_{\text{elec}}(d_1) = \frac{1}{2}\frac{\varepsilon_0 S V^2}{\varepsilon_2 \left(\frac{t}{\varepsilon_1} + \frac{d_1}{\varepsilon_2}\right)^2}. \tag{8.9}$$

In this simulation, $\varepsilon_0 = 8.854 \times 10^{-12}$ [F/m], $\varepsilon_1 = 3$ and $\varepsilon_2 = 1.00059$. In the situation when the electrode areas are different, average area between the two electrode units are used as S. If $d_1 = d_4$ and $d_2 = d_3$, the electrostatic force is described as a following equation:

$$F_{\text{elec}}(d_1, d_2) = \frac{1}{2}\frac{\varepsilon_0 S V^2}{\varepsilon_2 \left(\frac{t}{\varepsilon_1} + \frac{d_1}{\varepsilon_2}\right)\left(\frac{t}{\varepsilon_1} + \frac{d_2}{\varepsilon_2}\right)}. \tag{8.10}$$

In a similar way, If all of the distances are different, the electrostatic force is expressed as follows:

$$F_{\text{elec}}(d_1, d_2, d_3, d_4) = \frac{1}{2}\frac{\varepsilon_2 \varepsilon_0 S V^2}{(d_2 - d_1)(d_3 - d_1)} \ln \frac{\left(\frac{t}{\varepsilon_1} + \frac{d_3}{\varepsilon_2}\right)\left(\frac{t}{\varepsilon_1} + \frac{d_2}{\varepsilon_2}\right)}{\left(\frac{t}{\varepsilon_1} + \frac{d_1}{\varepsilon_2}\right)\left(\frac{t}{\varepsilon_1} + \frac{d_4}{\varepsilon_2}\right)}. \tag{8.11}$$

The direction of the electrostatic force is a direction from the center of gravity of the objective electrode unit to that of the facing electrode unit.

Air Drag

As the air drag, inertial resistance are used in this simulation.

$$\boldsymbol{F}_{\text{air}} = -C_{\text{air}}|\boldsymbol{v}|^2 \cdot \hat{\boldsymbol{r}}_v \tag{8.12}$$

$$\boldsymbol{T}_{\text{air}} = -C'_{\text{air}}|\boldsymbol{\omega}|^2 \cdot \hat{\boldsymbol{r}}_\omega, \tag{8.13}$$

where, C_{air} is a coefficient, $\boldsymbol{v}$ is the velocity of the electrode unit, $\boldsymbol{\omega}$ is the rotational velocity of the electrode unit, $\hat{\boldsymbol{r}}_v$ represents a unit vector pointed to positive sense of the direction of $\boldsymbol{v}$, and $\hat{\boldsymbol{r}}_\omega$ represents a unit vector pointed to positive sense of the direction of $\boldsymbol{\omega}$. In this simulation, C_{air} and C'_{air} was 0.001 $[\text{mN} \cdot \text{s}^2/\text{m}^2]$ and 0.001 $[\text{mN} \cdot \text{s}^2/\text{rad}^2]$ respectively.

Calculation of Collision

Collision force is added at the contact points. The method of the collision detection is as follows. let $\boldsymbol{a}$, $\boldsymbol{b}$, $\boldsymbol{c}$, $\boldsymbol{d}$ are position vectors pointed to the positions of the corners of the objective electrode unit respectively. In the same manner, let $\boldsymbol{e}$, $\boldsymbol{f}$, $\boldsymbol{g}$, $\boldsymbol{h}$ are position vectors pointed to the positions of the corners of the facing electrode unit respectively. Here, we assume that the objective electrode unit is placed under (or has a larger x than) the facing electrode unit in the initial condition. The equation of the plane $ABCD$ is described using a normal vector $\boldsymbol{n}$ of the plane as follows:

$$\boldsymbol{n} \cdot (\boldsymbol{x} - \boldsymbol{a}) = 0. \tag{8.14}$$

Then, if at least one of the corner positions $\boldsymbol{p}$ ($\boldsymbol{p} = \boldsymbol{e}, \boldsymbol{f}, \boldsymbol{g}, \boldsymbol{h}$) satisfies the following inequality:

$$p_x > a_x - \frac{n_y}{n_x}(p_y - a_y) - \frac{n_z}{n_x}(p_z - a_z), \tag{8.15}$$

the corner point $\boldsymbol{p}$ is located under the plane $ABCD$. In the same manner, if any of the corner positions $\boldsymbol{q}$ ($\boldsymbol{q} = \boldsymbol{a}, \boldsymbol{b}, \boldsymbol{c}, \boldsymbol{d}$) satisfy the following inequality:

$$q_x < e_x - \frac{n'_y}{n'_x}(q_y - e_y) - \frac{n'_z}{n'_x}(q_z - e_z), \tag{8.16}$$

these electrode units are contacted. Here, $\boldsymbol{n}'$ is a normal vector of the plane $EFGH$.

Because calculation of the collision force is difficult, the following small force

added at the contact points repeatedly until velocity vectors $\boldsymbol{v}_{\mathrm{col}}$ of the contact points point to the direction to separate the electrode units:

$$\boldsymbol{f}_{\mathrm{col}} \;=\; (\alpha|\boldsymbol{v}_{\mathrm{col}}| + \beta) \cdot \hat{\boldsymbol{r}}_{\mathrm{col}}, \tag{8.17}$$

where, α and β are coefficients, and $\hat{\boldsymbol{r}}_{\mathrm{col}}$ is a unit vector pointed to the direction normal to the contact surface. In this simulation, we set $\alpha = 1 \times 10^{-6}$ [mN $\cdot$ s/m] and $\beta = 1 \times 10^{-4}$ [mN].

Calculation of Force and Torque

Total force $\boldsymbol{F}_{\mathrm{tot}}$ acting on the electrode unit is calculated as follows:

$$\boldsymbol{F}_{\mathrm{tot}} = \boldsymbol{F}_{\mathrm{grav}} + \sum_i (\boldsymbol{F}_{\mathrm{lin},i} + \boldsymbol{F}_{\mathrm{tor},i}) + \boldsymbol{F}_{\mathrm{elec}} + \boldsymbol{F}_{\mathrm{air}} + \sum_j m_j \boldsymbol{f}_{\mathrm{col}}. \tag{8.18}$$

where, i represents the number of the springs constituting the hinge part, j represents the number of the contact points and m_j represents the number of addition of $\boldsymbol{f}_{\mathrm{col}}$ at the contact point j. In the same way, total torque $\boldsymbol{T}_{\mathrm{tot}}$ is calculated from the following formula:

$$\boldsymbol{T}_{\mathrm{tot}} = \sum_i \{\boldsymbol{r}_{\mathrm{corner},i} \times (\boldsymbol{F}_{\mathrm{lin},i} + \boldsymbol{F}_{\mathrm{tor},i}) + \boldsymbol{T}_{\mathrm{tor},i}\} + \boldsymbol{T}_{\mathrm{air}} + \sum_j \boldsymbol{r}_{\mathrm{col},j} \times (m_j \boldsymbol{f}_{\mathrm{col}}), \tag{8.19}$$

where, $\boldsymbol{r}_{\mathrm{corner},i}$ represents position of the point of application of $\boldsymbol{F}_{\mathrm{lin},i}$ and $\boldsymbol{F}_{\mathrm{tor},i}$ from the center of gravity, and $\boldsymbol{r}_{\mathrm{col},j}$ represents position of the contact point j from the center of gravity.

8.3 Simulation Method

Figure 8.3.1 shows the calculation flow of the physics engine. Each step is detailed below.

Initialize: In this step, the physics engine loads data regarding the dimensions and mass of the electrode parts and the hinge parts, values of the coefficients and calculation time step dt.

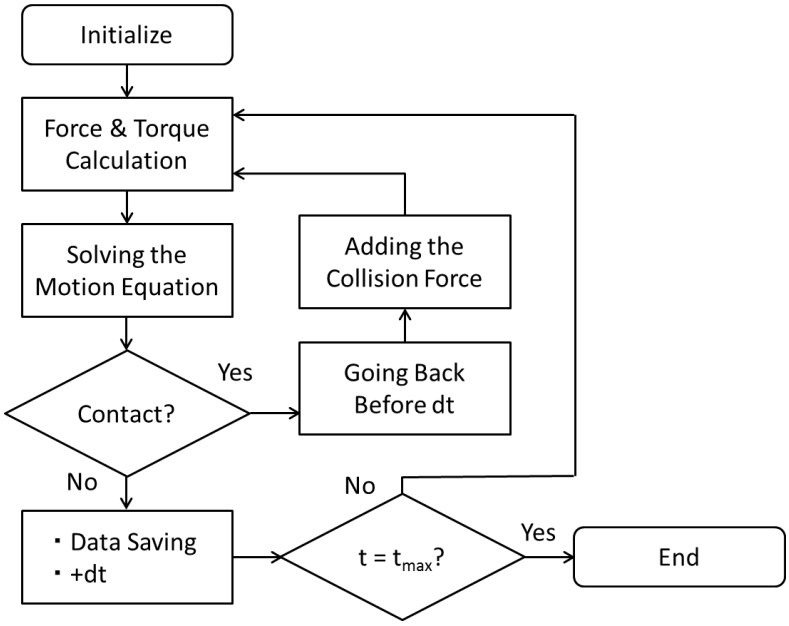

Figure 8.3.1: Flow chart of the physics engine.

Force and Torque Calculation: The physics engine calculates the forces $\boldsymbol{F}_{\mathrm{tot}}$ and torques $\boldsymbol{T}_{\mathrm{tot}}$ acting on the electrode units from the positions (see Equations (8.18) and (8.19)).

Solving the Motion Equation: The engine calculates the motion of the electrode units by using $\boldsymbol{F}_{\mathrm{tot}}$ and $\boldsymbol{T}_{\mathrm{tot}}$ and determines the position, velocity and acceleration of the electrode units after the time step dt. The accelerations $\boldsymbol{\alpha}$ of the center of gravity of the electrode units are determined by Newton's equation:

$$m\boldsymbol{\alpha} = \boldsymbol{F}_{\mathrm{tot}}. \tag{8.20}$$

The rotational accelerations $\dot{\boldsymbol{\omega}}$ around the center of gravity of the electrode units are calculated by the following equation:

$$\mathbf{I}\dot{\boldsymbol{\omega}} + \boldsymbol{\omega} \times \mathbf{I}\boldsymbol{\omega} = \boldsymbol{T}_{\mathrm{tot}}. \tag{8.21}$$

Besides, the bottom electrode units are attached to the clamping plate. Their motion is calculated as the motion of a compound of the electrode units and the clamping plate.

Collision Detection: After solving the equation of motion, the engine looks for

the contact points by using Inequalities (8.15) and (8.16). If any contact points are found, the engine substitutes data before dt to the current data, adds collision force $\boldsymbol{f}_{\mathrm{col}}$ at the contact points and recalculates the equation of motion. This loop is repeated until the velocity vectors $\boldsymbol{v}_{\mathrm{col}}$ of the contact points point to the direction to separate the electrode units.

Data Saving / +dt: If no collision is detected, the calculated data is saved and the simulation goes to the next time until the elapsed time reaches the upper limit $t_{\max}$.

8.4 Examples of the Simulation

In this section, some examples of the simulation results are shown. The physics engine is currently under development, therefore, the results are just for reference.

8.4.1 Elongation

Elongation of a 6-layered 3×1 LSEA was simulated with a load of 1 g in both cases with/without variability. The variability of the hinge lengths are given by variability of width of the adhesive. It should be noted that the electrode areas are also changed in this situation. The variability randomized according to a normal distribution of the standard deviation of the 20 % average hinge length.

Figure 8.4.1 shows the elongation simulation of the LSEA without variability. Each square represents the electrode unit. In this figure, the top electrodes are fixed and the load is attached to the bottom electrodes (the bottom clamping plate). As is shown in this figure, the air gaps are almost uniform except for that close to the top and bottom clamping plates. On the other hand, Figure 8.4.2 is simulation result of the LSEA with variability, indicating that the air gaps are distributed randomly. Some left electrode units were crossed because the number of loops for collision was limited by 1000 in order to reduce the calculation time and collision force was not sufficiently large in this simulation.

Elongation simulation was succeeded for a 11-layered 7×7 LSEA (no variability model) with a load of 10 g as well as the 3×1 LSEA (Figure 8.4.3).

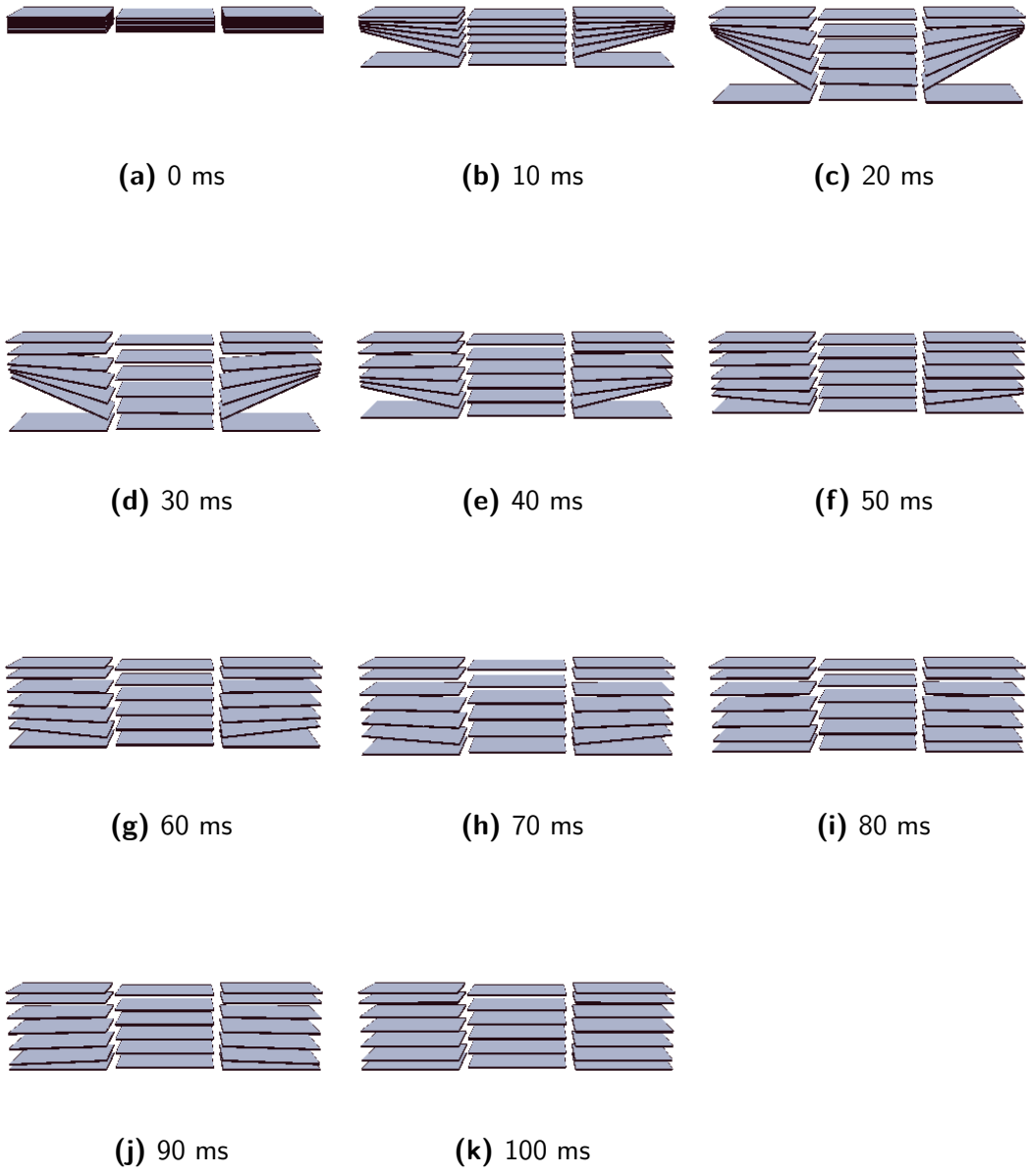

(a) 0 ms **(b)** 10 ms **(c)** 20 ms

(d) 30 ms **(e)** 40 ms **(f)** 50 ms

(g) 60 ms **(h)** 70 ms **(i)** 80 ms

(j) 90 ms **(k)** 100 ms

Figure 8.4.1: Elongation simulation of a 6-layered 3×1 LSEA with a load of 1 g. The time represents the elapsed time. The scale of elongation direction is doubled.

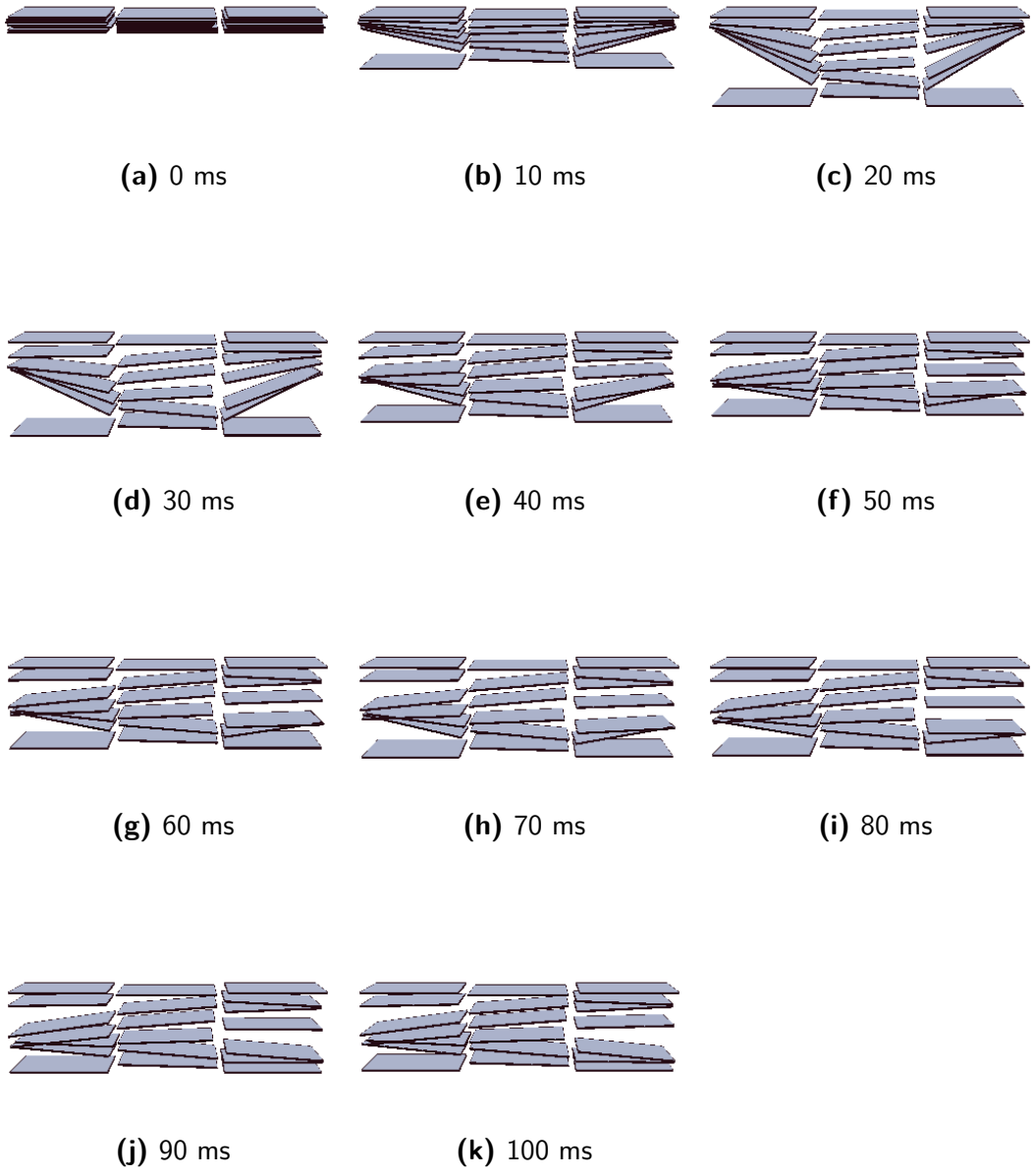

(a) 0 ms **(b)** 10 ms **(c)** 20 ms

(d) 30 ms **(e)** 40 ms **(f)** 50 ms

(g) 60 ms **(h)** 70 ms **(i)** 80 ms

(j) 90 ms **(k)** 100 ms

Figure 8.4.2: Elongation simulation of a 6-layered 3×1 LSEA having 20 % variability of the hinge length with a load of 1 g. The scale of elongation direction is doubled.

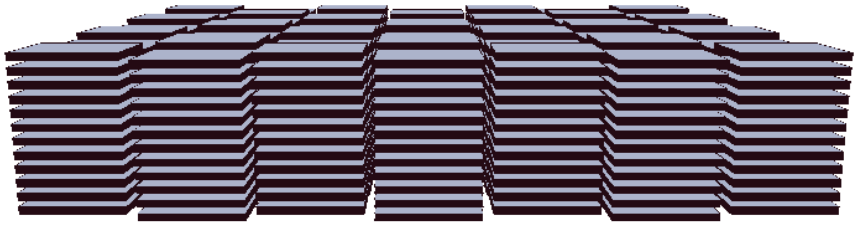

(a) 0 ms

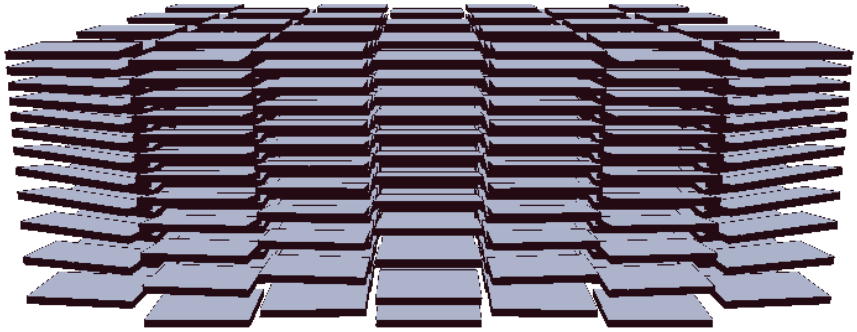

(b) 10 ms

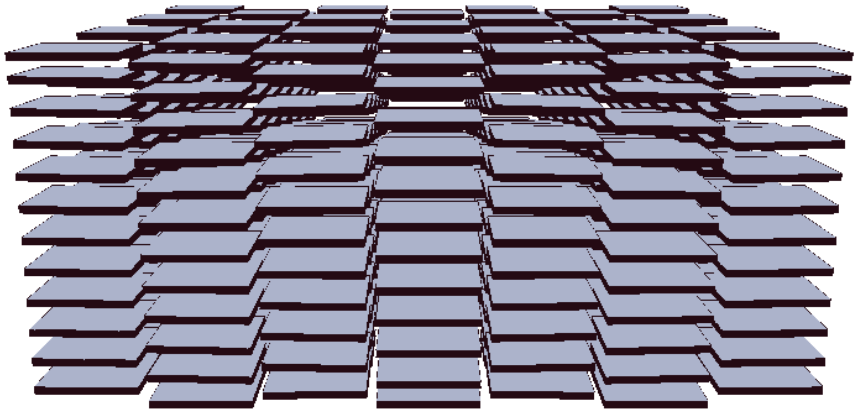

(c) 30 ms

Figure 8.4.3: Elongation simulation of a 11-layered 7×7 LSEA with a load of 10 g. The time represents the elapsed time. The scale of elongation direction is decupled.

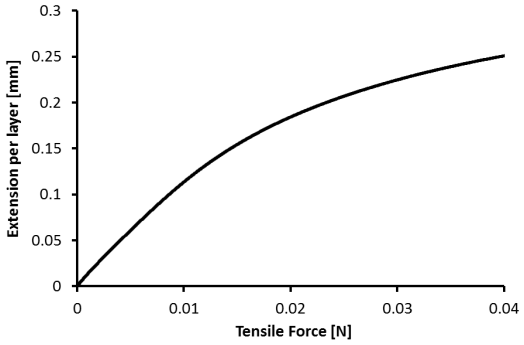

(a) 3×1 LSEA

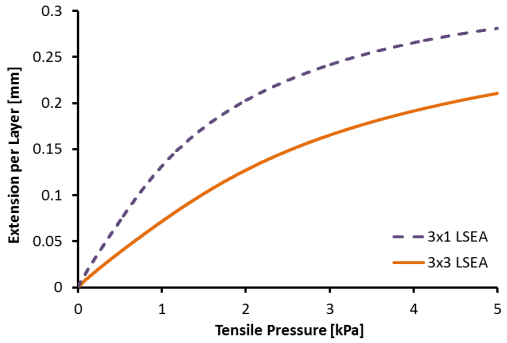

(b) Comparison between a 3×1 LSEA and a 3×3 LSEA

Figure 8.4.4: Calculated spring characteristics of a 6-layered LSEA without variability.

8.4.2 Spring Characteristics

Spring characteristics can be calculated from the force acting on the clamping plate and the extension of the LSEA at the time. Figure 8.4.4a is a calculated spring characteristics of a 6-layered 3×1 LSEA without variability of the hinge parts. In this simulation, the bottom clamping plate was displaced mandatorily with the velocity of 2 mm/s. This characteristics re-created the result of deflection of a cantilever beam in Figure 3.2.3 well. In this simulation, the number of the hinge parts was four per layer (two units of two hinges connected in series are connected in parallel), therefore, the value in horizontal axis in the graph double and that in vertical axis quadruple in comparison with the graph in Figure 3.2.3.

In the same way, spring characteristics of a 6-layered 3×3 LSEA are calculated. Figure 8.4.4b shows the extension per layer between the 3×1 LSEA and the 3×3 LSEA under appled tensile pressures. This implies that the 3×3 LSEA are stiffer than the 3×1 LSEA because of the transverse force as well as the measurement result of the spring characteristics of Prototype A.

8.4.3 Contraction Ratio

Contraction of a 6-layered 3×1 LSEA was simulated with a load of 0.1 g at 100 V as well as the elongation simulation. Figure 8.4.5 shows the contraction simulation of the LSEA. As is shown in this figure, the electrode units moved by pull-in

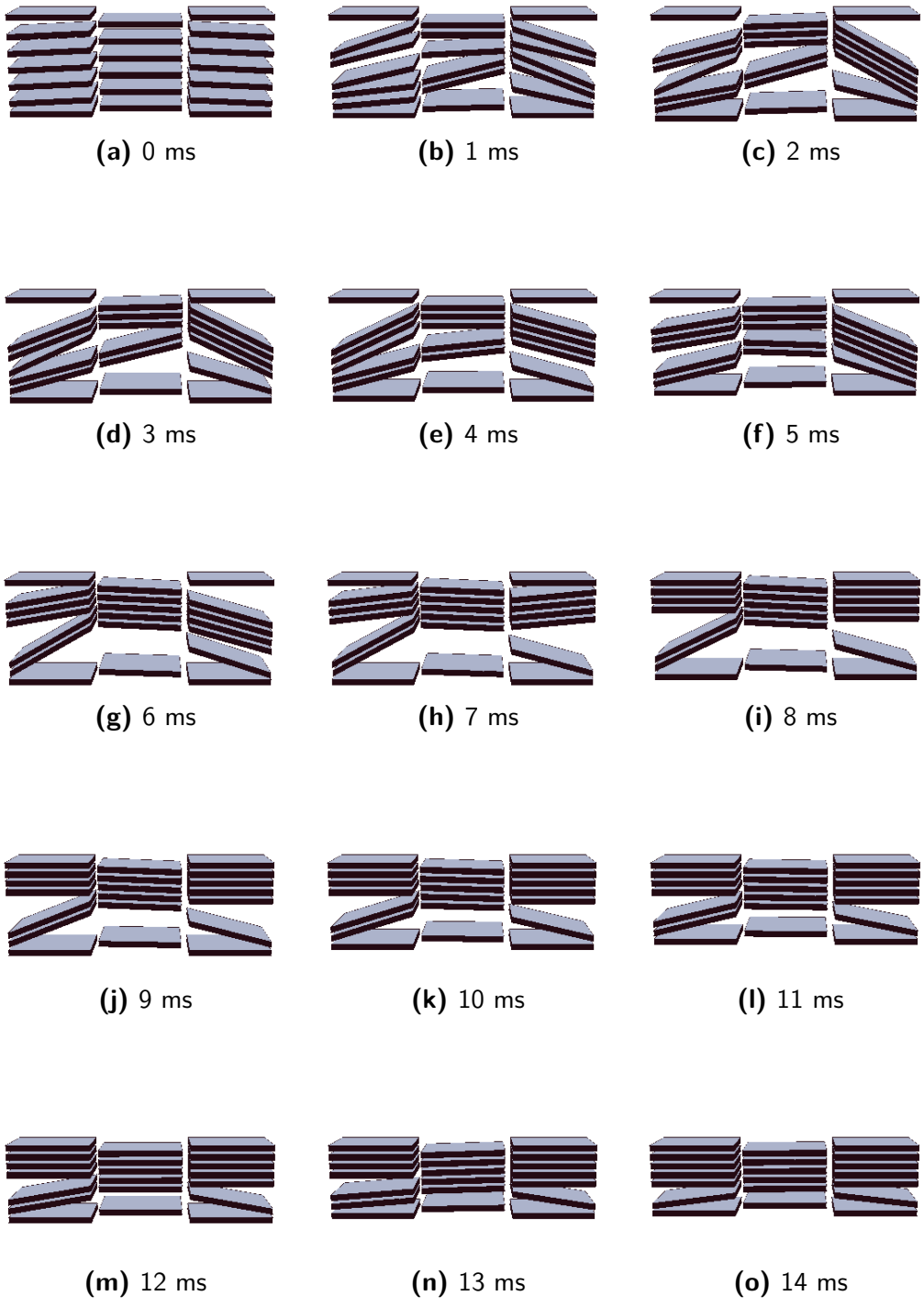

(a) 0 ms **(b)** 1 ms **(c)** 2 ms

(d) 3 ms **(e)** 4 ms **(f)** 5 ms

(g) 6 ms **(h)** 7 ms **(i)** 8 ms

(j) 9 ms **(k)** 10 ms **(l)** 11 ms

(m) 12 ms **(n)** 13 ms **(o)** 14 ms

Figure 8.4.5: Contraction simulation of a 6-layered 3×1 LSEA with a load of 0.1 g at 100 V. The time represents the elapsed time. The scale of elongation direction is decupled.

phenomenon before contraction of the LSEA, sustaining the discussion of the generative force in Section 6.3. The contraction ratio was 34.4 %. In the contraction simulation, we added a term proportional to the square of the applied voltage to the collision force $\boldsymbol{f}_{\mathrm{col}}$ in order to shorten the calculation time.

8.5 Concluding Remarks

Fundamental concept of a physics engine was proposed as a method to simulate the performance of LSEAs. The physics engine simulate the motion of LSEAs by calculating equation of the motion of the electrode units. In order to reduce the calculation cost, the electrode parts were seemed as rigid bodies and the hinge parts were seemed as compounds of linear springs and torsion springs. The result example of calculation of spring characteristics (Figure 8.4.4a) showed that the spring model of the hinge parts can simulate the complex deformation of actual hinge parts successfully in the case of a 6-layered 3×1 LSEA model.

As the future work, we have to improve the calculation process of collision. In order to shorten the calculation time, the number of loops for collision was limited by 1000 in this simulation, resulting in insufficient collision force in some case e.g. crossed electrode units in Figure 8.4.2.

9 Conclusion

9.1 Summary

In this study, we proposed a innovative electrostatic actuator for use as artificial muscles of robots in macro scale. The actuator, called a Large-scale Stacked-type Electrostatic Actuator (LSEA), is a multiply-layered actuator consisting of thin and flexible three-layered (insulator - conductor - insulator) films of the specific gravity of about one, resulting in the light weight and flexibility like a biological muscle. The LSEA contracts in the stacking direction linearly by a application of a voltage between the electrode films. Due to the unique bonding pattern, this actuator has a lot of electrode parts (acting as parallel electrode plates) connected with each other by hinge parts (acting as flexible hinges). The gaps between the electrode parts narrow easily in activation and are hard to widen beyond necessity in deactivation because of the spring characteristics of the hinge parts.

The LSEA has an advantage in the easy fabrication even when the electrode area is large, i.e., the fabrication process is only making laminated films (also commercially available) and cutting, etching and stacking them. The stroke length

can be increased by stacking a lot of electrode films and the force density can be increased by shortening the hinge length. Therefore an LSEA can achieve a high output at a small size. Changing the area and the configuration of the electrode films makes it possible to fabricate large-area LSEAs having different shapes. It indicates that an LSEA can achieve an output as high or higher than that of biological muscles even at a large scale, also having high power-weight ratio.

In the experiment, the performances of two prototypes, such as a five-layered LSEA (Prototype A) and fifty-layered LSEA with external stoppers (Prototype B), were investigated.

Spring characteristics: The measurement of the spring characteristics proved experimentally that LSEAs have proper spring characteristics for use as artificial muscles, i.e. the hinge parts having two soft and hard range prevent overextension of the electrode intervals. For Prototype A, the spring constants were 38 kN/m per layer in the soft range and 138 kN/m per layer in the hard range. Their ratio was 3.6. The spring characteristics were due to the configuration of the hinge parts and the effect of the transverse force acting on the hinge parts.

The spring constant changed with respect to the degree of vacuum almost linearly. The calculation of the deflection of the hinge parts indicated that the binder layer expanded 0.16 μm (about 3 % of the thickness) per sheet of the electrode films in vacuum as compared to that in atmospheric pressure. The effect of air drag was appeared prominently when the prototype elongated from the completely contracted range to the soft range due to the short gap between the electrodes less than 3 μm.

Contraction ratio: The measurement of the contraction ratio revealed that LSEAs had the high contraction ratio either equaling or surpassing the contraction strain of biological muscles. For Prototype B, the contraction ratio was -28.8 % at a load of 0.85 N at 300 V. The contraction ratio of the prototype decreased even at a light load (0.12 N) due to the stiffness of the hinges in the soft range. The hinges also stiffened in vacuum because expansion of the binder increased the second moment of area of the hinges, resulting in the high flexural rigidity. The actuation energy density was 0.25 J/kg at a load of 0.85 N at 300 V for Prototype B which was about hundredth of that of muscles because the electrostatic force

was not sufficiently high. The comparison of the storage condition indicated that the actuation performance changed due to the plastic deformation or peeling of the adhesive.

Responsiveness: The responsiveness of the prototype was slow and easily changed with the applied load due to inertia of the load, that is, sufficiently high electrostatic force will improve the responsiveness. The comparison of the responsiveness in atmospheric pressure and vacuum showed that the effect of air drag was not dominant and it slightly appeared only when the average gap between the electrodes was less than 3 μm for Prototype B.

Generative force: The generative force of Prototype B was smaller at the narrow electrode intervals than the electrostatic force calculated by using the average electrode interval because the actual behavior of the prototype should have been expressed by pull-in model. However, the generative force exceeded the calculated electrostatic when the prototype elongated to some extent. The precise solution has not been obtained yet, but this indicates that more air gaps pulled in than calculated numbers because of the dynamic pull-in phenomenon or the variability of the gap lengths and the spring constants.

The decreasing of the generative force with respect to the degree of vacuum seems to come from difference of the charging condition between atmospheric condition and vacuum condition. The charge distribution on the surface of the electroe films seems to contribute to the reduction of the contraction ratio in vacuum too.

In addition, we found a phenomenon of the significant increment of the generative force at high vacuum as compared to that at a low degree of vacuum when the elapsed time after application of a voltage was short, but the reason is not clear yet.

Power consumption: The power consumption of Prototype B was around 1mW at first and stayed at sub-milliwatt, showing the existence of the creep discharge. This resulted in the energy loss at the steady state. The reason of this discharge could come from the bear copper along the edge faces of the electrode films. The current flow in atmospheric pressure and vacuum had no remarkable difference except for increasing the steady current in vacuum.

As an additional study, fundamental concept of a physics engine was proposed as

a method to simulate the performance of LSEAs. The hinge parts were considered as compounds of linear springs and torsion springs in order to simplify the hinge model. The result example of calculation of spring characteristics showed the adequacy of the spring hinge model in the case of a 6-layered 3×1 LSEA model.

9.2 Future Work

The performance measurement of the prototypes revealed some improvements described below:

Adhesive: The adhesion force between the bonded electrode parts should be more forceful to improve reproducibility of the contraction ratio and achieve durable LSEAs regardless of the storage condition.

Hinge: The hinge parts should be thin and short (but tough and hard-breakdown) to achieve a high force density, resulting in a high energy density and responsiveness for LSEAs.

Bonding of plastic materials is generally difficult for adhesives because of the inactive surface. Some activation treatments such as plasma processing or UV-ozone processing are effective to improve adhesion force. However, the adhesive in the prototypes peeled from the electrode films despite the UV-ozone processing. Therefore, we should try other methods to improve the bonding force such as a application of molecular binding technique. The method enables to link plastic materials with each other by covalent bonds which connect atoms strongly.

As the other challenges, a mechanism for the force generation in a high vacuum should be interpreted. This also seems to be strongly linked to the process of changing the generative force with respect to the elapsed time.

In the simulation, we have to improve the calculation process of collision. The improvement will enable the physics engine to re-create the actual motion of LSEAs and evaluate more quantitatively.

Appendix

I Pull-in Phenomenon

The phenomenon of contraction that exceeds the balance of an elastic force and coulomb force is called "pull-in". Let us consider a parallel plate electrode pair with the initial air gap d between the electrodes. In the situations where the electrodes are connected with each other by a linear spring k of the natural length d, the electrostatic force F_e after application of a voyage V and the elastic force F_s of the spring after the displacement of $d - x$ are given by

$$F_e(x) = \frac{1}{2}\frac{\varepsilon S V^2}{x^2}, F_s(x) = k(d - x). \tag{I.1}$$

where, ε is the dielectric constant, S is the area of the electrode. In this model, for gap x, a border point α in position control exists. Once x becomes lower than α, the electrodes will cling with each other due to the electrostatic force surpasses the elastic force overall (pull-in phenomenon). At $x = \alpha$, the electrostatic force and the derivation become to equal to those of the elastic force respectively, therefore,

$$F_e'(\alpha) = F_s'(\alpha) \quad \therefore -\frac{\varepsilon S V^2}{\alpha^3} = k, \tag{I.2}$$

$$F_e(\alpha) = F_s(\alpha) \quad \therefore \frac{1}{2}\frac{\varepsilon S V^2}{\alpha^2} = k(d - \alpha). \tag{I.3}$$

so,

$$\varepsilon S V^2 = 2d\frac{\varepsilon S V^2}{\alpha} - 2\varepsilon S V^2. \tag{I.4}$$

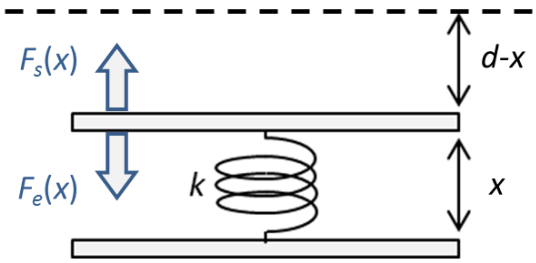

Figure I.1: Schematic of a parallel plate electrode connected with a linear spring.

then, α is given by following simple value:

$$\alpha = \frac{2}{3}d \tag{I.5}$$

It should be noted that this value is not dependent on the other parameters, that is, the range of the controllable position is always ranged from d to $2d/3$ regardless of the applied voltage.

II Electrostatic Force Generated in a Parallel Plate Electrode Laminated by a Solid Insulator

Let us consider a parallel plate electrode pair of the area S laminated by a solid insulator of the relative permittivity ε_1 as shown in Figure II.1. If the electrode pair is in an insulating fluid of the relative permittivity ε_2, the electrostatic capacitance is expressed as follows:

$$C = \frac{\varepsilon_0 S}{\dfrac{t}{\varepsilon_1} + \dfrac{d}{\varepsilon_2}}, \tag{II.1}$$

where t is the thickness of the solid insulator, d is the thickness of the insulating fluid, and ε_0 is the electric permittivity of vacuum. When a voltage V is applied, the charge stored in the electrode is

$$Q = \frac{\varepsilon_0 S V}{\dfrac{t}{\varepsilon_1} + \dfrac{d}{\varepsilon_2}}. \tag{II.2}$$

The electrostatic energy stored in the insulators is given by

$$U_e = \frac{1}{2} Q V. \tag{II.3}$$

If the electrostatic force generated between the electrodes narrows the thickness of the insulating fluid by Δd, the power source loses its energy $E = QV$ and the

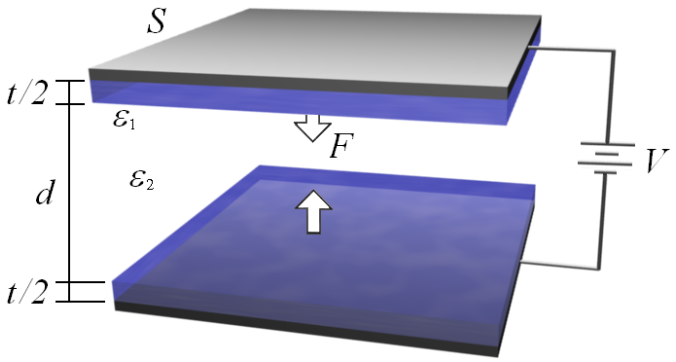

Figure II.1: Schematic of a parallel plate electrode with a solid insulator in an insulating fluid.

electrostatic energy U_e increases. The work-energy relation is expressed as follows:

$$F\Delta d = \Delta E - \Delta U_e = \Delta W. \tag{II.4}$$

Here, the work W done by the electrostatic force is equal to U_e. The electrostatic force is therefore given by

$$C = \frac{\partial W}{\partial d} = -\frac{1}{2}\frac{\varepsilon_0 S V^2}{\varepsilon_2 \left(\frac{t}{\varepsilon_1} + \frac{d}{\varepsilon_2}\right)^2}, \tag{II.5}$$

The minus sign shows that the electrostatic force is an attractive force.

III Large Deflection of a Cantilever Beam

The deflection of a cantilever beam under loading is known to be described by a relationship between the curvature at any point on the beam and the applied bending moment at that point under the assumption that the beam obeys Bernoulli-Euler theory. Let us consider a cantilever beam having length L and flexural rigidity $B = EI$ subjected to the concentrated vertical force P and horizontal force Q at the free end. Here, E and I represents the Young's modulus and the moment of inertia of area. The arc length measured from the fixed end and the slope angle of the centroidal axis of the beam are denoted by s and $\phi(s)$, respectively. If x is the horizontal coordinate and y is the vertical coordinate measured from the fixed end, the relationship between the curvature and the bending moment is

$$B\frac{d\phi}{ds} = -M = P(L - \delta_x - x) + Q(\delta_y - y), \tag{III.1}$$

where $\dfrac{d\phi}{ds}$ is the curvature of the beam, δ_x is the horizontal component of the displacement and δ_y is the vertical displacement. The differential of Equation (III.1) is

$$\frac{d^2\phi}{ds^2} = -\frac{P}{B}\frac{dx}{ds} - \frac{Q}{B}\frac{dy}{ds} = -\frac{P}{B}\cos\phi - \frac{Q}{B}\sin\phi. \tag{III.2}$$

The integral over ϕ gives

$$\frac{1}{2}\left(\frac{d\phi}{ds}\right)^2 = -\frac{P}{B}\sin\phi + \frac{Q}{B}\cos\phi + C = -\frac{A}{B}\sin(\phi - \varphi) + C, \tag{III.3}$$

where A denotes $\sqrt{P^2 - Q^2}$ and φ denotes $\cos^{-1}\dfrac{P}{A}$. The constant C can be evaluated by observing that the curvature at the free end ϕ_0:

$$\begin{aligned}\left(\frac{d\phi}{ds}\right)^2 &= -\frac{2A}{B}\left\{\sin(\phi - \varphi) - \sin(\phi_0 - \varphi)\right\} \\ \therefore \frac{d\phi}{ds} &= \sqrt{\frac{2A}{B}}\left\{\sin(\phi_0 - \varphi) - \sin(\phi - \varphi)\right\}^{\frac{1}{2}}.\end{aligned} \tag{III.4}$$

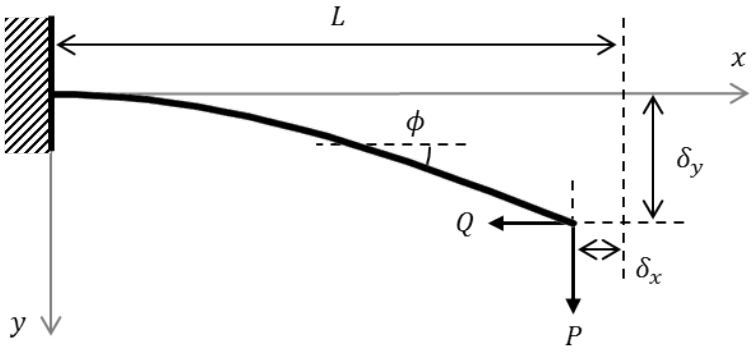

Figure III.1: A cantilever beam bended by the concentrated vertical force P and horizontal force Q at the free end.

The integral from the fixed end to the free end gives

$$\sqrt{\frac{2A}{B}}\int_0^L ds = \int_0^{\phi_0} \{\sin(\phi_0-\varphi)-\sin(\phi-\varphi)\}^{-\frac{1}{2}}\, d\phi = \left(\frac{2AL^2}{B}\right)^2. \qquad \text{(III.5)}$$

Denote $\dfrac{AL^2}{B}$, $\phi_0-\varphi$ and $\phi-\varphi$ by α^2, Φ_0 and Φ respectively:

$$\begin{aligned}\sqrt{2}\alpha &= \int_0^{\phi_0} \{\sin(\phi_0-\varphi)-\sin(\phi-\varphi)\}^{-\frac{1}{2}}\, d\phi \\ &= \int_{-\varphi}^{\Phi_0} (\sin\Phi_0-\sin\Phi)^{-\frac{1}{2}}\, d\Phi, \qquad \text{(III.6)}\end{aligned}$$

and let

$$\begin{cases} \sin\Phi = 2k^2\sin^2\theta - 1 \\ \sin\Phi_0 = 2k^2 - 1. \end{cases} \qquad \text{(III.7)}$$

Then

$$\alpha = \int_{\theta_1}^{\frac{\pi}{2}} \left(1-k^2\sin^2\theta\right)^{-\frac{1}{2}} d\theta \qquad \text{(III.8)}$$

$$\sin\theta_1 = \frac{1}{\sqrt{2}k}\left(1-\sin\varphi\right)^{\frac{1}{2}}. \qquad \text{(III.9)}$$

Equations (III.8) and (III.9) find the value of k and θ_1 simultaneously.

The vertical displacement δ_y is obtained from the equation described below,

$$\frac{dy}{d\phi}\frac{d\phi}{ds} = \frac{dy}{ds} = \sin\phi, \tag{III.10}$$

and since we have $\dfrac{d\phi}{ds}$ from Equation (III.4),

$$\frac{dy}{d\phi}\sqrt{\frac{2A}{B}}\left(\sin\Phi_0 - \sin\Phi\right)^{\frac{1}{2}} = \sin\Phi\cos\varphi + \cos\Phi\sin\varphi. \tag{III.11}$$

Thus

$$\begin{aligned}\delta_y = \int_0^{\delta_y} dy &= \sqrt{\frac{B}{2A}}\cos\varphi\int_{-\varphi}^{\Phi_0}\left(\sin\Phi_0 - \sin\Phi\right)^{-\frac{1}{2}}\sin\Phi d\Phi \\ &\quad + \sqrt{\frac{B}{2A}}\sin\varphi\int_{-\varphi}^{\Phi_0}\left(\sin\Phi_0 - \sin\Phi\right)^{-\frac{1}{2}}\cos\Phi d\Phi.\end{aligned} \tag{III.12}$$

With the aid of Equation (III.7) we obtain the equation containing complete and incomplete elliptic integrals of the first (F) and second (E) kinds

$$\frac{\delta_y}{L} = \left[1 - 2\frac{E(k) - E(k,\theta_1)}{F(k) - F(k,\theta_1)}\right]\cos\varphi + \frac{2|k|\sin\varphi\cos\theta_1}{F(k) - F(k,\theta_1)}. \tag{III.13}$$

The horizontal displacement δ_x is calculated from Equation (III.1) with $x = 0$ and $y = 0$ when $\phi = 0$. Thus,

$$\begin{aligned}P(L - \delta_x) + Q\delta_y &= B\left(\frac{d\phi}{ds}\right)_{\phi=0} \\ &= \sqrt{2AB}\left(\sin\Phi_0 + \sin\varphi\right)^{\frac{1}{2}},\end{aligned} \tag{III.14}$$

or

$$\frac{L - \delta_x}{L} = \frac{1}{\alpha}\sqrt{2 - 2\left(\frac{Q}{P}\right)^2}\left(\sin\Phi_0 + \sin\varphi\right)^{\frac{1}{2}} - \frac{Q}{PL}\delta_y. \tag{III.15}$$

IV Tensile Test of the PET Film and the Electrode Film

Figure IV.1a is a measurement result of tensile test of the PET film of 1.5 μm thick which was the same material used as a insulator of the LSEA prototypes. This shows the elasticity of the PET film and the slope around 0.01 of the strain denotes the Young's modulus of 4.15 GPa.

Figure IV.1b represents a result of tensile test of the electrode film. The slope shows that the Young's modulus was within 2.2-4.6 GPa.

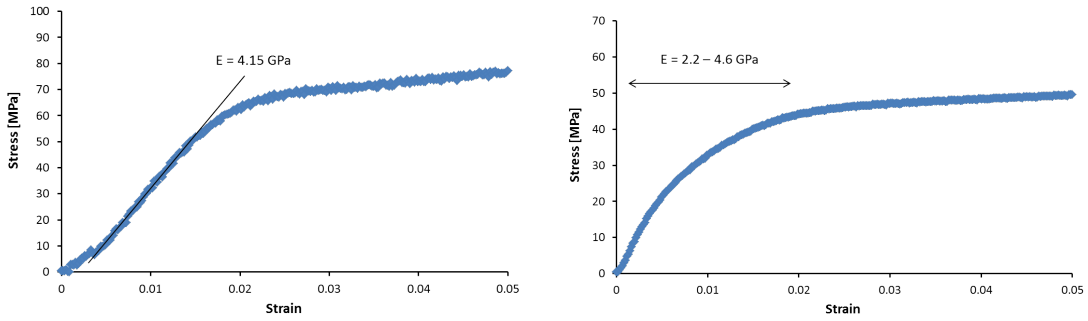

(a) PET Film **(b)** Electrode Film

Figure IV.1: Results of the tensile test of the PET film and the electrode film.

References

[1] M. De Volder, A.J.M. Moers, and D. Reynaerts. Fabrication and control of miniature McKibben actuators. *Sensors and Actuators A: Physical*, 166(1):111 – 116, 2011.

[2] D. Kamo, M. Maehara, D. Tanaka, and T. Nakamura. Development of a manipulator with straight-fiber-type artificial muscle and differential gear mechanism. In *Proceedings of the 37th Annual Conference on IEEE Industrial Electronics Society*, pages 98–103, 2011.

[3] K. Mitsui. A wonderful phenomenon of spontaneously flowing fluid without an external force. *Gijyutu-joho (in Japanese)*, pages 7 – 10.

[4] J. Zeng and T. Korsmeyer. Principles of droplet electrohydrodynamics for lab-on-a-chip. *Miniaturisation for chemistry, biology and bioengineering*, 4:265 – 277, 2004.

[5] T. C. Waram. Actuator design using shape memory alloys. *T. C. Waram, Hamilton, Ontario, 2nd edition*, 1993.

[6] Dynalloy Inc. Technical characteristics of FLEXINOL® actuator wire. December 2013.

[7] H. Meng and J. Hu. A brief review of stimulus-active polymers responsive to thermal, light, magnetic, electric, and water/solvent stimuli. *Journal of Intelligent Material Systems and Structures*, 21:859–885, 2010.

[8] P. Brochu and Q. Pei. Advances in Dielectric Elastomers for Actuators and Artificial Muscles. *Macromolecular Rapid Communication*, 31:10–36, 2010.

[9] Z. Cheng and Q. Zhang. Field-activated electroactive polymers. *MRS Bulletin*, 33:183–187, 2008.

[10] I. W. Hunter and S. Lafontaine. A comparison of muscle with artificial actuators. In *5th Technical Digest of IEEE Solid-State Sensor and Actuator Workshop*, pages 178–185, 1992.

[11] C. Huang, R. Klein, F. Xia, H. Li, Q. M. Zhang, F. Bauer, and Z.-Y. Cheng. Poly(vinylidene fluoride-trifluoroethylene) based high performance electroactive polymers. *IEEE Transactions on Dielectrics and Electrical Insulation*, 11(2):299–311, 2004.

[12] J. Su, J. S. Harrison, and T. St. Clair. Novel polymeric elastomers for actuation. In *Proceedings of the 12th IEEE International Symposium on Applications of Ferroelectrics*, volume 2, pages 811–814, 2000.

[13] R. E. Pelrine, R. D. Kornbluh, and J. P. Joseph. Electrostriction of polymer dielectrics with compliant electrodes as a means of actuation. *Sensors and Actuators A: Physical*, 64(1):77 – 85, 1998.

[14] J.-S. Plante and S. Dubowsky. On the properties of dielectric elastomer actuators and their design implications. *Smart Materials and Structures*, 16(2):S227–S236, 2007.

[15] W. Yuan, L. B. Hu, Z. B. Yu, T. Lam, J. Biggs, S. M. Ha, D. J. Xi, B. Chen, M. K. Senesky, G. Grüner, and Q. Pei. Fault-tolerant dielectric elastomer actuators using single-walled carbon nanotube electrodes. *Advanced Materials*, 20(3):621–625, 2008.

[16] F. Hu, J. Yao, C. Qiu, and H. Ren. A MEMS micromirror driven by electrostatic force. *Journal of Electrostatics*, 68(3):237–242, 2010.

[17] F. Hu, Z. Li, Y. Qian, J. Yao, X. Xiong, J. Niu, and Z. Peng. A multi-electrode and pre-deformed bilayer spring structure electrostatic attractive MEMS actuator with large stroke at low actuation voltage. *Journal of Micromechanics and Microengineering*, 22(9):095023, 2012.

[18] T. Chen, L. Sun, L. Chen, W. Rong, and X. Li. A hybrid-type electrostatically driven microgripper with an integrated vacuum tool. *Sensors and Actuators A: Physical*, 158(2):320–327, 2010.

[19] F. M. Ozkeskin, S. Choi, K. Sarabandi, and Y. B. Gianchandani. An all-metal micro-relay with bulk foil Pt-Rh contacts for high-power RF applications. *IEEE Transactions on Microwave Theory and Techniques*, 60(6):1595–1604, 2012.

[20] H.-C. Chang, J. M.-L. Tsai, H.-C. Tsai, and W. Fang. Design, fabrication, and testing of a 3-DOF HARM micromanipulator on (1 1 1) silicon substrate. *Sensors and Actuators A: Physical*, 125(2):438–445, 2006.

[21] H. Amakawa, K. Fukuzawa, M. Shikida, H. Tsuji, H. Zhang, and S. Itoh. An electrostatic actuator for dual-axis micro-mechanical probe on friction force microscope. *Sensors and Actuators A: Physical*, 175(0):94–100, 2012.

[22] S.-W. Chung and Y.-K. Kim. Design and fabrication of 10 × 10 micro-spatial light modulator array for phase and amplitude modulation. *Sensors and Actuators A: Physical*, 78(1):63–70, 1999.

[23] T. Ikeda, Y. Kanamori, and K. Hane. Si photonic nano-wire tunble micro-ring resonator composed of triply-liked variable couplers. In *Proceedings of the IEEE International Conference on Micro Electro Mechanical Systems; Paris, France*, pages 660–663, 2012.

[24] T. Niino, S. Egawa, H. Kimura, and T. Higuchi. Electrostatic artificial muscle: compact, high-power linear actuators with multiple-layer structures. In *Proceedings of the IEEE workshop on Micro Electro Mechanical Systems*, pages 130–135, 1994.

[25] T. Niino, S. Egawa, N. Nishiguchi, and T. Higuchi. Development of an electrostatic actuator exceeding 10 N propulsive force. In *Proceedings of Micro Electro Mechanical Systems; Travemünee, Germany*, pages 122–127, 1992.

[26] S. Egawa, M. Fujie, and T. Higuchi. A study on electrostatic actuator for physical aids. *Journal of Robotics Society of Japan*, 15:1147–1155, 1994.

[27] Z. G. Zhang, M. Gondo, N. Yamashita, A. Yamamoto, and T. Higuchi. Design and control of a fish-like robot using an electrostatic motor. In *Proceedings of the IEEE International Conference on Robotics and Automation*, pages 974–979, 2007.

[28] K. Minami, S. Kawamura, and M. Esashi. Fabrication of distributed electrostatic micro actuator (DEMA). *Journal of Microelectromechanical Systems*, 2(3):121–127, 1993.

[29] D. Halliday, R. Resnick, and K. S. Krane. Physics, volume 2. *John Wiley & Sons, New York, NY, fifth edition*, 2002.

[30] E. Husain and R. S. Nema. Analysis of paschen curves for air, N_2 and SF_6 using the townsend breakdown equation. *IEEE Transactions on Electrical Insulation*, EI-17(4):350–353, 1982.

[31] L. H. Germer. Physical processes in contact erosion. *Journal of Applied Physics*, 29(7):1067–1082, 1958.

[32] P. Kisliuk. Electron emission at high fields due to positive ions. *Journal of Applied Physics*, 30(1):51–55, 1959.

[33] M. Radmilović-Radjenović, J. K. Lee, F. Iza, and G. Y. Park. Particle-in-cell simulation of gas breakdown in microgaps. *Journal of Physics D: Applied Physics*, 38(6):950, 2005.

[34] P. G. Slade and E. D. Taylor. Electrical breakdown in atmospheric air between closely spaced (0.2 μm - 40 μm) electrical contacts. *IEEE Transactions on Components and Packaging Technologies*, 25(3):390–396, 2002.

[35] R. G. Horn and D. T. Smith. Contact electrification and adhesion between dissimilar materials. *Science*, 256(5055):362–364, 1992.

[36] K. Saneyoshi, K. Okuda, and Y. Hata. The characteristics of contraction of a layered type electrostatic actuator. In *Proceedings of the 22nd Annual Conference of the Robotics Society of Japan; Gifu, Japan*, page 2C11, 2004. Accompanied by: CD-ROM. Japanese.

[37] K. Okuda and K. Saneyoshi. Development of stacked-type electrostatic actuator using two ribbon films. *Journal of Robotics and Mechatronics*, 25(2):324–332, 2013.

[38] Q. Pei R. Pelrine, R. Kornbluh and J. Joseph. High-speed electrically actuated elastomers with strain greater than 100 %. *Science*, 287(5454):836–839, 2000.

[39] S. M. Bobbio, M. D. Kellam, B. W. Dudley, S. Goodwin-Johansson, S. K. Jones, J. D. Jacobson, F. M. Tranjan, and T. D. DuBois. Integrated force arrays. In *Proceedings of Micro Electro Mechanical Systems*, pages 149–154, 1993.

[40] J. D. Jacobson, S. H. Goodwin-Johansson, S. M. Bobbio, C. A. Bartlett, and L. N. Yadon. Integrated force arrays: theory and modeling of static operation. *Journal of Microelectromechanical Systems*, 4(3):139–150, 1995.

[41] Y. Yamano, Y. Miyauchi, and S. Kobayashi. Real time measurement of surface charge distractions under vacuum flashover events. *Saitama University Kiko*, 38, 2005. Japanese.

[42] Yamano Y., H. Yamazaki, S. Kobayashi, Y. Saito, and G. Zhang. Comparison of surface charge distributions under vacuum and atmospheric condition due to surface discharge events. In *Proceedings of the 24th International Symposium on Discharges and Electrical Insulation in Vacuum; Braunschweig, Germany*, 2010.